NANOPORES FOR DETECTING AND SENSING BIOLOGICAL MOLECULES

BY

AMIR BARATI FARIMANI

DISSERTATION

Submitted in partial fulfillment of the requirements
for the degree of Doctor of Philosophy in Mechanical Engineering
in the Graduate College of the
University of Illinois at Urbana-Champaign, 2015

Urbana, Illinois

Doctoral Committee:

Professor Narayana R. Aluru, Chair
Professor Emad Tajkhorshid
Professor Eric Jakobsson
Professor Joseph W. Lyding

Abstract

In spite of significant advances in the detection, separation and counting of single biological molecules (DNA, proteins, aminoacids, etc.) with solid-state nanopores, atomically-resolved scanning and detection of these molecules remains a significant challenge. In most nanopore-based DNA sequencing and single molecule detection techniques, ionic current blockade and blockade duration are the primary signatures associated with reading and scanning. Although these techniques are good enough for single molecule detection, they are not sophisticated enough to analyze and detect single DNA bases, fine structures, homologues and mutagenesis. Aside from the detection difficulties, low signal to noise ratio (SNR), fast speed of translocation, and lack of a cross-check signal are the biggest challenges of current nanopore technology. In this study, we explored different nanopore architectures and materials to find solutions to these current challenges. Using extensive atomistic simulations, we showed that a single layer molybdenum Disulfide (MoS_2) nanopore is attractive pore for single base DNA detection with high SNR and multi-level conductance. We introduced and simulated MscL (Mechano-Sensitive Channel of Large Conductance) as an alternative to traditional biological nanopores (Alpha-Hemolysin, MspA) since it provides a flexible nanopore with adaptability to DNA base types. Induced tension in MscL is shown to be different and distinguishable for each DNA base type. The speed of DNA translocation is also decreased by one order of magnitude in MscL, providing a better detection resolution compared to its counterpart, e.g. MspA. Next, we explored DNA

origami-graphene hybrid nanopore for DNA detection. We found that the dwell time of each base type in the hybrid pore is different and distinguishable compared to pristine graphene nanopore. The specific interaction (hydrogen bonds) between the complimentary bases at the edge of the pore and the translocating DNA bases give rise to distinguishable dwell time for each DNA.

In addition to DNA sequencing studies, we also investigated the recognition of natively folded proteins using graphene nanopore. We specifically focused on the detection of Immunoglobin G subclasses since the separation and the detection of different subclasses of IgG is the signature of many diseases. These four subclasses differ only in their hinge regions and are 95% homologues. We showed that the one atom thick graphene is highly capable of distinguishing between the subclasses by using ionic current and water flux signals.

To my family

Acknowledgements

I would like to thank my advisor, Professor Narayana R. Aluru, for his great guidance, patience and advice that helped me to reach my goals. I appreciate all his contributions of time, ideas, and funding to make my Ph.D. experience productive and stimulating. The great joy and enthusiasm he has for his research was contagious and motivational for me, even during tough times in the Ph.D. pursuit. He gave me the freedom to explore and collaborate on different projects during the course of my Ph.D. I would also like to deeply thank Professor Emad Tajkhorshid for his everlasting supports and inputs. He opened up new horizons in my view of biological systems at molecular level. My special thanks are extended to Professor Eric Jakobsson for his time and thoughtful comments. I also thank Professor Lyding, my Ph.D. committee member, whose feedbacks and helps are overwhelming.

I also need to thank Professor Amin Salehi Khojin, Professor John Rogers, Professor Eric Pop and Professor Sergei Sukharev for their wonderful guidance, support and collaborations. I also need to mention that through these collaborations with these fabulous experimentalists, I gained enough insights which lead me to better understanding of devices and nano-systems.

Finally, I am also very grateful for the constant support I received from the Computational Multiscale Nanosystems group throughout these years that I have pursued my Ph.D. studies.

TABLE OF CONTENTS

CHAPTER 1: Introduction

1.1 Significance of DNA Sequencing

Detailed human genome sequencing will help to enhance our current understanding of hereditary diseases, defective genome, identification, cloning and cancer. Sequencing also plays a critical role in the determination of the genetic defects associated with a variety of human diseases. In addition to diagnostics, sequencing has an emerging role in drug design. The tremendous growth in the processes requiring the fast and precise DNA sequencing, urges the developments of the technologies which can deliver cheaper and faster genome sequencing.[1, 2] To reach this goal, in 2004, National Institute of Health (NIH) proposed[1, 2] a challenge to the researchers to find a technology that can sequence the whole genome under $1000. This initiative and other health incentives inspired the second and the third generation sequencing methods to appear. Among these technologies, nanopore technology is an attractive method for DNA detection which is still under development.[1, 3]

1.2 Nanopore technology

Nanopores are thin insulating membranes (usually a few nanometers in thickness and diameter) that separate the two chambers containing conductive electrolytes. A charged molecule is driven through the nanopore by applying electric field (this process is called electrophoresis). As the molecules are translocating through the nanopore, certain number of ions are passing through the pore, modulating electrical current. The read out of this current may provide useful information

about the translocating molecules (Figure 1.1). Nanopores are attractive devices for DNA/protein detection because it is a single molecule approach which can potentially yield a high-throughput DNA analysis. Also, it benefits from relatively low cost and can be used to read very long threads of DNA. In nanopore DNA detection technology, the modulated current represents and defines the four different nucleotide types, i.e. adenine (A), guanine (G), cytosine (C), and thymine (T).[1]

The idea of DNA detection using nanopore was first proposed by Kasianowicz et al. in a patent application in 1998.[4] They used Alpha-Hemolysin, a naturally occurring biological nanopore, as a proof of concept experiment. Since then, numerous biological and synthetic nanopores were proposed for DNA sequencing. [4]

Biological nanopores offer several advantages for single-molecule DNA analysis over their synthetic counterparts. First, mutagenesis can be used to tailor the physical and chemical properties of biological nanopores; Second, biological nanopores are produced by cells with an atomic level precision that may not be reachable with solid-state fabrication approaches; Third, crystallography data of protein channels is available at sub nanometer length scales.[5]

α-Hemolysin is a protein that spontaneously inserts itself into a lipid bilayer membrane. This protein pore is formed by a 3.6 nm diameter vestibule connected to a β-barrel that is ~5 nm long and around 2.5 nm wide (Figure 1.2). It has a transmembrane channel with a width of 1.4 nm at its narrowest point. αHL shows the ionic conductance as high as one nS, when it is working with one molar salt concentration.[3] αHL cylindrical beta barrel is not tight enough to yield a distinguishable ionic current specific to individual nucleotides and therefore, exhibits small current differences between the nucleotides.[6] Another well-studied biological nanopore for DNA sequencing is Mycobacterium Smegmatis Porin A (MspA).[6, 7] MspA has been shown to provide

better ionic current signals for differentiating nucleotides as its pore structure includes a tighter 1.2 nm constriction region (Figure 1.2).[7]

In addition to biological nanopores, solid-state nanopores also were fabricated and used in DNA sequencing since 2001. Golovchenko and his colleagues[8] used the ion-beam sculpting system to create nanopores with merely precise sizes in thin SiN membranes. Solid-state nanopores are cheaper and more versatile compared to their biological nanopores. It is also possible to have large arrays of these pores for parallel sequencing. Its noteworthy that the solid state nanopores are stronger and more durable compared to biological protein-lipid systems. It is also possible to integrate the solid state nanopores to other electronics.[1, 3]

The disadvantages of classical solid state nanopores (SiN, SiO_2, HfO_2) are the large thickness of these membranes which prohibit the single base resolution recognition.[9] The thickness of these pores provides space for multiple bases to reside simultaneously inside the pore, leading to a signal which is the mixture of multiple bases.[1]

In 2010, graphene, a single sheet of carbon atom was introduced as a membrane for DNA detection, [10-12] with the hope that the atomic resolution diameter (0.34 nm thick) will resolve the single base detection of DNA bases.[10-12] Another advantage of graphene over high dielectric, thick solid state membranes is its capability for DNA recognition in transverse direction.[13-15] Additional yielded signal can be ancillary to ionic current and can potentially be used as a cross check signal.

The downside toward using graphene is its low signal to noise ratio (SNR) and the stickiness of its surface. [10, 11] DNA bases stick to the pore edges and surface, giving rise to more under defined interactions with graphene nanopore. To overcome this challenge, new two dimensional, single layer membranes were proposed. [16]

1.3 Structure of the Dissertation

The current thesis is comprised of four separate studies on nanopores for DNA and protein recognition. Each chapter includes an introduction, method and simulation set up, results and discussion and conclusion. Since the systems under study in this thesis differ in architecture and the pore type, the molecular dynamic (MD) simulation method section is written specifically for each chapter. The very detailed simulation information and the supporting results of each chapter are reported and classified in Appendices (A, B, C and D).

In the second chapter, we introduced Molybdenum Disulphide (MoS_2) single layer membrane as an attractive candidate for DNA detection with high sensitivity. In the third chapter, we introduced and studied a new class of biological nanopore called Mechano-Sensitive Channel of Large Conductance (MscL) with flexible pore for DNA detection.

In the fourth chapter, we focused on hybrid nanopore comprised of DNA origami nanopore and a thin membrane of graphene. The pore is anchored with specific DNA origami bases which give rise to distinguishable dwell time and ionic current for translocating DNA.

In the fifth and final chapter, we looked at the detection and recognition of natively folded antibodies using graphene nanopore. By taking advantage of thin graphene membrane, we were able to distinguish between two homologues subclasses of Immunoglobin G (IgG).

1.4 Figures

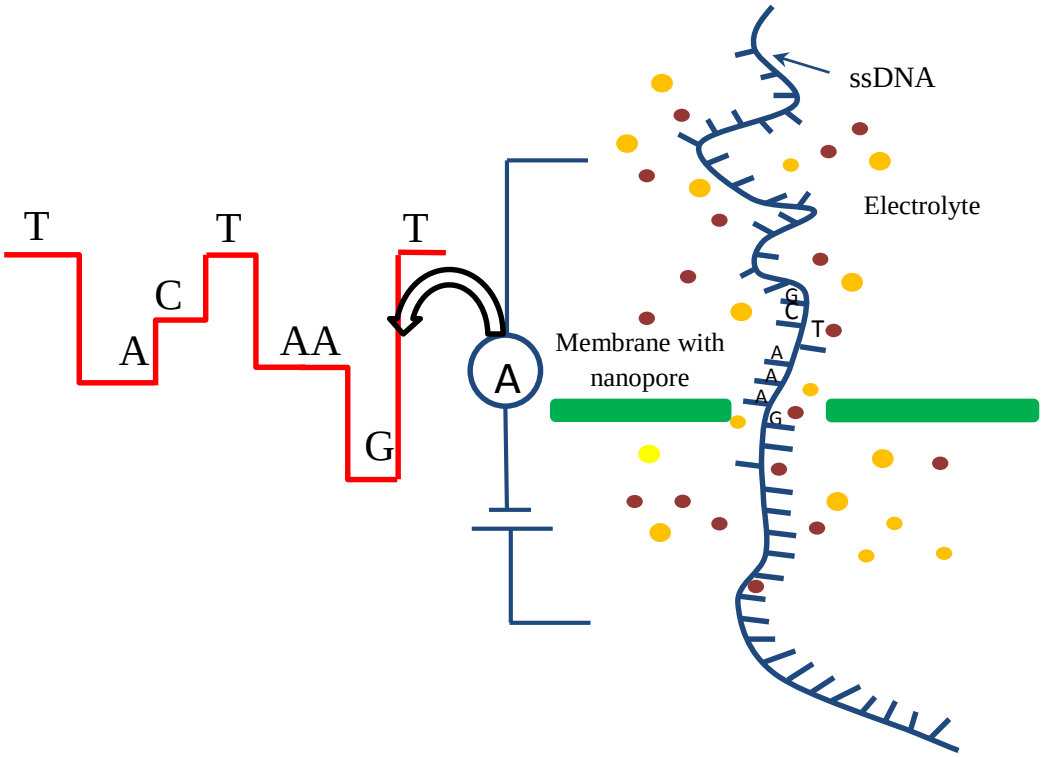

Figure 1.1 |The general concept of DNA detection with nanopore: the modulated current represents different base type in the nanopore.

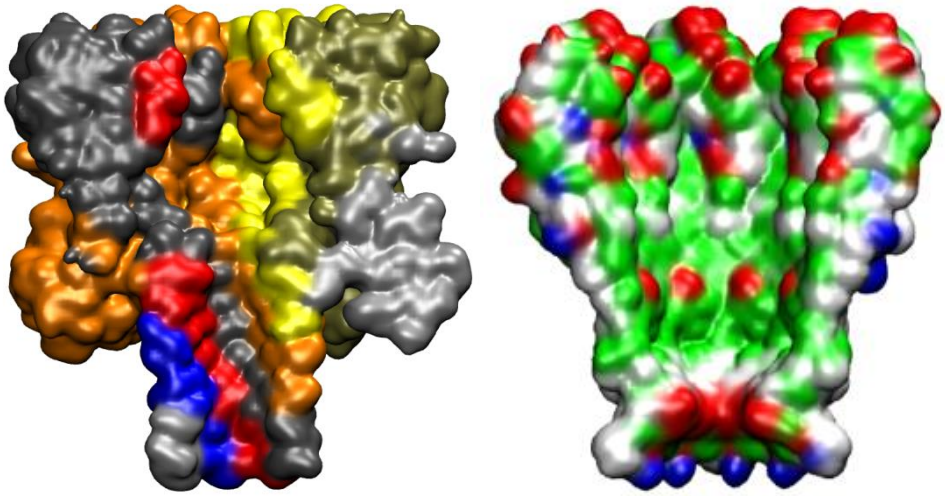

Figure 1.2 | The cross section of biological nanopores used in DNA sequencing experiments and simulations. **Left**: Alpha-Hemolysin, **Right**: MspA

1.5 References

1. Venkatesan, B. M.; Bashir, R. Nanopore Sensors for Nucleic Acid Analysis. *Nat. Nanotechnol.* 2011, 6, 615-624.
2. Branton, D.; Deamer, D. W.; Marziali, A.; Bayley, H.; Benner, S. A.; Butler, T.; Di Ventra, M.; Garaj, S.; Hibbs, A.; Huang, X. H.; Jovanovich, S. B.; Krstic, P. S.; Lindsay, S.; Ling, X. S. S.; Mastrangelo, C. H.; Meller, A.; Oliver, J. S.; Pershin, Y. V.; Ramsey, J. M.; Riehn, R.; Soni, G. V.; Tabard-Cossa, V.; Wanunu, M.; Wiggin, M.; Schloss, J. A. The Potential and Challenges of Nanopore Sequencing. *Nat. Biotechnol.* 2008, 26, 1146-1153.
3. Dekker, C. Solid-State Nanopores. *Nat. Nanotechnol.* 2007, 2, 209-215.
4. Kasianowicz, J. J.; Brandin, E.; Branton, D.; Deamer, D. W. Characterization of Individual Polynucleotide Molecules Using a Membrane Channel. *Proc. Natl. Acad. Sci. U. S. A.* 1996, 93, 13770-13773.
5. Farimani, A. B.; Heiranian, M.; Aluru, N. R. Electromechanical Signatures for DNA Sequencing through a Mechanosensitive Nanopore. *J. Phys. Chem. Lett.* 2015, 6, 650-657.
6. Butler, T. Z.; Pavlenok, M.; Derrington, I. M.; Niederweis, M.; Gundlach, J. H. Single-Molecule DNA Detection with an Engineered Mspa Protein Nanopore. *Proc. Natl. Acad. Sci. U. S. A.* 2008, 105, 20647-20652.
7. Chang, G.; Spencer, R. H.; Lee, A. T.; Barclay, M. T.; Rees, D. C. Structure of the Mscl Homolog from Mycobacterium Tuberculosis: A Gated Mechanosensitive Ion Channel. *Science* 1998, 282, 2220-2226.
8. Li, J.; Stein, D.; McMullan, C.; Branton, D.; Aziz, M. J.; Golovchenko, J. A. Ion-Beam Sculpting at Nanometre Length Scales. *Nature* 2001, 412, 166-169.
9. Ahmed, T.; Kilina, S.; Das, T.; Haraldsen, J. T.; Rehr, J. J.; Balatsky, A. V. Electronic Fingerprints of DNA Bases on Graphene. *Nano Lett.* 2012, 12, 927-931.
10. Wells, D. B.; Belkin, M.; Comer, J.; Aksimentiev, A. Assessing Graphene Nanopores for Sequencing DNA. *Nano Lett.* 2012, 12, 4117-4123.
11. Sathe, C.; Zou, X. Q.; Leburton, J. P.; Schulten, K. Computational Investigation of DNA Detection Using Graphene Nanopores. *ACS Nano* 2011, 5, 8842-8851.
12. Schneider, G. F.; Kowalczyk, S. W.; Calado, V. E.; Pandraud, G.; Zandbergen, H. W.; Vandersypen, L. M. K.; Dekker, C. DNA Translocation through Graphene Nanopores. *Nano Lett.* 2010, 10, 3163-3167.
13. Traversi, F.; Raillon, C.; Benameur, S. M.; Liu, K.; Khlybov, S.; Tosun, M.; Krasnozhon, D.; Kis, A.; Radenovic, A. Detecting the Translocation of DNA through a Nanopore Using Graphene Nanoribbons. *Nat. Nanotechnol.* 2013, 8, 939-945.
14. Saha, K. K.; Drndic, M.; Nikolic, B. K. DNA Base-Specific Modulation of Microampere Transverse Edge Currents through a Metallic Graphene Nanoribbon with a Nanopore. *Nano Lett.* 2012, 12, 50-55.
15. Garaj, S.; Liu, S.; Golovchenko, J. A.; Branton, D. Molecule-Hugging Graphene Nanopores. *Proc. Natl. Acad. Sci. U. S. A.* 2013, 110, 12192-12196.
16. Farimani, A. B.; Min, K.; Aluru, N. R. DNA Base Detection Using a Single-Layer MoS_2. *ACS Nano* 2014, 8, 7914-7922.

CHAPTER 2: DNA Base Detection Using a Single-Layer MoS_2 [*]

2.1 Introduction

Nanopore-based DNA sequencing has opened up opportunities for fast and high resolution recognition and detection of DNA bases (Guanine (G), Adenine (A), Thymine (T), and Cytosine (C)).[1-6] In these devices, a negatively charged DNA is driven through the nanopore along with other molecules such as water and ions.[2, 5, 7] DNA is electrophoretically[4] driven through a nanopore by an applied external electric field, and the ionic current through the nanopore is modulated during the DNA "translocation processes".[3, 8] The change in the ionic current as the DNA molecule passes through the nanopore represents a direct reading of the DNA sequence. [3, 5] The translocation occurs at speeds of about 10^7 bases per second, which is the sub-millisecond laboratory timescale.[9, 10] Solid-state nanopores[11, 12] and biological nanopores (e.g. α-hemolysin)[13] have been extensively used for DNA sequencing.[1, 2] In general, these membranes and pores are too thick (> 5 nm) to be able to perform sequencing at single base resolution.[11] Biological nanopores can be unstable, prone to be disassembled when biases higher than 1.0 V are applied, and can be quite sensitive to mechanical/thermal fluctuations.[2, 14, 15] To read the sequence of nucleotides in a DNA molecule,

[*] A. Barati Farimani, K. Min and N. R. Aluru, ``DNA base detection using a single-layer MoS2'', ACS Nano, Vol. 8, No. 8, pp. 7914-7922, 2014.

for example, a pore of nanometer thickness is required. [16] Graphene[17], a 2-D material with a thickness of 0.34 nm, has conceptually been demonstrated for DNA translocation and sequencing.[9, 14, 16, 18-20] The atomic-scale pore thickness can be used for DNA single base detection[18]. In addition to ionic current blockade, transverse tunneling current can also be used for electronic base detection.[21-23] Sequencing by tunneling has already been accomplished using standard solid-state pores and break junctions.[24, 25] It's notable that pristine graphene does not have a band gap[17], which is not desirable for electronic base detection and field effect transistors (FETs).[26] Engineering the band gap of graphene increases fabrication complexity[20, 27] and either reduces the electronic mobility or requires high voltages which are beyond threshold voltages for DNA.[16] A single layer of MoS_2 has a direct band gap of 1.8 eV,[28] which can be used to construct inter-band tunnel FETs for sensing applications.[28] Recently, it has been shown that using hafnium oxide (HfO_2) as gate dielectric can enhance the single-layer MoS_2 mobility by about 200 times at room temperature, which makes it comparable to graphene nanoribbon mobility.[28] This finding makes MoS_2 highly preferable to graphene in terms of DNA electronic base sensing.

It has been shown that ionic current blockade signal shows noise for DNA translocation through a single-layer graphene nanopore.[16, 29] The origin of this noise has been attributed to the atomic thickness of the pore. It is notable that a nanopore in a three-layer graphite structure, which has ~1 nm thickness, shows a better signal to noise ratio.[16, 29, 30] MoS_2 has a thickness of 1 nm which makes it a superior material compared to graphene in terms of signal/noise intensity while maintaining its monolayer property.

Another issue with graphene nanopore is that DNA sticks to the pore sides and surface during translocation process.[14, 16] Coexistence of bases on the surface and the pore sides will complicate the transverse tunneling current making the nucleobase identification difficult. In addition, the

stochastic motion of DNA through a nanopore generated due to the base adherence has under-defined interactions between the nanopore and the nucleobases.[9, 16, 31] Finding a substitute or a way to modify graphene for good sensing ability and non-sticky pore surface will be the challenge for the next generation DNA sequencing devices. Orientational fluctuations of nucleobases can give rise to overlapping current contributions from different bases, so it is advantageous to develop a device that can hold each base firmly while the base was being read.[15, 31] The thickness of a single-layer MoS_2 nanopore combined with the ability to engineer atoms (Molybdenum (Mo), Sulfur (S) or both) exposed to DNA bases opens up opportunities for DNA sequencing. In a recent work, DNA is translocated through a single layer MoS_2 and a SNR of higher than 10 has been demonstrated.[32] In this chapter, using Molecular Dynamics (MD) simulations, we demonstrate the translocation and sequencing of double stranded DNA (dsDNA) through MoS_2 nanopore with distinct ionic current blockade and low noise to signal ratio for each nucleobase. Furthermore, using Density Functional Theory (DFT) simulation, we show that both MoS_2 nanopore and MoS_2 surface can be used for single DNA base detection. A comparison between graphene and MoS_2 nanopore in terms of DNA adherence and pore architecture is also discussed.

2.2 Methods

2.2.1 MD simulation

We performed MD simulations with LAMMPS[33] to investigate DNA translocation in a MoS_2 nanopore (Figure 2.1.a). We used the structural features of the hairpin DNA (5'-D (ATCCTA-GTTA-TAGGAT)-3'). The specific feature of this DNA is the formation of a G-A base pair in the loop (Figure 2.1.b). A pore with a diameter of 2.3 nm is drilled in the center of an 8nm×8nm single layer MoS_2. Initially, DNA was placed at the mouth of the MoS_2 nanopore where the DNA axis (z direction) is along the nanopore axis (Figure 2.1.b). DNA and MoS_2 are submersed in water and

salt ionic solution. The ionic concentration of NaCl is 1M. We used the CHARMM27 force field[34] parameters for DNA, TIP3P water molecules, and ions. SHAKE algorithm was used to maintain the rigidity of the water molecules. The parameters for MoS_2 were taken from Reference[35]. For the interaction between MoS_2 and DNA, water and ions, we used mixing rules. MoS_2 atoms were frozen to their initial lattice position. In the case of graphene nanopore, C-C interaction is modeled with the AIREBO[36] potential. The Periodic boundary condition is applied in all the three directions. The cutoff distance for the LJ interactions is 15 Å. The long-range electrostatic interactions were computed by using the particle-particle-particle-mesh (PPPM) method. The time step is selected to be 1 fs. For each simulation, energy minimization was performed for 100,000 steps. Systems were then equilibrated for 1 ns with NPT ensemble at 1 atm pressure and 300 K temperature. NPT simulation ensures that the water concentration is equal to the bulk value of 1 g/cm^3. The simulation is then performed in NVT ensemble. Temperature was maintained at 300 K by applying the Nosè-Hoover thermostat with a time constant of 0.1 ps. Before applying the electric field, equilibration for 2ns is performed in NVT. Production simulations were performed by applying an external electric field in the z-direction. The external electric fields are reported in terms of a transmembrane voltage difference $V = EL_z$, where E is the electric field strength and L_z is the length of the simulation system in the z direction[16]. We monitored the time-dependent ionic current, $I(t)$, in the pore. We computed the ionic current through the nanopore by using the definition of current, $I=dq/dt$, as $I(t) = \frac{1}{L_z}\sum_{i=1}^{n} q_i \left[\frac{z_i(t+\delta t) - z_i(t)}{\delta t} \right]$, where the sum is for all the ions, δt is chosen to be 5 ps, and z_i and q_i are the z-coordinate, charge of ion i, and n is the total number of ions, respectively.

2.2.2 DFT simulation

We performed DFT with SIESTA to understand the physical nature of interaction between MoS_2 and nucleobases.[37] DFT has been widely used to investigate the physical/chemical adsorption mechanism, and it has also been shown that it can accurately capture the electronic properties of nano-materials, such as MoS_2, water filled buckyball, and graphene.[26, 38-40] For parameterization of the exchange-correlation functional, generalized gradient approximation (GGA) with Perdew-Burke-Ernzerhof (PBE) is used.[41] The core electrons are replaced by the norm-conserving pseudo-potentials.[42] For the basis set, double zeta basis plus polarization (DZP) numerical atomic orbital is used. For the k-point mesh generation, the 5x5x1 Monkhorst-Pack for structural relaxation for both MoS_2 and DNA, and 12x12x1 (bulk structure) and 1x1x40 (finite structure) Monkhorst-Pack for calculation of electronic properties are used.[43] A vacuum region of around 20 Å is used to remove any artificial effect from the non-periodic directions in the simulation box. Structural relaxation is achieved until the maximum residual force of the system is reached, which is less than 0.05 eV/Å. For MoS_2 structure construction, the unit cell of MoS_2 is first relaxed and using it a larger system is generated for interaction with DNA bases. (APPENDIX A) After energy minimization, the total Density of States (DOS) of the system (MoS_2 + DNA bases), which represents the number of states for each energy level, is obtained. The binding energy between MoS_2 substrate and DNA bases is calculated as $E_{Binding} = (E_{MoS2} + E_{Base}) - E_{Total}$, where E_{Total} is the total energy of the system (MoS_2 and Base), and E_{MoS2} and E_{Base} is the energy of each system, MoS_2 and single base, respectively. For the interaction of pristine MoS_2 with DNA base, the band gap change is studied. To understand the electron clouds overlap due to the interaction between MoS_2 and DNA bases, the charge density difference ($\Delta\rho$) is obtained, which is defined as $\Delta\rho = \rho_{MoS_2+Base} - (\rho_{MoS_2} + \rho_{Base})$, where ρ_{MoS_2} and ρ_{Base} represents the charge density distribution

of each structure (MoS_2 and DNA base), and ρ_{MoS_2+Base} is the charge density distribution of the total system.

2.3 MD Results and Discussion

We performed MD simulations on translocation of dsDNA through a 2.3 nm diameter pore in a single layer MoS_2 structure (Figure 2.1a and 2.1b). We used 2.3 nm pore size as prior studies for graphene nanopore have shown that a pore diameter of 2.3 nm is the smallest and most efficient pore size for the translocation of dsDNA[14] – specifically, this pore diameter shows better signatures of ionic current blockade for each DNA base and nucleotides[19]. Studies for graphene nanopore also reveal that the pore size of ~2.3 nm would help augmenting the transverse tunneling current due to the better mixing of the electronic cloud of carbon atoms and DNA bases. After equilibration (as described in the methods section), electric field is applied in the *z*-direction. The translocation history of DNA center of mass (COM) is registered for 3 biases of 2.1 V, 2.8 V and 3.57 V. Complete electrophoresis of DNA for 2.1 V, 2.8 V and 3.57 V takes 3.2 ns, 0.3 ns and 0.18 ns, respectively. Generally, a bias of 100 mV – 600 mV is applied in experiments for DNA translocation through nanopores. Here, for tractable computational studies, we applied a higher bias. According to our simulation data (APPENDIX A), for biases lower than 2.0 V, translocation is significantly hindered. Our estimates show that for biases of around 100 mV, the translocation time increases to microseconds. In all nanopore technologies, the high speed at which DNA is translocated through nanopores is very promising in ultra-fast sequencing (1 base/μs); however, the measurement of small currents requires the bandwidth to be of MHz[2], which limits the optimum sequencing speed. The red dashed line in Figure 2.1.c represents the pore mid-line which is aligned along the *x*-axis. For a low bias of 2.1 V, DNA (COM) oscillates around the mid-line. Initially,

when the dsDNA is located a few Angstroms away from the pore mouth, we observed the transient flux of ions and water (APPENDIX A) as the dsDNA approaches the pore entrance. Due to the confinement in the pore, dsDNA acts like a pump and pushes ions and water molecules inside the pore. To calculate the residence time, and translocation history of each base inside the pore, we tagged the atoms of each base when they are inside the pore. We counted the number of atoms of each base which occupy the pore at different time instances. Figure 2.2.a shows the density of each base inside the pore (for a bias of 2.8 V). It is observed that A-T and C-G bases occupy the pore most of the time. At t=250 ps, interestingly, only base A dominates the whole pore. Base T occupies the pore for t=100-250 ps. We computed the ionic current blockade, *I(t)*, when the DNA passes through the pore. The ionic current through the nanopore is shown in Figure 2.2.b. The computed ionic current in Figure 2.2.b is in nA, which is in agreement with experiments[32]. We associate the bases, A, T, C and G with the corresponding ionic current. At some time instances, two bases coexist in the pore and the associated ionic current is for both the bases combined. As shown in Figure 2.2.b, the ionic current associated with the bases decreases as AT > G > T > CG > C. This result also accounts for orientation of bases in the pore and we note that the effective blockade is higher for C and G bases compared to A and T (APPENDIX A). We compared the noise in ionic current in graphene and MoS_2 nanopores by considering the same pore size and applied bias (APPENDIX A). We found 4 distinct conductance states for MoS_2 nanopore compared to graphene which has only 2 conductance states. Graphene thickness is too small to capture the ionic current appropriately and 2 conductance states are not enough to distinguish all the bases in the pore. For example, the chloride ion size (σ) is larger than the pore thickness (t), (σ=0.41 nm compared to pore thickness of graphene, t=0.34 nm) and the effective pore occupation length of each base is larger than the graphene pore thickness. The origin of more conduction states

in MoS_2 nanopore can be attributed to the architecture of the pore that contains both hydrophobic (S atoms) and hydrophilic (Mo atoms) sites. We computed the signal to noise ratio (SNR)[44] of MoS_2 and graphene nanopores (APPENDIX A). SNR for MoS_2 and graphene nanopore is 15.02 and 3.32, respectively. The SNR results are in agreement with the experiments suggesting that the SNR of DNA ionic current in a MoS_2 nanopore is higher than ten.[32] The noise generated in graphene is 4-5 times larger compared to MoS_2. The best SNR taken for any nanopore (biological and solid state) to our current knowledge[45] is around 10 which is lower than MoS_2 SNR. In addition, the noise is significantly higher in the case of graphene. In the case of MoS_2 nanopore, the thickness of 1 nm combined with alternative arrangement of pore atoms (Mo/S) with hydrophobic-hydrophilic-hydrophobic architecture makes MoS_2 amenable for ionic current measurements with lower noise. Our findings can pave way towards efficient DNA sequencing by ionic current measurements.

2.3.1 Thermal Fluctuations and DNA modalities

To understand the effect of thermal fluctuations on the quality of the signal computed, we analyzed the effect of temperature on the noise generated in the pore. In all the pores, the translocation forces, which are electrostatic, compete with the drag forces in the nanopore[46]. The drag forces arise from the van der Waals (VdW) interactions with the pore atoms. We changed the strength of the applied bias and temperature to examine its effect on the SNR (see APPENDIX A for the calculation of SNR). Figure 2.2.c shows that as we increase the applied bias, SNR increases. Also, as we increase the temperature from T=300 K to 325 K, SNR decreases for all the applied biases. The decrease in SNR with increase in temperature is due to the increase in thermal vibration which gives rise to a larger stochastic motion of the bases in the pore. The root mean-squared displacement (RMSD) calculation of dsDNA in the MoS_2 nanopore (in the absence of applied bias)

reveals a higher DNA fluctuation (RMSD=3.65 Å) for T=325 K compared to T=300 K (RMSD=2.93 Å). The higher RMSD indicates a higher frequency of bases entering and exiting the pore. This can be further confirmed by the comparison with $I_{noise,RMS}$ (APPENDIX A). $I_{noise,RMS}$ is higher for T=325 K compared to T=300 K. From Figure 2.2.c, it can be inferred that higher biases can enhance the SNR which can be attributed to stretching of the dsDNA.

We measured the time-averaged maximum length of dsDNA in the presence of an applied bias and we observed that the stretching of the dsDNA increases with the bias (Figure 2.2.d). The snapshots of dsDNA modalities for V=0.1 volts and V=3.0 volts reveal that dsDNA knotting occurs frequently in lower biases in the nanopore, giving rise to a higher noise due to presence of multi-base in the nanopore (Figure 2.2.d)

2.3.2 Stickiness of the pores

One of the other challenges posed by DNA translocation through a graphene nanopore is the sticking behavior of DNA to the pore internal carbons and the surface of graphene.[14, 16] We performed MD simulations for both graphene and MoS_2 nanopore in order to compare their stickiness (to DNA) behavior (APPENDIX A). Surprisingly, DNA didn't adhere to MoS_2 in contrast to graphene where significant stickiness is observed. Liu *et al*. also found, by experiments, that DNA does not stick to the surface of MoS_2.[32] The architecture of the MoS_2 pore has Mo atoms which are strong hydrophilic sites. DNA is a hydrophobic structure, so it does not like to adhere to Mo sites. We performed MD simulations on two types of pore structures (Mo exposed only and S exposed only). Our observations suggest that having more Mo exposed in the pore would decrease the sticking of atoms to the pore sides and surface. These results open up opportunities for engineering the pore architecture for optimized DNA translocation through MoS_2.

2.4 DFT Results and Discussion

2.4.1 Bases in MoS_2 nanopore

To demonstrate the significance of using MoS_2 as a DNA-FET[47, 48] for nucleobase detection (see Figure 2.3.a for proposed architecture), we computed the electronic structure changes induced due to presence of DNA bases inside the nanopore using DFT.

In MoS_2 nanopores, the atoms exposed to DNA bases can be engineered with three possible configurations: Mo-terminated, S-terminated, and both Mo- and S-terminated edge. We first constructed a MoS_2 nanopore with Mo termination. The charge density rearrangement ($\Delta\rho$) in the nanopore (Mo-terminated) due to the interaction between MoS_2 and DNA bases is shown in Figure 2.3.b. It indicates that there are more overlapped electron clouds when G is inside the nanopore compared to T. This result suggests that base G will give rise to a higher conductance if bias is applied to the device.

To further investigate the effect of DNA bases (inside the pore) on MoS_2, the total Density of States (DOS) is obtained in Figure 2.3.c and it shows that Mo-terminated pore induces finite states around the Fermi level.[49] Each base is placed in a planar configuration (θ=0 and α=0, APPENDIX A) in the nanopore. The shape of the total DOS is significantly changed around the Fermi level as shown in Figure 2.3.c which indicates a strong interaction of the bases with MoS_2. Each base shows a different response, and G and A bases interact stronger than the other two bases (G>A>C>T) supported by the binding energy calculation as shown in Table 2.1. This can be further confirmed when the DNA bases are placed at an orientation, which is the most probable orientation (θ=40 to 52 degrees) obtained from MD simulations). (APPENDIX A) Similar to the case when the bases are placed horizontally, each DOS curve shows a distinct response for DNA

base interaction with MoS_2 nanopore and binding energy calculations also confirm this result as shown in Figure 2.3.d and Table 2.1.

Next, we also constructed two other configurations: S- terminated nanopore and both Mo- and S-terminated nanopore. As shown in the APPENDIX A, it should be noted that there is no distinct change in the total DOS when each base is placed horizontally, and the overall response is the same for all the bases. These results suggest that Mo atoms interact strongly with DNA bases compared to the S atoms, and Mo-terminated nanopores can potentially differentiate each base. This finding can be potentially used for the construction of a DNA-FET sensor for electronic detection of each base.

2.4.2 Interaction of Armchair MoS_2 Nanoribbon (AMNR) with DNA bases

To further investigate the potential application of a single-layer MoS_2 as a DNA sensing device in a nanochannel configuration, we studied the interaction of DNA bases with pristine armchair MoS_2 nanoribbon (AMNR) without any pore or defects (Device architecture and AMNR setup are shown in APPENDIX A). A similar concept has been proposed by Min *et al.* using a graphene nanoribbon (GNR), where a unique response of GNR to DNA bases has been demonstrated. [9] Unlike zigzag MoS_2 nanoribbon, which is a metal, AMNR exhibits a finite energy gap of 0.5349 eV that makes it amenable as a sensor. [50, 51] We performed DFT simulations by placing each nucleobase on top of AMNR in a planar configuration (APPENDIX A). A total of ten different configurations for each structure are considered and the average band gap is obtained. As shown in Figure 2.3.e, the total DOS of AMNR shows a characteristic response in the presence of each base. The band gap of each system is highly affected due to the presence of bases. Base G most significantly affects AMNR and gives rise to a reduction in band gap of 0.2 eV compared to pristine AMNR. Unlike

other bases, base T slightly opens the band gap of AMNR by 0.02 eV. The change in band gap is highest with base G and lowest with T and follows the order, G>A>C>T (Figure 2.3.f), which is the same order obtained for the MoS_2 nanopore (Mo-terminated) case. Interestingly, this order is also observed for the interaction of pristine graphene with DNA bases. [38, 39] The binding energy calculation further confirms this result, which shows a larger value for the case with higher change in band gap (see Figure 2.3.f). It's noteworthy that bases G and A inherit an additional five-membered ring attached to the six-membered ring compared to bases C and T with only one six membered ring. The additional ring in bases A and G provides the possibility of sharing higher level of electronic interactions with MoS_2. To investigate further on the origin of the band gap change, the local DOS for pristine AMNR, DNA base and the total system (base + AMNR) is computed (see Figure 2.4). The local DOS of AMNR is almost the same for all structures. It should be noted that the band gap change in MoS_2 interacting with base G is mainly due to the overlap of the energy states around the Fermi level induced from base G (Figure 2.4.a). For bases A and C, the finite energy states of each base are located around the Fermi level (Figure 2.4.c and 2.4.d) unlike the case of base T (Figure 4.b), which reduces the band gap.

2.5 Conclusion

In summary, we found that a single-layer MoS_2 is a promising material for DNA sequencing technology through the nanopore or the surface using MD and DFT simulations. MoS_2 nanopore shows a distinct ionic current signal for single nucleobase detection with a SNR of 15 which is consistent with the experimental results[32]. MoS_2 also shows a characteristic response in total DOS change for each base. The band gap of MoS_2 is significantly changed when bases are placed on the top of pristine MoS_2, which makes it a good material for base detection. In contrast to graphene,

for MoS_2 nanopore, DNA shows a more distinguishable signature per base. During translocation of DNA, bases stick to the graphene surface while MoS_2 nanopore shows a non-sticky behavior.

2.6 Figures

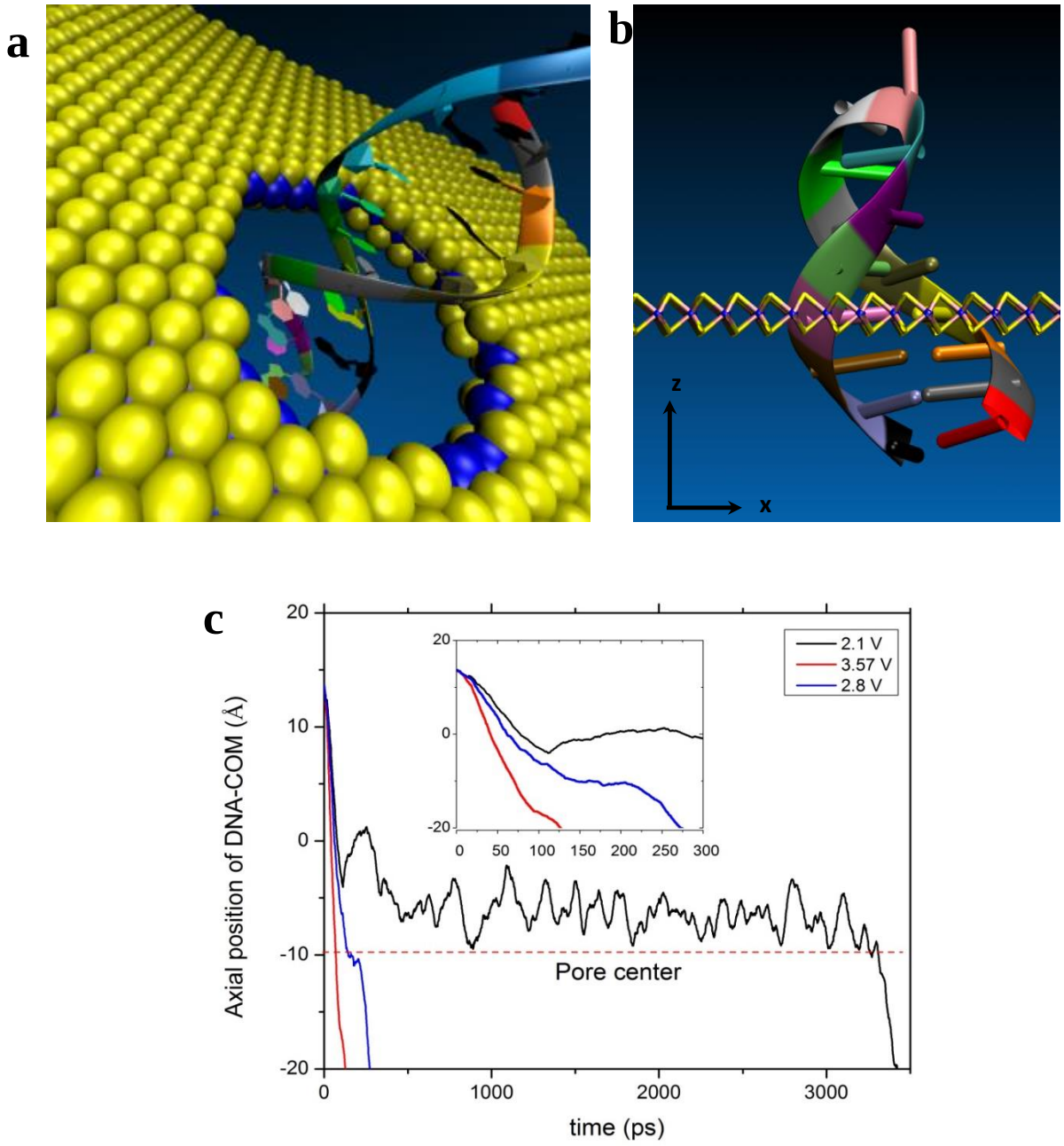

Figure 2.1.a| DNA translocation through a MoS_2 nanopore. **b|** DNA hairpin structure with the loop at the top (PDB code:1ac7 taken from PDB.org) and the side view of MoS_2 fish-bone structure. **c|** DNA translocation history for different biases; the red dashed line represents the center of the pore.

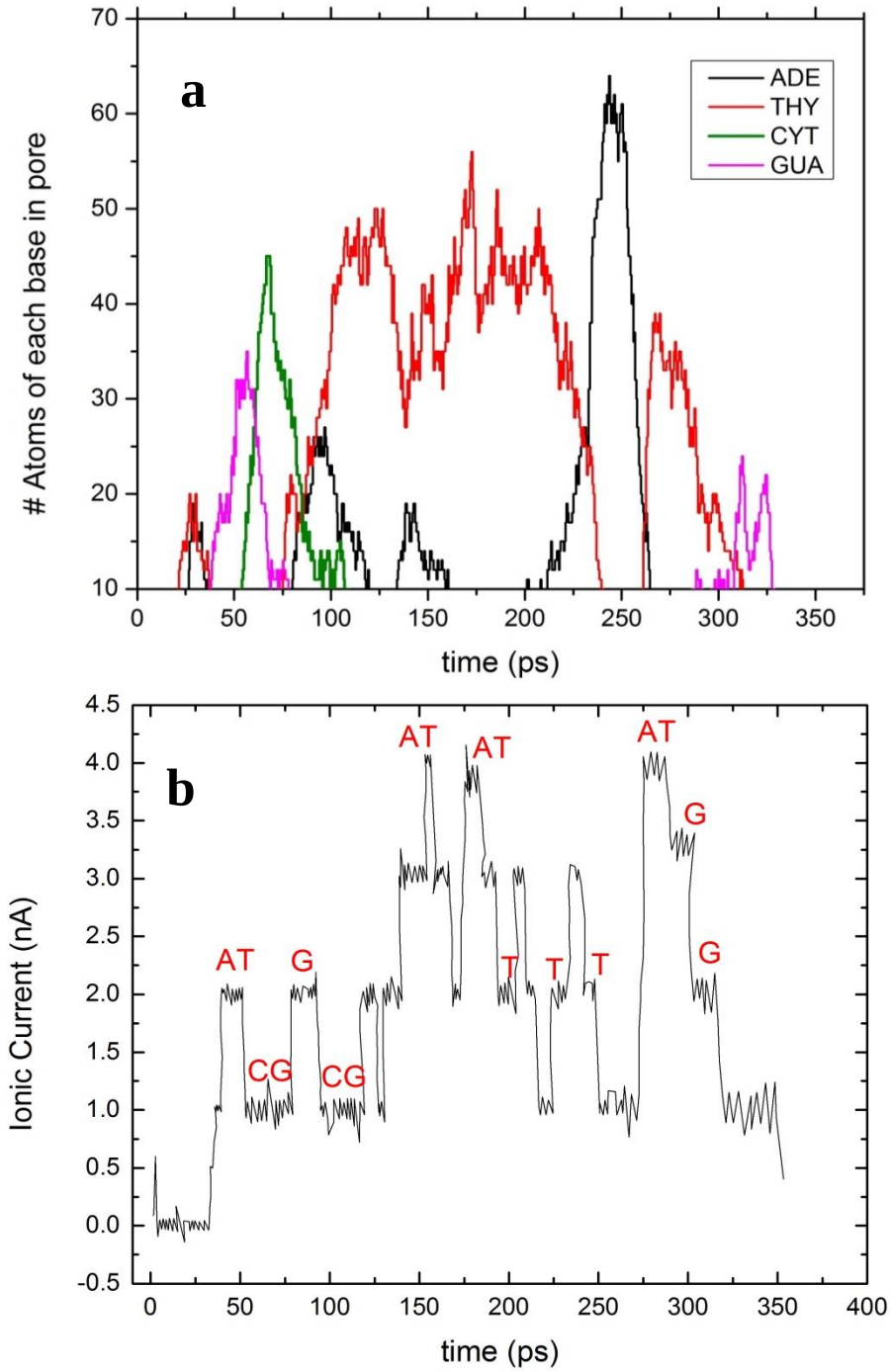

Figure 2.2.a| Passage of bases (A, C, G and T) through the MoS_2 nanopore and the residence time of each base inside the pore. **b|** Ionic current for different bases and combination of CG or AT bases.

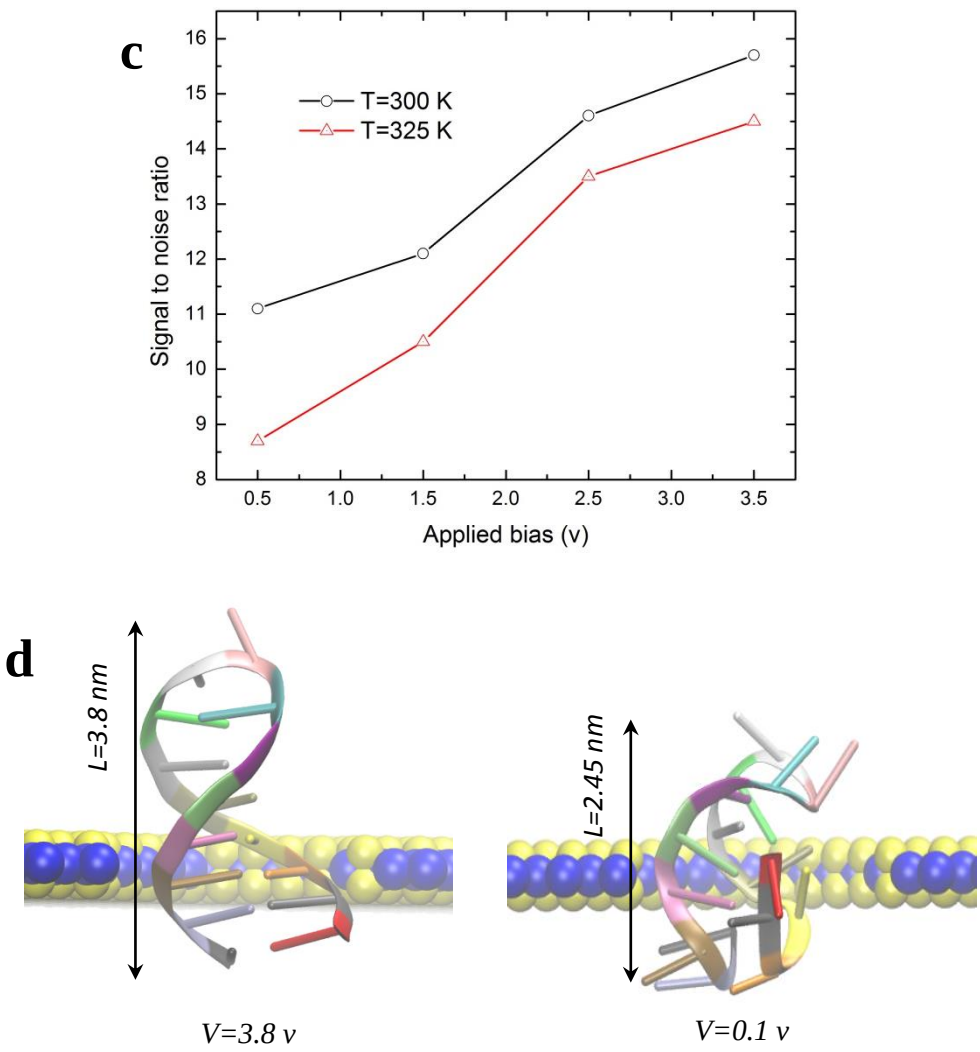

Figure 2.2 (Cont.) c| Signal to noise ratio of MoS_2 nanopore for different biases and temperatures, T=300 K and T=325 K. **d|** dsDNA modalities for two different applied voltages. The average length of dsDNA during translocation is shown for the two cases. dsDNA knots inside the pore (right); electrophoretic forces are not strong enough to stretch and translocate dsDNA.

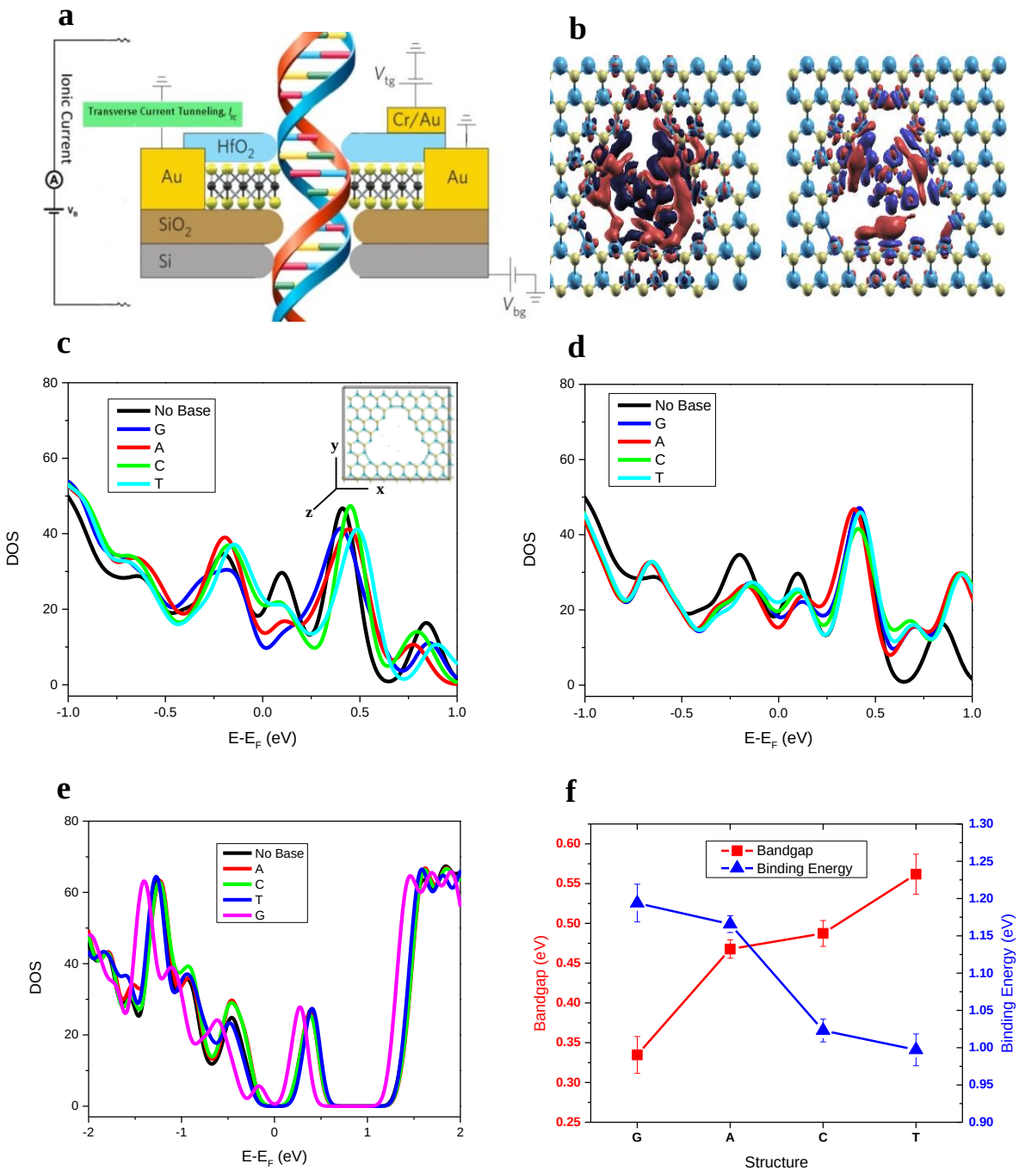

Figure 2.3.a| Schematic view of a potential DNA sensing device. **b|** 3D electronic charge density rearrangement ($\Delta\rho$) (Red and blue isosurface represent charge accumulation and depletion, respectively. Isosurface level is set at 0.0004 $Å^{-3}$.) when porous (Mo-terminated) MoS_2 interacting with G (left) and T (right). Total DOS of each base when placed **c|** horizontally (Inset: Molecular snapshot of Mo-only edge) and **d|** at 45 degree angle in porous (Mo-terminated) MoS_2. **e|** Total DOS, and **f|** band gap (left axis) and binding energy (right axis) of a pristine single-layer AMNR with each DNA base placed on the top of AMNR.

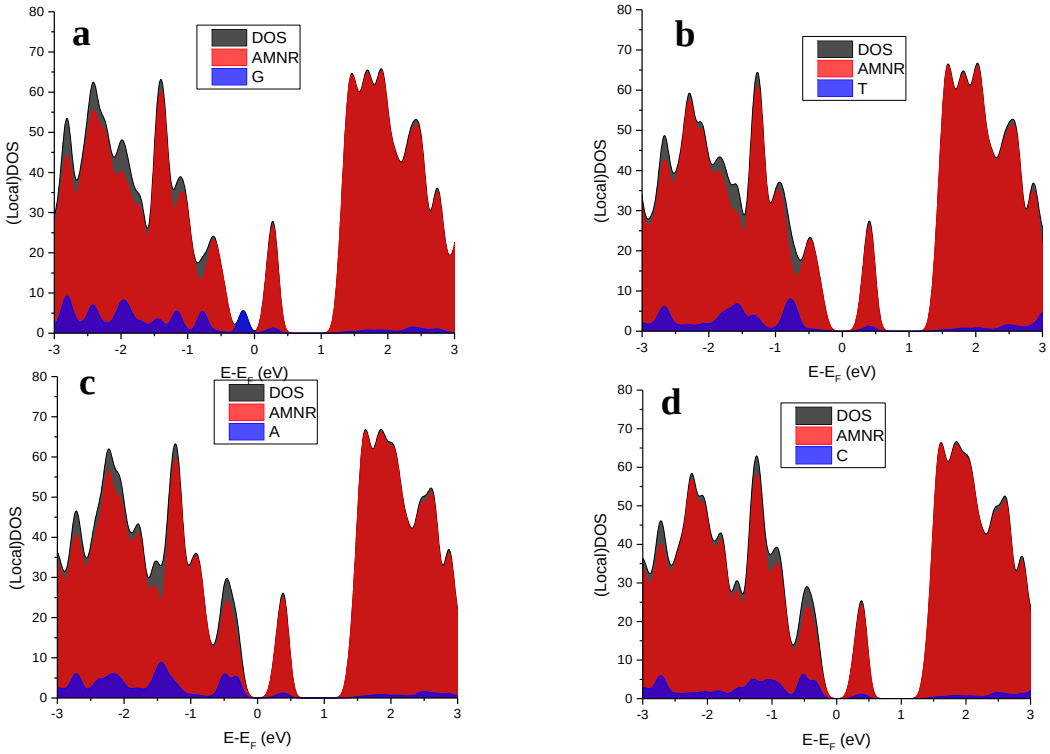

Figure 2.4. Total and local DOS of a pristine AMNR with each DNA base, **a|** Guanine (G), **b|** Thymine (T), **c|** Adenine (A), and **d|** Cytosine (C), which is placed on the top of AMNR.

Base Orientation	Bases	Binding Energy, (eV)
Horizontal	A	3.563
	C	3.246
	G	4.306
	T	1.603
Angle	A	2.587
	C	2.153
	G	2.873
	T	1.755

Table 2.1. Binding energy calculation between MoS_2 terminated with Mo-only and each base (horizontal and angle configuration)

2.7 References

1. Deamer, D. W.; Branton, D. Characterization of Nucleic Acids by Nanopore Analysis. *Accounts Chem. Res.* 2002, 35, 817-825.
2. Branton, D.; Deamer, D. W.; Marziali, A.; Bayley, H.; Benner, S. A.; Butler, T.; Di Ventra, M.; Garaj, S.; Hibbs, A.; Huang, X. H.; Jovanovich, S. B.; Krstic, P. S.; Lindsay, S.; Ling, X. S. S.; Mastrangelo, C. H.; Meller, A.; Oliver, J. S.; Pershin, Y. V.; Ramsey, J. M.; Riehn, R.; Soni, G. V.; Tabard-Cossa, V.; Wanunu, M.; Wiggin, M.; Schloss, J. A. The Potential and Challenges of Nanopore Sequencing. *Nat. Biotechnol.* 2008, 26, 1146-1153.
3. Fologea, D.; Gershow, M.; Ledden, B.; McNabb, D. S.; Golovchenko, J. A.; Li, J. L. Detecting Single Stranded DNA with a Solid State Nanopore. *Nano Lett.* 2005, 5, 1905-1909.
4. Dekker, C. Solid-State Nanopores. *Nat. Nanotechnol.* 2007, 2, 209-215.
5. Aksimentiev, A.; Heng, J. B.; Timp, G.; Schulten, K. Microscopic Kinetics of DNA Translocation through Synthetic Nanopores. *Biophys. J.* 2004, 87, 2086-2097.
6. Chen, Z.; Jiang, Y. B.; Dunphy, D. R.; Adams, D. P.; Hodges, C.; Liu, N. G.; Zhang, N.; Xomeritakis, G.; Jin, X. Z.; Aluru, N. R.; Gaik, S. J.; Hillhouse, H. W.; Brinker, C. J. DNA Translocation through an Array of Kinked Nanopores. *Nat. Mater.* 2010, 9, 667-675.
7. Heng, J. B.; Aksimentiev, A.; Ho, C.; Marks, P.; Grinkova, Y. V.; Sligar, S.; Schulten, K.; Timp, G. The Electromechanics of DNA in a Synthetic Nanopore. *Biophys. J.* 2006, 90, 1098-1106.
8. Heng, J. B.; Aksimentiev, A.; Ho, C.; Marks, P.; Grinkova, Y. V.; Sligar, S.; Schulten, K.; Timp, G. Stretching DNA Using the Electric Field in a Synthetic Nanopore. *Nano Lett.* 2005, 5, 1883-1888.
9. Min, S. K.; Kim, W. Y.; Cho, Y.; Kim, K. S. Fast DNA Sequencing with a Graphene-Based Nanochannel Device. *Nat. Nanotechnol.* 2011, 6, 162-165.
10. Venkatesan, B. M.; Bashir, R. Nanopore Sensors for Nucleic Acid Analysis. *Nat. Nanotechnol.* 2011, 6, 615-624.
11. Iqbal, S. M.; Akin, D.; Bashir, R. Solid-State Nanopore Channels with DNA Selectivity. *Nat. Nanotechnol.* 2007, 2, 243-248.
12. Li, J. L.; Gershow, M.; Stein, D.; Brandin, E.; Golovchenko, J. A. DNA Molecules and Configurations in a Solid-State Nanopore Microscope. *Nat. Mater.* 2003, 2, 611-615.
13. Meller, A.; Nivon, L.; Brandin, E.; Golovchenko, J.; Branton, D. Rapid Nanopore Discrimination between Single Polynucleotide Molecules. *Proc. Natl. Acad. Sci. U. S. A.* 2000, 97, 1079-1084.
14. Sathe, C.; Zou, X. Q.; Leburton, J. P.; Schulten, K. Computational Investigation of DNA Detection Using Graphene Nanopores. *ACS Nano* 2011, 5, 8842-8851.
15. Siwy, Z. S.; Davenport, M. Nanopores Graphene Opens up to DNA. *Nat. Nanotechnol.* 2010, 5, 697-698.
16. Wells, D. B.; Belkin, M.; Comer, J.; Aksimentiev, A. Assessing Graphene Nanopores for Sequencing DNA. *Nano Lett.* 2012, 12, 4117-4123.
17. Geim, A. K.; Novoselov, K. S. The Rise of Graphene. *Nat. Mater.* 2007, 6, 183-191.
18. Nelson, T.; Zhang, B.; Prezhdo, O. V. Detection of Nucleic Acids with Graphene Nanopores: Ab Initio Characterization of a Novel Sequencing Device. *Nano Lett.* 2010, 10, 3237-3242.
19. Schneider, G. F.; Kowalczyk, S. W.; Calado, V. E.; Pandraud, G.; Zandbergen, H. W.; Vandersypen, L. M. K.; Dekker, C. DNA Translocation through Graphene Nanopores. *Nano Lett.* 2010, 10, 3163-3167.
20. Traversi, F.; Raillon, C.; Benameur, S. M.; Liu, K.; Khlybov, S.; Tosun, M.; Krasnozhon, D.; Kis, A.; Radenovic, A. Detecting the Translocation of DNA through a Nanopore Using Graphene Nanoribbons. *Nat. Nanotechnol.* 2013, 8, 939-945.
21. Saha, K. K.; Drndic, M.; Nikolic, B. K. DNA Base-Specific Modulation of Microampere Transverse Edge Currents through a Metallic Graphene Nanoribbon with a Nanopore. *Nano Lett.* 2012, 12, 50-55.

22. Prasongkit, J.; Grigoriev, A.; Pathak, B.; Ahuja, R.; Scheicher, R. H. Transverse Conductance of DNA Nucleotides in a Graphene Nanogap from First Principles. *Nano Lett.* 2011, 11, 1941-1945.
23. Banerjee, S.; Shim, J.; Rivera, J.; Jin, X. Z.; Estrada, D.; Solovyeva, V.; You, X.; Pak, J.; Pop, E.; Aluru, N.; Bashir, R. Electrochemistry at the Edge of a Single Graphene Layer in a Nanopore. *ACS Nano* 2013, 7, 834-843.
24. Tsutsui, M.; Taniguchi, M.; Yokota, K.; Kawai, T. Identifying Single Nucleotides by Tunnelling Current. *Nat. Nanotechnol.* 2010, 5, 286-290.
25. Tsutsui, M.; Taniguchi, M.; Kawai, T. Transverse Field Effects on DNA-Sized Particle Dynamics. *Nano Lett.* 2009, 9, 1659-1662.
26. Kumar, B.; Min, K.; Bashirzadeh, M.; Farimani, A. B.; Bae, M. H.; Estrada, D.; Kim, Y. D.; Yasaei, P.; Park, Y. D.; Pop, E.; Aluru, N. R.; Salehi-Khojin, A. The Role of External Defects in Chemical Sensing of Graphene Field-Effect Transistors. *Nano Lett.* 2013, 13, 1962-1968.
27. Obradovic, B.; Kotlyar, R.; Heinz, F.; Matagne, P.; Rakshit, T.; Giles, M. D.; Stettler, M. A.; Nikonov, D. E. Analysis of Graphene Nanoribbons as a Channel Material for Field-Effect Transistors. *Appl. Phys. Lett.* 2006, 88.
28. Radisavljevic, B.; Radenovic, A.; Brivio, J.; Giacometti, V.; Kis, A. Single-Layer MoS_2 Transistors. *Nat. Nanotechnol.* 2011, 6, 147-150.
29. Li, J. P.; Zhang, Y.; Yang, J. K.; Bi, K. D.; Ni, Z. H.; Li, D. Y.; Chen, Y. F. Molecular Dynamics Study of DNA Translocation through Graphene Nanopores. *Phys. Rev. E* 2013, 87.
30. Lv, W. P.; Chen, M. D.; Wu, R. A. The Impact of the Number of Layers of a Graphene Nanopore on DNA Translocation. *Soft Matter* 2013, 9, 960-966.
31. Paik, K. H.; Liu, Y.; Tabard-Cossa, V.; Waugh, M. J.; Huber, D. E.; Provine, J.; Howe, R. T.; Dutton, R. W.; Davis, R. W. Control of DNA Capture by Nanofluidic Transistors. *ACS Nano* 2012, 6, 6767-6775.
32. Liu, K.; Feng, J. D.; Kis, A.; Radenovic, A. Atomically Thin Molybdenum Disulfide Nanopores with High Sensitivity for DNA Trans Location. *ACS Nano* 2014, 8, 2504-2511.
33. Plimpton, S. Fast Parallel Algorithms for Short-Range Molecular-Dynamics. *J. Comput. Phys.* 1995, 117, 1-19.
34. MacKerell, A. D.; Banavali, N. K. All-Atom Empirical Force Field for Nucleic Acids: Ii. Application to Molecular Dynamics Simulations of DNA and Rna in Solution. *J. Comput. Chem.* 2000, 21, 105-120.
35. Stewart, J. A.; Spearot, D. E. Atomistic Simulations of Nanoindentation on the Basal Plane of Crystalline Molybdenum Disulfide (MoS_2). *Model. Simul. Mater. Sci. Eng.* 2013, 21.
36. Stuart, S. J.; Tutein, A. B.; Harrison, J. A. A Reactive Potential for Hydrocarbons with Intermolecular Interactions. *J. Chem. Phys.* 2000, 112, 6472-6486.
37. Soler, J. M.; Artacho, E.; Gale, J. D.; García, A.; Junquera, J.; Ordejón, P.; Sánchez-Portal, D. The Siesta Method for Ab Initio Order-N Materials Simulation. *Journal of Physics: Condensed Matter* 2002, 14, 2745.
38. Lee, J.-H.; Choi, Y.-K.; Kim, H.-J.; Scheicher, R. H.; Cho, J. H. Physisorption of DNA Nucleobases on H-Bn and Graphene: Vdw-Corrected Dft Calculations. *The Journal of Physical Chemistry C* 2013.
39. Le, D.; Kara, A.; Schröder, E.; Hyldgaard, P.; Rahman, T. S. Physisorption of Nucleobases on Graphene: A Comparative Van Der Waals Study. *Journal of Physics: Condensed Matter* 2012, 24, 424210.
40. Min, K.; Farimani, A. B.; Aluru, N. Mechanical Behavior of Water Filled C60. *Appl. Phys. Lett.* 2013, 103, 263112.
41. Perdew, J. P.; Burke, K.; Ernzerhof, M. Generalized Gradient Approximation Made Simple. *Physical Review Letters* 1996, 77, 3865-3868.
42. Troullier, N.; Martins, J. L. Efficient Pseudopotentials for Plane-Wave Calculations. *Physical Review B* 1991, 43, 1993-2006.

43. Monkhorst, H. J.; Pack, J. D. Special Points for Brillouin-Zone Integrations. *Physical Review B* 1976, 13, 5188-5192.
44. Smeets, R. M. M.; Keyser, U. F.; Dekker, N. H.; Dekker, C. Noise in Solid-State Nanopores. *Proc. Natl. Acad. Sci. U. S. A.* 2008, 105, 417-421.
45. Cracknell, J. A.; Japrung, D.; Bayley, H. Translocating Kilobase Rna through the Staphylococcal Alpha-Hemolysin Nanopore. *Nano Lett.* 2013, 13, 2500-2505.
46. Lu, B.; Albertorio, F.; Hoogerheide, D. P.; Golovchenko, J. A. Origins and Consequences of Velocity Fluctuations During DNA Passage through a Nanopore. *Biophys. J.* 2011, 101, 70-79.
47. Li, Z.; Chen, Y.; Li, X.; Kamins, T. I.; Nauka, K.; Williams, R. S. Sequence-Specific Label-Free DNA Sensors Based on Silicon Nanowires. *Nano Lett.* 2004, 4, 245-247.
48. Fritz, J.; Cooper, E. B.; Gaudet, S.; Sorger, P. K.; Manalis, S. R. Electronic Detection of DNA by Its Intrinsic Molecular Charge. *Proc. Natl. Acad. Sci. U. S. A.* 2002, 99, 14142-14146.
49. Zhou, Y.; Yang, P.; Zu, H.; Gao, F.; Zu, X. Electronic Structures and Magnetic Properties of MoS_2 Nanostructures: Atomic Defect, Nanohole, Nanodot and Antidot. *Physical Chemistry Chemical Physics* 2013.
50. Kou, L.; Tang, C.; Zhang, Y.; Heine, T.; Chen, C.; Frauenheim, T. Tuning Magnetism and Electronic Phase Transitions by Strain and Electric Field in Zigzag MoS_2 Nanoribbons. *The Journal of Physical Chemistry Letters* 2012, 3, 2934-2941.
51. Dolui, K.; Pemmaraju, C. D.; Sanvito, S. Electric Field Effects on Armchair MoS_2 Nanoribbons. *ACS Nano* 2012, 6, 4823-4834.

CHAPTER 3: Electro-Mechanical Signatures for DNA Sequencing through a Mechano-Sensitive Nanopore[†]

3.1 Introduction

Nanopore-based DNA sequencing is attractive as it is a label-free, single-molecule approach that can be utilized for high precision DNA analysis.[1-3] Biological nanopores have been investigated for DNA base detection since they offer several advantages for single-molecule DNA analysis.[2-8] First, mutagenesis can be used to tailor the physical and chemical properties of biological nanopores;[1, 8] Second, biological nanopores are synthesized by cells with an atomic level precision that may not be possible with solid-state fabrication approaches;[9] Third, crystallography data of protein channels is available at Angstrom length scales.[1, 2, 4, 9] The first biological nanopore investigated for sequencing DNA was staphylococcal Alpha-Hemolysin (αHL) protein pore[10]; an applied potential translocated a ssDNA molecule through the pore giving rise to modulation of the ionic current.[5] αHL cylindrical beta barrel (with a diameter of 2 nm and length of 5 nm) is not tight enough to yield a distinguishable ionic current specific to individual nucleotides and therefore, exhibits small current differences between the nucleotides. Another well-researched biological

[†] A. Barati Farimani, M. Heiranian and N. R. Aluru, ``Electromechanical signatures for DNA sequencing through a mechanosensitive nanopore'', Journal of Physical Chemistry Letters, Vol. 6, No. 4, pp. 650-657, 2015.

nanopore for DNA sequencing is Mycobacterium Smegmatis Porin A (MspA).[11, 12] MspA has been shown to provide better ionic current signals for differentiating nucleotides as its pore structure includes a tighter 1.2 nm constriction region.[12] In contrast to synthetic nanopores, such as graphene[13-15] and MoS_2 nanopores[16, 17] where DNA base could be electronically read through transverse tunneling current,[18-20] ionic current is the only signature that has been acquired in biological nanopores, e.g. in MspA or αHL. The noise in the system and the presence of multiple bases in these nanopores make detection of a single DNA base difficult.[1] Acquiring another signal, in addition to ionic currents, for DNA detection using biological pores can significantly increase the accuracy of DNA sequencing.

The sensing of mechanical tension and force within a cell's environment is mostly mediated by a highly specialized class of membrane proteins known as Mechanosensitive (MS) ion channels.[12] MS channels were shown to be able to transduce mechanical tension into an electrochemical response[21]. When a cell membrane is under tension due to osmotic down shock, MS channels relieve the pressure of the cell by gating and forming a pore as big as 3 nm in diameter.[22, 23] Among several types of MS channels, the mechano-sensitive channel of large conductance (MscL) of prokaryotes has been most extensively characterized.[22, 24-29]

Here, we demonstrate for the first time that a MscL nanopore can be used for detection of DNA bases by modulating tension and strain in MscL. Tension in the MscL membrane, along with the ionic currents, can be used for more precise sequencing of DNA (see the cartoon representation of the system in Figure 3.1a). Unlike αHL or MspA, that are structurally wide open pores, initially closed MscL pore opens as a ssDNA translocates through the pore due to an applied electric field. MscL adjusts its pore size to the size of DNA bases during the translocation. The distinct tension in the protein associated with each nucleotide can be sensed through the strain and tension induced

in the lipid bilayer. Recently,[30] MscL has been successfully embedded and characterized inside a droplet interface bilayer (DIB). It has been shown that the induced tension inside MscL is translated into a change in the triple point angle of DIB. By monitoring the angle change in DIB during DNA translocation, induced tension can be measured and quantified.

Two well-known challenges of DNA detection through nanopores are the fast translocation speed of DNA and noise.[1, 2, 9] Experiments have shown that DNA passes through αHL with a speed of 1base/μs, requiring MHz signal measurements to differentiate between nucleotide types.[1, 2] The presence of multiple bases in the pore and thermal fluctuations in the system generate noise in the ionic current, making detection difficult. A MscL nanopore is flexible[31] and it adjusts to DNA size, causing a reduction in the speed of translocation. We demonstrate the slower translocation of DNA in MscL by comparing the results in MspA nanopore. Furthermore, we demonstrate the effect of pore flexibility by comparing the results in MscL and MspA pores.

3.2 Methods

We performed molecular dynamics (MD) simulations with NAMD 2.6 using the Petascale Blue Waters machine.[32] A typical simulation set up consisting of ssDNA, MscL protein, lipid bilayer, water and ions (~600,000 atoms) is shown in Figure 3.1.b. We used the closed MscL model provided by Sukharev et al. and the crystal structure was obtained from this reference.[12, 21] the C alpha segments were eliminated to obtain a reduced version of MscL.[12, 21] A lipid bilayer (POPC) patch was created (10 nm×10 nm) to accommodate the protein and solvated by a 25-Å thick slab of water on each side of the membrane. MscL with the center of the pore aligned along the membrane normal axis (z-axis) was placed in the lipid bilayer using Visual Molecular Dynamics (VMD).[33] We ran the simulation for 40 ns to equilibrate the system of lipid bilayer and protein.

This long equilibration makes sure that the protein is firmly placed in the membrane without any membrane leakage. Using the equilibrated lipid-protein system, ssDNA was placed at the mouth of the MscL nanopore with the ssDNA axis (z-direction) aligned along the protein axis (Figure 3.1.b). Then, ssDNA (one at a time), MscL and lipid bilayer are submersed in water and salt ionic solution. The ionic concentration of NaCl is 0.5 M. We used polydA(60), polydC(60), polydT(60) and polydG(60) to create 4 simulation boxes (Figure 3.1.b) differing only in ssDNA type. We used the CHARMM27 force field[34] parameters for the protein, nucleic acid (DNA), TIP3P water molecules and ions. SHAKE algorithm was used to maintain the rigidity of the water molecules. Periodic boundary condition was applied in all the three directions. The cut off distance for the LJ interactions was 15 Å. The long-range electrostatic interactions were computed by using the Particle-Mesh-Ewald (PME) method. The time step is selected to be 1 fs. For each simulation, energy minimization was performed for 100,000 steps. System was then equilibrated for 5 ns with NPT ensemble at 1 atm pressure and 300 K temperature. NPT simulation ensures that the water concentration is equal to the bulk value of 1 g/cm^3. The simulation was then performed in NVT ensemble. Temperature was maintained at 300 K by applying the Nosè-Hoover thermostat with a time constant of 0.1 ps. Before applying the electric field, equilibration for 2 ns was performed in NVT. Production simulations were performed by applying an external electric field in the z-direction. The external electric fields are reported in terms of a transmembrane voltage difference $V = EL_z$, where E is the electric field strength and L_z is the length of the simulation system in the z-direction.[14] For computational efficiency, we used steered molecular dynamics (SMD) to pull DNA with a very slow velocity of 0.00001 Å/fs. The steering forces were applied to all the atoms (both charged and uncharged) of the first base entering the pore. We monitored the time-dependent ionic current, $I(t)$, in the pore. We computed the ionic current through the nanopore by using the

definition of current, $I=dq/dt$, as $I(t)=\frac{1}{L_z}\sum_{i=1}^{n} q_i\left[\frac{z_i(t+\delta t)-z_i(t)}{\delta t}\right]$, where the sum is for all the ions, δt is chosen to be 5 ps, and z_i and q_i are the z-coordinate, charge of ion i, and n is the total number of ions, respectively. The ionic current data is averaged for each base, and the average current per base was reported.

To characterize the tension in the protein due to nucleotide translocation, the interaction forces between MscL helices and DNA bases were calculated. Subunits of MscL containing M1, M2 and S1 helices are shown in different colors in Figure 3.1.c. Since MscL has five identical subunits, pair interaction calculations were carried out separately for each subunit. Both Coulombic and VdW (Van der Waals) forces by DNA bases on the inner transmembrane helix (M1) and the S1 helix (Figure 3.1.c) were computed every pico second and then averaged over the entire DNA translocation time for each subunit of MscL. Only the inner M1 and S1 helices which create the constriction regions (Figure 3.1.c) inside MscL were considered and the outer helices (M2) were ignored. The radial components of the calculated forces directed away from the center of the protein channel were then spatially averaged over all the five identical subunits of MscL to obtain an average force per subunit corresponding to each DNA base type. The nature of these forces is tensile and, therefore, the induced tension in MscL is transferred to the membrane since its segments are radially pushed outward by ssDNA. We refer to these interaction forces between ssDNA and protein lining residues as tension. It's notable that the origin of this tension is different from the tension defined as the membrane tension which causes MscL to gate.

3.3 Results and Discussion

We found 4 different tension signals for bases A, C, G and T which can be used for detecting and discriminating between nucleotides (Figure 3.1.d). We observed that the maximum induced force is from base T, and the order of the induced forces is T>G>C>A. The force between ssDNA and MscL is from VdW and electrostatic interactions. Prior work has shown that a 70 pN force can open the MscL protein channel, therefore, the range of 20-120 pN forces induced from translocation of different bases should be adequate for the discrimination of bases.[23, 28] Also, using magnetic tweezers, it's possible to measure forces as small as 50 fN,[35] therefore, forces of 20 pN magnitude should be measurable. These forces on the wall of the protein channel have a local effect on the lipid bilayer. The effect of the forces and tension is maximum on the lipids in the vicinity of MscL, therefore, the force measurements need to be done on the lipids, close to the protein. To understand why base T induces a maximum force, we investigated the structure and interaction parameters of each base. Base T has two protruding oxygen atoms and this is the maximum number among all the bases (more information about the structure of bases and their interaction strength can be found in the APPENDIX B). Oxygen plays a significant role in both VdW and electrostatic forces between MscL lumen lining residues and nucleotides. The Lennard-Jones (LJ) energy interaction parameter of the oxygen atom is higher (ε_O=0.210) compared to all the other atoms (ε_H=0.05, ε_C=0.1, ε_N=0.17)[36] of the base. Base A has only hydrogen terminations (no oxygen), therefore, it has the lowest interactive forces among all the bases (Figure 3.1.d). Comparing the termination structure of bases G and C reveals the existence of two nitrogens and one oxygen for base G, and only one nitrogen and oxygen for base C . The extra nitrogen in base G compared to base C gives rise to the higher interaction forces between MscL and base G and this fact explains the interaction forces order (G>C).

Unlike other biological pores (MspA or αHL) and solid-state nanopores which are normally-open, MscL has a flexible pore as it opens according to the size of the base, i.e., in our simulations, initially, MscL opens with evolving pore radii during the translocation of the first 5-10 bases. In the calculation of forces, we ignored the force data from the initial entry of ssDNA (for all PolydA, PolydC, PolydG and PolydT) into MscL because these forces are not in equilibrium and the pore exhibits transient dynamics. In Figure 3.2.a, we show three states of the pore representing the pore opening and expansion. State 1, state 2 and state 3 refer to closed, transient opening (while the first bases of PolydA are about to exit the cytoplasmic segment of MscL) and fully-opened by polydA states, respectively. Interestingly, MscL pore has an elliptical shape when it is fully open (Figure 3.2.a). It is notable that in normal operation of MscL, in both intermediate and open states, MscL pore is circular and symmetrical.

We computed the average ionic current for each base (averaged during the translocation of each polydna with 60 bases) and found the current to decrease in the order, C>A>G>T. The ionic currents of bases C and A are close to each other and higher compared to bases G and T. Most of the ions that passed through the pore are cations which are dragged by the negatively charged backbone of the DNA during the translocation of all the 60 bases. Very small number of ions are trapped between the bases and dragged down the pore. Water molecules are observed in the pore all around the DNA. To illustrate the effect of pore elasticity of MscL on the quality of the acquired ionic current signal, we compared the ionic current signals for both MscL and MspA nanopores (APPENDIX B). According to the literature, MspA has been found to be the best biological pore, reported so far, for DNA detection.[2, 11, 37, 38] The maximum and minimum current difference, ΔI, is 113.1 pA and 189.2 pA for MspA and MscL, respectively (APPENDIX B). Higher ΔI for MscL compared to MspA shows a better detection signal for MscL. We also investigated the noise by

computing the signal to noise ratio, SNR, for both MscL and MspA pores. SNR is 6.13 (with $I_{noise,RMS}$=30.99 pA) and 4.21 (with $I_{noise,RMS}$=26.84 pA) for MscL and MspA, respectively (APPENDIX B). To compare the noise for static and moving ssDNA, we performed simulation of moving ssDNA by applying bias (500 mv) and static ssDNA when ssDNA is inside MscL and the applied bias is zero. We used the same method of noise calculation that we used in SNR computation (APPENDIX B). The ratio of noise generated in static ssDNA case ($I_{noise, RMS: Static}$) and noise generated in moving ssDNA case ($I_{noise, RMS:Moving}$) , is $I_{noise, RMS:Static} / I_{noise, RMS:Moving}$ =0.985 which means the noise is very similar in both cases. The signal becomes strong (or the SNR is improved) when a strong bias (no SMD) is applied leading to a high DNA passage rate. Therefore, DNA translocation rate is indirectly related to the strength of the signal and consequently the signal to noise ratio.

The fluctuations in current are dependent on the slit diameter, slit length and the charged lining residues of the slit. In MscL, the diameter of the pore is flexible and adaptive to the ssDNA nucleotide type. We believe this flexibility, and perhaps selectivity reduces the noise level, as noted in the SNR comparison of MspA and MscL. The distinctive ionic current features in MscL can be attributed to two fundamental differences between the operation of MscL and other biological nanopores. First, in MscL, the pore is initially closed and it opens due to the electric field-mediated translocation of ssDNA, unlike in other nanopores where a fixed pore diameter is employed. Second, unlike MspA, Alpha-Hemolysin, Si_3N_4, graphene and MoS_2, MscL has two constriction regions which open during ssDNA translocation (see Figure 3.1.c). Bases C and A have larger ionic currents (Figure 3.2.b), revealing the fact that these bases are capable of transporting ions through the constriction regions with higher rates. To understand how the MscL pore opens during the translocation of bases, we time-averaged the pore radius during ssDNA translocation (Figure

3.3.a). Base A creates the largest pore diameter and base T creates the smallest pore diameter in constriction 1, constriction 2 and open regions of the MscL channel. (Figure 3.3.a). The minimum ionic current is for base T (Figure 3.2.b) and this is consistent with the minimum opening of the pore induced by base T in all the segments of MscL (Figure 3.3.a). The order of pore radii opened by ssDNA in constriction regions 1, 2 and open region is A>G>C>T. Bases A and G (purines) have an additional ring compared to bases C and T (pyrimidines) which gives rise to larger base area of purines and the consequent larger pore radii in MscL compared to pyrimidines (APPENDIX B).

The normal activation of MscL by tension in the lipid bilayer has two open states – intermediate and fully-open. In the closed state, the S1 segments form a bundle, and the crosslinking of S1 segments prevents the opening of the channel (Figure 3.1.c). When a tension is applied to the membrane, the transmembrane barrel-like structure expands and stretches apart the S1-M1 region allowing the channel to open (Figure 3.1.c). The transition from the closed to the intermediate state includes small movements of the M1 helix. Further transitions to the open states are characterized by large movements in both M1 and M2. The gating pathway for ssDNA translocation through MscL is, however, different. We compared the conformational changes occurring in the pore lumen due to ssDNA translocation with the normal operation of MscL (Figure 3.3.b). The average pore radius for the 3 stable structures of MscL and ssDNA-opened MscL are shown in Figure 3.3.b. The minimum pore radii are 0.0 Å, 2.1 Å and 12.5 Å for the closed, intermediate and open states, respectively (Figure 3.3.b). For the ssDNA translocation case, MscL radius is between closed and intermediate states (Figure 3.3.b). It can be inferred from the radius of ssDNA–opened MscL that this state of MscL is not stable; tending to relax to closed state. Another striking difference between ssDNA-opened and normally-opened MscL is the mechanism of gating. In the

normal operation of MscL, transmembrane helices M1 (Figure 1c) rotate and tilt such that they become more aligned with the plane of the membrane and M2 helices also tilt but to a much lower degree[23, 28] resulting in a shortened length of MscL (Figure 3.3.b). In the ssDNA-opened MscL, the initially closed-state length of MscL does not change and all M1, M2 and S1 segments expand radially (Figure 3.3.b).

An important challenge of DNA sequencing through a nanopore is to decrease the high speed of translocation. If the translocation speed can be reduced to about one base per millisecond, then single-base detection can be more easily performed in experiments. It has been shown that translocation speeds can be reduced by increasing the solvent viscosity or decreasing the temperature,[2] but these methods could not reduce the translocation speed to a desired level.[2] To reduce the translocation speed, an initially-closed, and a translocation-induced elastic opening of the pore could be a potential solution. In this regard, MscL has the potential to significantly reduce the translocation speed. We compared the translocation speed of ssDNA through MscL and MspA[39] (Figure 3.4). MspA is an octameric protein with a pore suitable for DNA sequencing[39, 40] (Figure 3.4.a). We simulated DNA translocation keeping all conditions identical and only differing in the type of the protein. Two biases of 500 mV and 1.0 V were applied to both simulation cases to compare their speed of translocation. Translocation speed of ssDNA in MscL is 11-17 times slower than in MspA (Figure 3.4.b and 3.4.c). For the bias of 500 mV, the speed of translocation is 0.129 Å/ns and 2.24 Å/ns for MscL and MspA, respectively (17.36 times slower in MscL than in MspA). The reduction in speed can be attributed to two fundamental differences between these pores: 1. The comparison between MscL and MspA protein structures reveals the existence of multiple constrictions in MscL with near zero diameters where as in MspA, only one constriction region with a 1.2 nm diameter is present (Figure 3.4.a). These structural differences help reducing

the speed of translocation in MscL to a large extent. 2. MspA has an open pore structure and remains roughly intact during translocation, whereas MscL opens to an extent just enough to accommodate the ssDNA bases. Since ssDNA-opened MscL does not reach an intermediate stable state, it tends to close during DNA translocation, which results in exerting force on ssDNA and reducing the speed. Based on the interaction force calculations, LYS 31, GLU 9, ARG 13 and ASP 18 residues in MscL have the highest interaction forces with ssDNA, giving rise to slower translocation of ssDNA. Interestingly, all these residues are located in constriction regions 1 and 2. It is notable that the S domain plays a critical role in the creation of highly constricted regions in MscL. The highly constricted regions in MscL give rise to the selectivity of the passage of ions for each nucleotide which increases the SNR. Also, the highly constricted regions created by S1 domain have a significant effect on reducing the DNA translocation speed.

3.4 Conclusion

We have shown that a mechanical signature, namely tension in the membrane, can be effective for DNA detection through a mechano-sensitive channel of large conductance, MscL. Four distinct force signals were detected for bases with forces decreasing in the order T> G> C>A. An initially-closed MscL opens to ssDNA due to electric-field mediated translocation and the pore geometry adapts to the size of each base. Ionic current signal is also distinct for each base, making MscL pore amenable for detecting bases with two parallel signals, namely, membrane tension and ionic current. We found a completely different gating mechanism of MscL during ssDNA translocation compared to its normal operation. The translocation speed of DNA in MscL is roughly one order of magnitude slower compared to that in MspA.

3.5 Figures

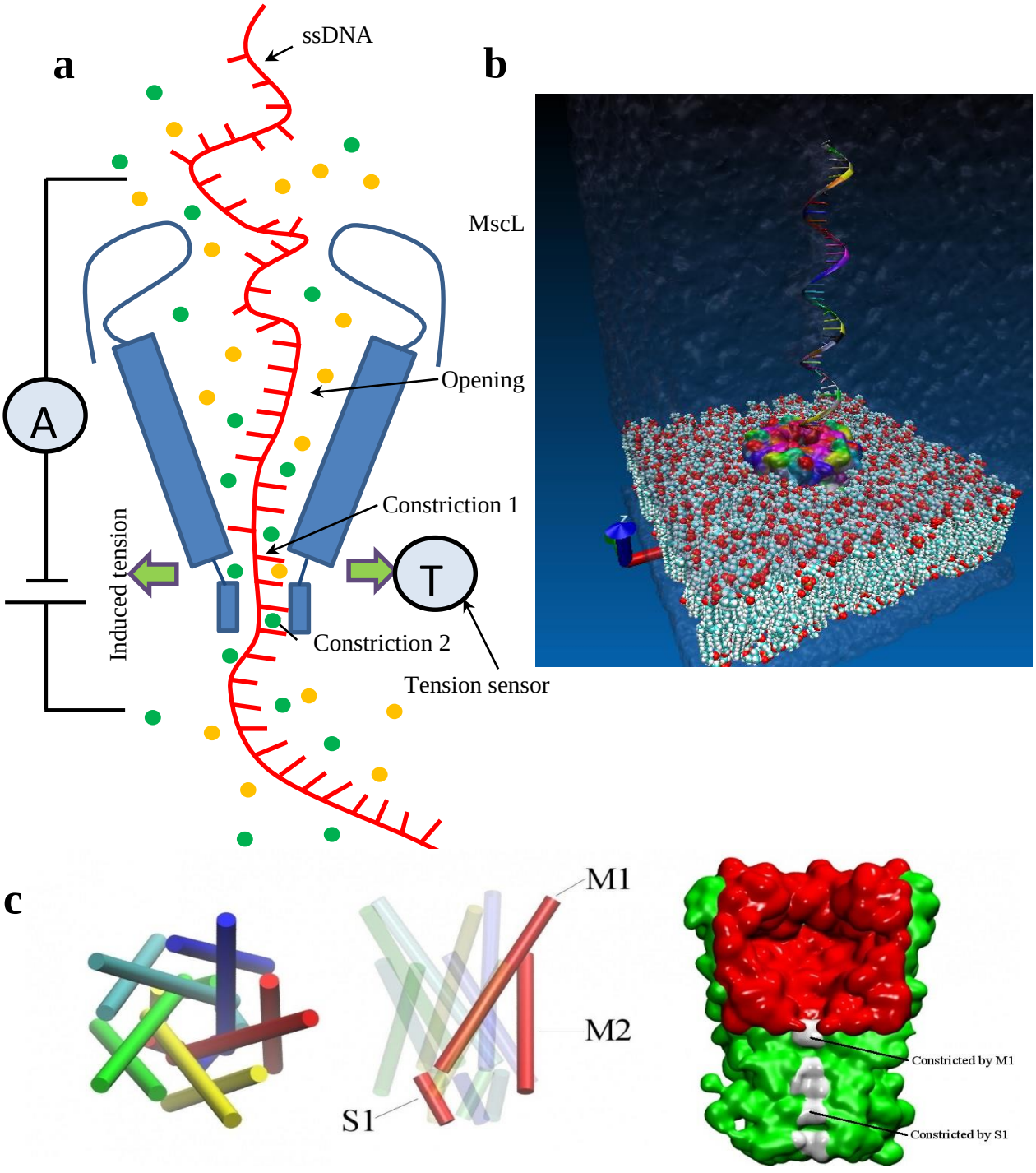

Figure 3.1.a| Cartoon representation of the system (MscL, ssDNA, ions) demonstrating two parallel signals: tension and ionic current. **b|** Visualization of the simulation setup comprising ssDNA, MscL protein, lipid bilayer and water. **c|** Left: Top view of MscL. Middle: side view of MscL with the designation of M1 and S1 helices. Right: Pore architecture of MscL, cut in the middle and the location of the two constriction regions of MscL.

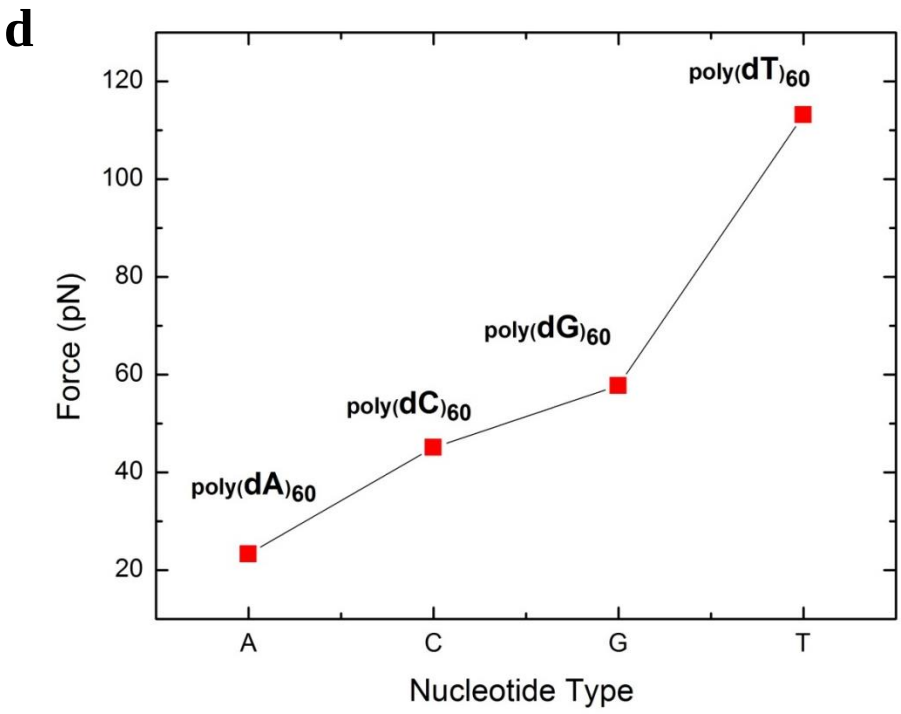

Figure 3.1.(Cont). **d|** Force (averaged) induced in the membrane due to the presence of each base in MscL.

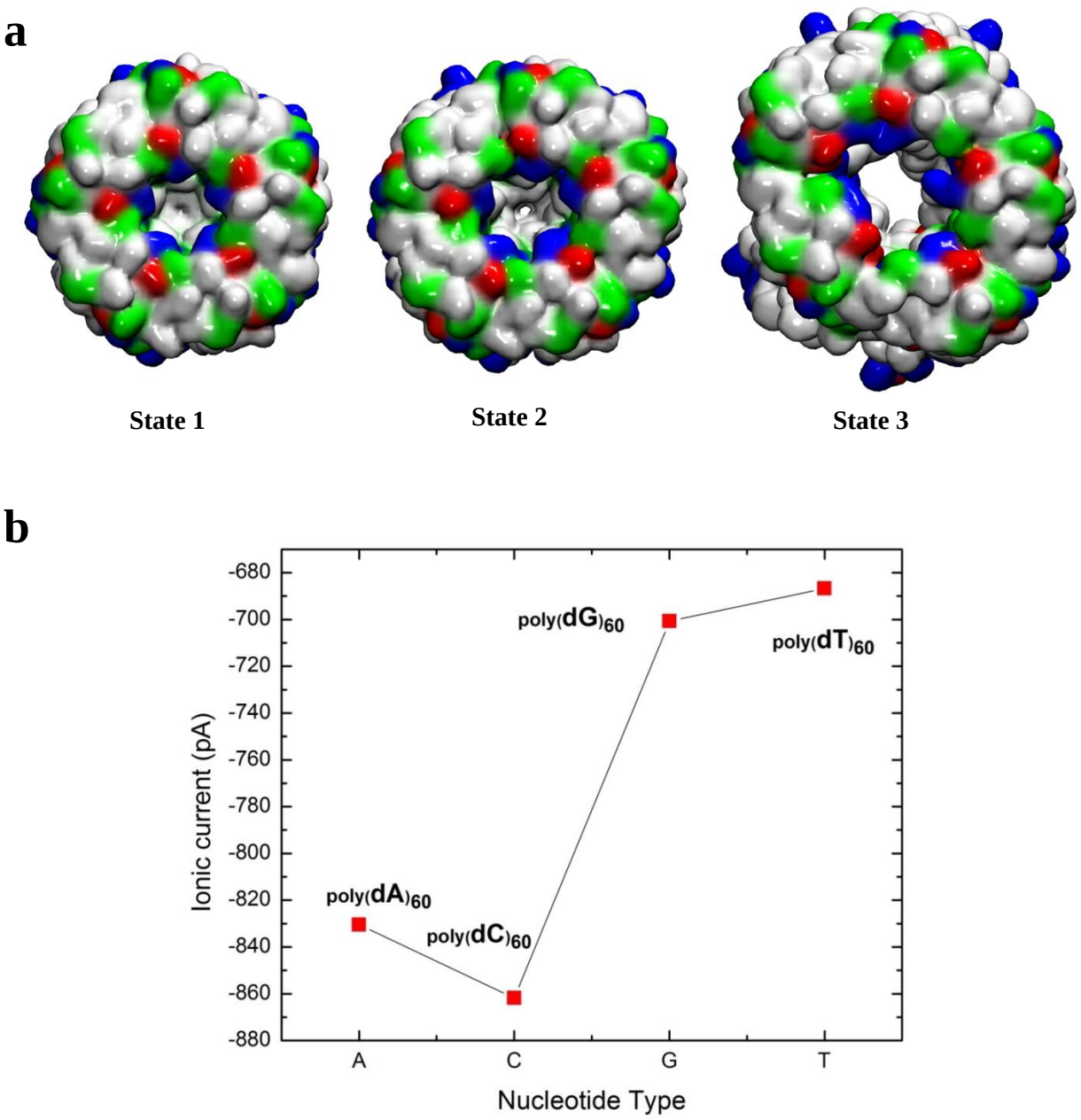

Figure 3.2.a| Three representative states of the MscL pore and the extent to which it opens, *state1*: initially-closed state prior to the ssDNA entry, *state 2*: the first base of ssDNA entered the pore and is about to exit the cytoplasmic segment of the pore (the pore opens partially), *state 3*: ssDNA with 60 bases (here, polydA) translocated and pore has an elliptical shape. **b|** Average ionic current for different nucleotide types.

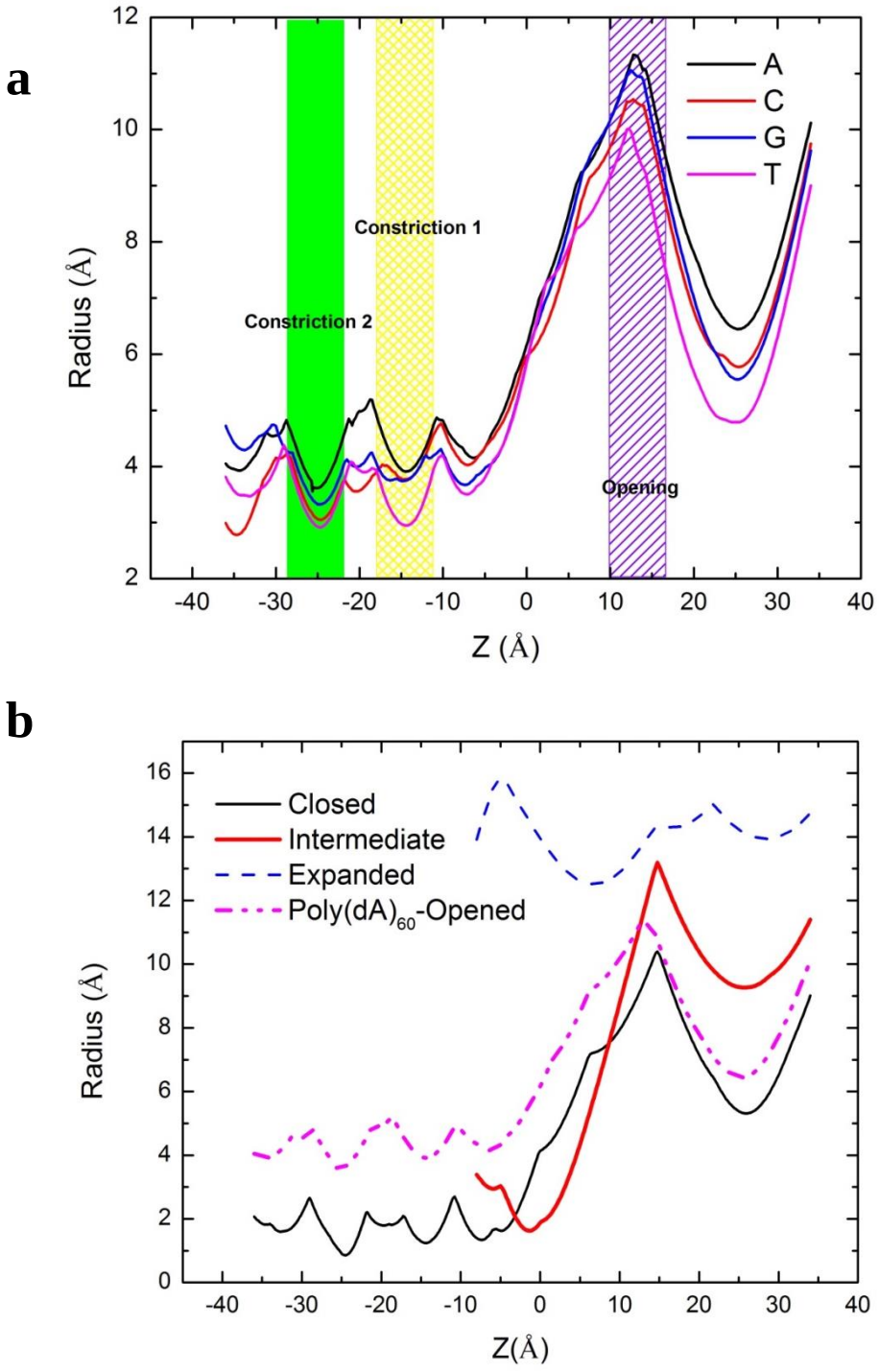

Figure 3.3.a| Average pore radius of MscL during translocation of Poly(dA)$_{60}$, Poly(dC)$_{60}$, Poly(dG)$_{60}$ and Poly(dT)$_{60}$. **b|** Pore radius for 3 stable states of MscL (closed, intermediate and expanded) and its comparison with the pore radius for translocation of Poly(dA)$_{60}$.

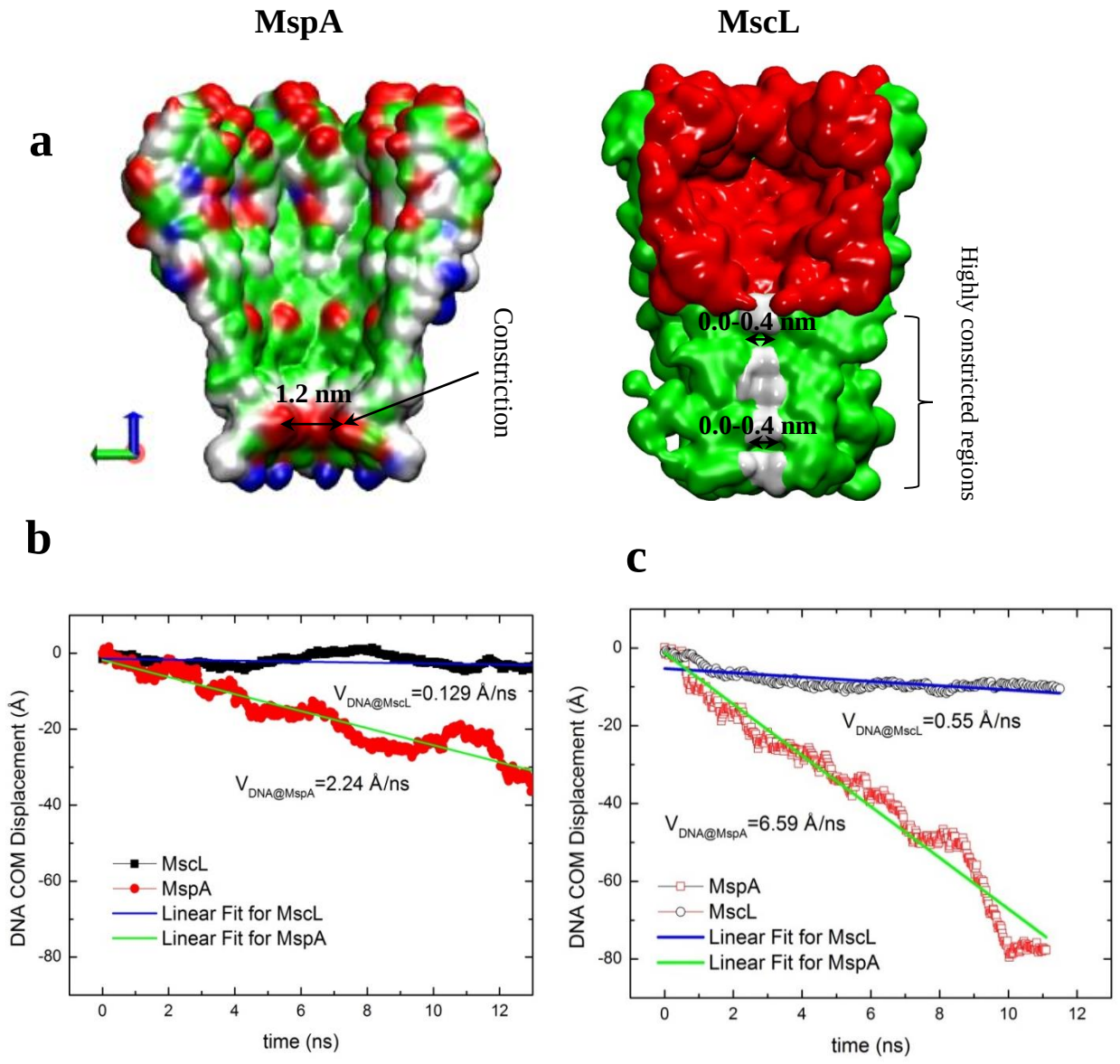

Figure 3.4.a| Cross-Sections of MspA and MscL pores and their structural differences. **b|** DNA center of mass (COM) translocation history through MspA and MscL for a bias=500 mV. **c|** DNA center of mass (COM) translocation history through MspA and MscL for a bias=1Volt.

3.6 References

1. Venkatesan, B. M.; Bashir, R. Nanopore Sensors for Nucleic Acid Analysis. *Nat. Nanotechnol.* 2011, 6, 615-624.
2. Branton, D.; Deamer, D. W.; Marziali, A.; Bayley, H.; Benner, S. A.; Butler, T.; Di Ventra, M.; Garaj, S.; Hibbs, A.; Huang, X. H.; Jovanovich, S. B.; Krstic, P. S.; Lindsay, S.; Ling, X. S. S.; Mastrangelo, C. H.; Meller, A.; Oliver, J. S.; Pershin, Y. V.; Ramsey, J. M.; Riehn, R.; Soni, G. V.; Tabard-Cossa, V.; Wanunu, M.; Wiggin, M.; Schloss, J. A. The Potential and Challenges of Nanopore Sequencing. *Nat. Biotechnol.* 2008, 26, 1146-1153.
3. Kasianowicz, J. J.; Brandin, E.; Branton, D.; Deamer, D. W. Characterization of Individual Polynucleotide Molecules Using a Membrane Channel. *Proc. Natl. Acad. Sci. U. S. A.* 1996, 93, 13770-13773.
4. Braha, O.; Walker, B.; Cheley, S.; Kasianowicz, J. J.; Song, L. Z.; Gouaux, J. E.; Bayley, H. Designed Protein Pores as Components for Biosensors. *Chem. Biol.* 1997, 4, 497-505.
5. Gu, L. Q.; Braha, O.; Conlan, S.; Cheley, S.; Bayley, H. Stochastic Sensing of Organic Analytes by a Pore-Forming Protein Containing a Molecular Adapter. *Nature* 1999, 398, 686-690.
6. Bayley, H.; Cremer, P. S. Stochastic Sensors Inspired by Biology. *Nature* 2001, 413, 226-230.
7. Clarke, J.; Wu, H. C.; Jayasinghe, L.; Patel, A.; Reid, S.; Bayley, H. Continuous Base Identification for Single-Molecule Nanopore DNA Sequencing. *Nat. Nanotechnol.* 2009, 4, 265-270.
8. Kircher, M.; Kelso, J. High-Throughput DNA Sequencing - Concepts and Limitations. *Bioessays* 2010, 32, 524-536.
9. Majd, S.; Yusko, E. C.; Billeh, Y. N.; Macrae, M. X.; Yang, J.; Mayer, M. Applications of Biological Pores in Nanomedicine, Sensing, and Nanoelectronics. *Curr. Opin. Biotechnol.* 2010, 21, 439-476.
10. Akeson, M.; Branton, D.; Kasianowicz, J. J.; Brandin, E.; Deamer, D. W. Microsecond Time-Scale Discrimination among Polycytidylic Acid, Polyadenylic Acid, and Polyuridylic Acid as Homopolymers or as Segments within Single Rna Molecules. *Biophys. J.* 1999, 77, 3227-3233.
11. Butler, T. Z.; Pavlenok, M.; Derrington, I. M.; Niederweis, M.; Gundlach, J. H. Single-Molecule DNA Detection with an Engineered Mspa Protein Nanopore. *Proc. Natl. Acad. Sci. U. S. A.* 2008, 105, 20647-20652.
12. Chang, G.; Spencer, R. H.; Lee, A. T.; Barclay, M. T.; Rees, D. C. Structure of the MscL Homolog from Mycobacterium Tuberculosis: A Gated Mechanosensitive Ion Channel. *Science* 1998, 282, 2220-2226.
13. Siwy, Z. S.; Davenport, M. Nanopores Graphene Opens up to DNA. *Nat. Nanotechnol.* 2010, 5, 697-698.
14. Wells, D. B.; Belkin, M.; Comer, J.; Aksimentiev, A. Assessing Graphene Nanopores for Sequencing DNA. *Nano Lett.* 2012, 12, 4117-4123.
15. Min, S. K.; Kim, W. Y.; Cho, Y.; Kim, K. S. Fast DNA Sequencing with a Graphene-Based Nanochannel Device. *Nat. Nanotechnol.* 2011, 6, 162-165.
16. Farimani, A. B.; Min, K.; Aluru, N. R. DNA Base Detection Using a Single-Layer MoS_2. *ACS Nano* 2014, 8, 7914-7922.
17. Liu, K.; Feng, J. D.; Kis, A.; Radenovic, A. Atomically Thin Molybdenum Disulfide Nanopores with High Sensitivity for DNA Trans Location. *ACS Nano* 2014, 8, 2504-2511.
18. Saha, K. K.; Drndic, M.; Nikolic, B. K. DNA Base-Specific Modulation of Microampere Transverse Edge Currents through a Metallic Graphene Nanoribbon with a Nanopore. *Nano Lett.* 2012, 12, 50-55.
19. Liu, Y. X.; Dong, X. C.; Chen, P. Biological and Chemical Sensors Based on Graphene Materials. *Chem. Soc. Rev.* 2012, 41, 2283-2307.

20. Prasongkit, J.; Grigoriev, A.; Pathak, B.; Ahuja, R.; Scheicher, R. H. Transverse Conductance of DNA Nucleotides in a Graphene Nanogap from First Principles. *Nano Lett.* 2011, 11, 1941-1945.
21. Sukharev, S.; Durell, S. R.; Guy, H. R. Structural Models of the MscL Gating Mechanism. *Biophys. J.* 2001, 81, 917-936.
22. Sukharev, S.; Betanzos, M.; Chiang, C. S.; Guy, H. R. The Gating Mechanism of the Large Mechanosensitive Channel MscL. *Nature* 2001, 409, 720-724.
23. Sukharev, S.; Anishkin, A. Mechanosensitive Channels: What Can We Learn from 'Simple' Model Systems? *Trends in Neurosciences* 2004, 27, 345-351.
24. Jeon, J.; Voth, G. A. Gating of the Mechanosensitive Channel Protein MscL: The Interplay of Membrane and Protein. *Biophys. J.* 2008, 94, 3497-3511.
25. Sukharev, S. I.; Blount, P.; Martinac, B.; Blattner, F. R.; Kung, C. A Large-Conductance Mechanosensitive Channel in E. Coli Encoded by MscL Alone. *Nature* 1994, 368, 265-268.
26. Perozo, E.; Cortes, D. M.; Sompornpisut, P.; Kloda, A.; Martinac, B. Open Channel Structure of Mscl and the Gating Mechanism of Mechanosensitive Channels. *Nature* 2002, 418, 942-948.
27. Gullingsrud, J.; Kosztin, D.; Schulten, K. Structural Determinants of Mscl Gating Studied by Molecular Dynamics Simulations. *Biophys. J.* 2001, 80, 2074-2081.
28. Gullingsrud, J.; Schulten, K. Gating of Mscl Studied by Steered Molecular Dynamics. *Biophys. J.* 2003, 85, 2087-2099.
29. Gullingsrud, J.; Schulten, K. Lipid Bilayer Pressure Profiles and Mechanosensitive Channel Gating. *Biophys. J.* 2004, 86, 3496-3509.
30. Barriga, H. M. G.; Booth, P.; Haylock, S.; Bazin, R.; Templer, R. H.; Ces, O. Droplet Interface Bilayer Reconstitution and Activity Measurement of the Mechanosensitive Channel of Large Conductance from Escherichia Coli. *J. R. Soc. Interface* 2014, 11.
31. Yang, L. M.; Wray, R.; Parker, J.; Wilson, D.; Duran, R. S.; Blount, P. Three Routes to Modulate the Pore Size of the MscL Channel/Nanovalve. *ACS Nano* 2012, 6, 1134-1141.
32. Kale, L.; Skeel, R.; Bhandarkar, M.; Brunner, R.; Gursoy, A.; Krawetz, N.; Phillips, J.; Shinozaki, A.; Varadarajan, K.; Schulten, K. Namd2: Greater Scalability for Parallel Molecular Dynamics. *J. Comput. Phys.* 1999, 151, 283-312.
33. Humphrey, W.; Dalke, A.; Schulten, K. Vmd: Visual Molecular Dynamics. *J. Mol. Graph.* 1996, 14, 33-38.
34. MacKerell, A. D.; Banavali, N. K. All-Atom Empirical Force Field for Nucleic Acids: Ii. Application to Molecular Dynamics Simulations of DNA and Rna in Solution. *J. Comput. Chem.* 2000, 21, 105-120.
35. Gosse, C.; Croquette, V. Magnetic Tweezers: Micromanipulation and Force Measurement at the Molecular Level. *Biophys. J.* 2002, 82, 3314-3329.
36. Monajemi, M.; Ketabi, S.; Zadeh, M. H.; Amiri, A. Simulation of DNA Bases in Water: Comparison of the Monte Carlo Algorithm with Molecular Mechanics Force Fields. *Biochem.-Moscow* 2006, 71, S1-S8.
37. Dekker, C. Solid-State Nanopores. *Nat. Nanotechnol.* 2007, 2, 209-215.
38. Deamer, D. W.; Branton, D. Characterization of Nucleic Acids by Nanopore Analysis. *Accounts Chem. Res.* 2002, 35, 817-825.
39. Derrington, I. M.; Butler, T. Z.; Collins, M. D.; Manrao, E.; Pavlenok, M.; Niederweis, M.; Gundlach, J. H. Nanopore DNA Sequencing with Mspa. *Proc. Natl. Acad. Sci. U. S. A.* 2010, 107, 16060-16065.
40. Faller, M.; Niederweis, M.; Schulz, G. E. The Structure of a Mycobacterial Outer-Membrane Channel. *Science* 2004, 303, 1189-1192.

CHAPTER 4: DNA Origami-Graphene Hybrid Nanopore for DNA Detection

4.1 Introduction

Biological and solid state nanopores offer great potential for DNA sequencing since they provide label-free, fast and single-molecule detection methods.[1, 2] In such devices, the ionic current modulated during DNA electrophoretic translocation reveals the nucleotide types.[3, 4] Noise in the electric current readout masks the detection signals, making detection erroneous and difficult.[5-7] To overcome these challenges, practical solutions such as using thin 2D material membranes,[8-10] slowing down DNA techniques,[11] flexible biological nanopores,[12] and pore functionalization were offered.[13-15] Among these solutions, bio-functionalization of inorganic nanopores seems to provide two advantages over chemically/synthetically modified pores. First, they can be programmed to yield specific interactions; consequently, ameliorate the noisy electric signals or even yield ancillary detection signals.[16, 17] Second, the bio-functionalization can be tuned and engineered with nanometer scale precision at the pore mouth. [18, 19]

DNA origami[20, 21] can be employed to functionalize the solid-state nanopores.[16, 22, 23] Programmable nanobox,[24 25, 26]plates,[16] channels in bilayer[23, 27] were constructed using DNA origami techniques. The self-assembly property and nanometer precision engineering of DNA origami nanostructures make them an attractive candidate for creating hybrid nanopores.[16, 22]

Using experimental techniques, DNA origami was inserted into silicon nitride nanopore and used for detection of λ-DNA.[16] In some other publications,[16, 22] DNA origami nano-plates were deposited on the surface of a pore and the generated hybrid nanopore was used for detection of proteins and single stranded DNA's (ssDNA's). The "bait-prey" mechanism[16] is used by taking advantage of DNA origami plates on a nanopore to create specific interactions with proteins.[16] The specific interaction between DNA-origami and protein-DNA binding sites gives rise to a distinguishable dwell time for proteins, facilitating single molecule studies and protein recognition.[28]

Using molecular dynamics simulations, the stability and structural properties of DNA origami shapes have already been well explored and investigated.[29] Recently, the dependence of the conductivity on the number of DNA layers, with different applied biases was characterized.[30] Also the packing of origami plates with the presence of Mg^{2+} ions was explored.[30]

With the advances in current fabrication technologies, deposition and programming of DNA origami plates on top of substrates[31, 32], chemically modified graphene[33] and MoS_2 [34]are feasible. It's been demonstrated that the DNA origami can be placed on top of graphene with 1-2nm precision adjustment.[33] Considering these advances, and the benefits that DNA origami offers to nanopore functionalization,[35] we decided to study a hybrid nanopore consisting of graphene and DNA origami nano-plate. It's notable that up to now, the molecular scale interaction between DNA origami and translocating DNA is largely unknown. Also the stability and the structure of DNA origami at the pore edge during DNA translocation needed to be investigated in detail. In this work, the graphene nanopore is specifically functionalized by dangling T bases which are part of DNA origami plate. In other words, we created a DNA origami nanopore with unpaired T bases at the edge and placed it on top of a graphene nanopore. The hybrid nanopores with zero, one and two

layers of DNA origami were characterized and used for the detection of DNA bases. The interactions between hybrid nanopore and sequencing DNA, the dwell time of each base type and the stability of hybrid nanopores were investigated and discussed.

4.2 Methods

We performed all-atom molecular dynamics (MD) simulations with NAMD 2.6 using the peta-scale Blue Waters machine.[36] Visual Molecular Dynamics (VMD)[37] is used for the visualization of a typical simulation set up consisting of the DNA origami nanoplate, graphene nanopore, ssDNA, water and ions (~118,000-120,000 atoms, as shown in Figure 4.1.a). A pore with diameter of 2.1 nm is drilled in the center of a 10 nm × 10 nm single layer graphene (Figure 4.1.b). In all simulations, the carbon atoms of the graphene sheet inside a ring with radius 1.6 nm around the pore have been restrained by a harmonic potential (with spring constant of k=5 kcal/(mol $Å^2$)) and the remaining atoms of the graphene sheet were fixed.

The model of one layer 8.7 nm×9.3 nm square lattice DNA origami nano-plate has been designed and generated using caDNAno software.[38] Using caDNAno,[38] the sequence of the bases was properly assigned to place a number of A-T pair bases in the middle of the plate. The DNA origami nano-plate is then placed on top of a nano-porous graphene. At the location of the graphene pore, the structure of DNA origami was modified to create an aperture in origami nanoplate by deleting eight A bases of staple strands and leaving eight unpaired T bases in the scaffold strand (see APPENDIX C) (Figure 4.1.c).

To perform simulations of the translocation of different nucleotide types, four different systems were constructed for polyDA, PolyDC, PolyDG and polyDT that each ssDNA consists of 20 bases and is combined with DNA origami-graphene hybrid nanopore. In each case, three first bases of

ssDNA were located inside the hybrid nanopore. Then, the whole structure was solvated in an aqueous 1.0 M NaCl solution.

Water molecules were treated as rigid using SHAKE algorithm.[39] We used the CHARMM27 force field[40] parameters for nucleic acids, TIP3P water molecules, graphene and ions. Periodic boundary condition is applied in all the three directions. The cut off distance for LJ and short range electrostatic interactions is 12.5 Å. The long-range electrostatic interactions were computed by using the Particle-Mesh-Ewald (PME) method.[41] The integration time step is selected to be 1 fs.

Before equilibration, energy minimization was performed for each system for 25000 steps. Upon minimization, equilibration was performed for 5 ns with harmonically restrained nucleic acids (of both DNA origami and ssDNA with k_{spring} = 100 kcal/(mol Å^2)). Following that, we maintained the ssDNA with harmonic constraint (with k_{spring} = 1 kcal/(mol Å^2)) and performed equilibration for 2 ns while the DNA origami nanoplate was free to move with no constraint. Next, another equilibration simulation was performed for 1ns with no constraint on nucleic acids. Previously mentioned equilibrations were done under NPT ensemble, while pressure was kept constant at 1atm using Nosé-Hoover Langevin piston method[42, 43] and temperature was maintained at constant value of 300 K by Langevin thermostat.[44] Before applying an external electric field, the final equilibration step was performed for 2ns with NVT ensemble.

All ionic current simulations were performed under NVT ensemble at 300 K. An electric field was applied along the z direction (ssDNA axis). During all ionic current simulations, DNA origami nanoplate was completely free to move. The external electric fields are reported in terms of a transmembrane voltage difference $V = -EL_z$, where E is the electric field strength and L_z is the length of the simulation system along the z direction.[45] We monitored the time-dependent ionic

current, *I(t)*, in the pore. We computed the ionic current through the nanopore by using the definition of current, $I=dq/dt$, as $I(t)=\frac{1}{L_z}\sum_{i=1}^{n} q_i\left[\frac{z_i(t+\delta t)-z_i(t)}{\delta t}\right]$, where the sum is over all the ions, δt is chosen to be 4 ps, z_i and q_i are the z-coordinate and the charge of ion *i* respectively, and *n* is the total number of ions. The ionic current data was block averaged over intervals of 100 ps.[45]

4.3 Results and Discussion

Presence of T base type at the mouth of the pore induces specific interactions with the translocating DNA, especially its complementary base, i.e., base A. Hypothetically, these interactions will give rise to specific signatures for DNA detection that we are trying to explore in this dissertation.

To characterize the graphene nanopore coated with DNA origami and the bare graphene nanopore, we computed the ionic current associated for these pores versus different biases (these systems do not contain translocating ssDNA). Since DNA origami is negatively charged, we did not study the negative branch of I-V curve because DNA origami will fly away from graphene surface. Applying negative biases causes the detachment of DNA origami from the surface of graphene sheet. For each bias point in Figure 4.2.a, we performed a simulation with the duration of 40 ns and we averaged the instantaneous ionic currents. In the case of 1 layer DNA origami we just accounted for the current through the middle pore of the nano-plate and not for the gaps and free spaces between DNA strands. The average ionic currents order for a same amount of bias is 2 layer DNA origami- graphene < 1 layer DNA origami-graphene < 1 layer DNA origami < bare (pristine) graphene nanopore (Figure 4.2.a). At bias of 0.25 V, the currents for 2 layer DNA origami-graphene, 1 layer DNA origami-graphene,1 layer DNA origami, and bare (pristine) graphene nanopore are 0.104 nA, 0.52 nA, 1.26 nA and 1.5 nA, respectively (Figure 4.2.a). The characteristic plots for all pores are fitted well into linear plots. The resistance of the bare graphene

pore is 0.285 V/nA and for the hybrid pore (1 layer DNA origami-graphene) is 0.667 V/nA. Since the origami nanoplate and the graphene nanopore are connected in series, the resistance of the origami plate is yielded to be 0.382 V/nA (APPENDIX C). The resistances of the hybrid nanopores are higher than the graphene nanopore, which can be attributed to their higher thickness and polarization. [22, 35]

We computed the conductance of different nanopores (pristine graphene, pristine DNA origami nanopore, 1 layer DNA origami-graphene and 2layer DNA origami-graphene (Figure 4.2.b-black)). Simply, the conductance is defined as $G=I/V$. The highest and lowest conductance is associated with the pristine graphene and 2 layer DNA origami-graphene, respectively. The order of the conductance in these pores is changing as pristine graphene> 1 layer DNA origami> 1 layer DNA origami-graphene>2layer DNA origami-graphene. As the conduction (G) highly correlates with the thickness of the membrane, Kowalczyk et al. proposed the following mathematical equation for the conductance [46]

$$G = \kappa\left[\frac{4l_{pore}}{\pi d^2} + \frac{1}{d}\right]^{-1}$$

where κ is the conductivity of the solution, l_{pore} is the effective thickness of the nanopore, and d is its diameter. Conductivity of the buffer κ is calculated by performing ionic current simulations for a 1M NaCl solution cell (see APPENDIX C). Kowalczyk et al.[46] assert that this model is accurate enough to predict the conductance of nanopores with the thickness of ~8.5 nm, while it overestimates the conductance of thinner membranes. We evaluated and compared the values of equation 1 to our results obtained from MD simulations (Figure 4.2.b-red). The higher values of equation 1 in comparison with the simulations results can be explained by small thicknesses of our

nanopores. The pore thickness of pristine graphene, 1 layer DNA origami, 1 layer DNA origami-graphene, 2layer DNA origami-graphene are 0.34 nm, 2.6 nm, 2.94 nm, and 5.44 nm, respectively. (we measured the minimum and maximum of the sheets' coordinates in z direction and averaged it over the simulation time).

To study and compare the translocation speed of ssDNA in hybrid nanopores and pristine graphene, we simulated poly$(dA)_{20}$ in pristine graphene (Figure 4.3.a), 4 poly-ssDNA's with 20 bases (A, C, G, T base types) in hybrid DNA origami-graphene (Figure 4.3.b), , and poly$(dA)_{30}$ in hybrid double–layer DNA origami-graphene nanopores (Figure 4.3.c). All these simulations were performed at 1.85 V bias. The fastest electrophoretic translocation is happened for pristine graphene nanopore where 20 DNA bases (type A) passed through the pore in 5 ns (Figure 4.3.d). The lowest translocation occurs for poly$(dA)_{30}$ through double-layer DNA origami – graphene nanopore that only 5 bases were translocated in 26 ns (Figure 3d). For the single layer DNA origami-graphene nanopore, which is the main case of our study, the order of translocation rates follows as A<T<C<G (Figure 4.3.d). For Poly$(dA)_{20}$, only 15 bases were successfully translocated and 5 last bases were stuck in the pore for more than 30ns. We also monitored and averaged the residence time of bases at the pore mouth and found that A bases resides in the DNA origami-graphene hybrid nanopore nine times longer than the pristine graphene nanopore. Furthermore, A bases dwell at the pore two times longer than that of T, three times than that of C and six times than that of G (Figure 4.3.e). While the residence time of different base types is nearly the same for graphene nanopore, it is significantly dependent on the translocating base type for the hybrid nanopore. This feature of the hybrid nanopore implies that the distinguishable dwell time of bases can be used as ancillary detection signal.

To shed more lights on the interactions between the hybrid pore and the strand of the translocating DNA, we computed the average hydrogen bonds (HB) between ssDNA and DNA origami at the pore. The snapshots of HBs which are made during translocation are shown in Figure 4.4.a and 4.4.b. To compute the number of hydrogen bonds, we considered the electrostatic interactions between (H, C, N, and O). The order of number of HBs created during translocation is A>C=G>T (Figure 4.4.c). The A (translocating base type) – T (unpaired bases of the pore) base paring gives rise to highest correlation and makes the highest number of HBs. However, for translocation of poly(dT), we observed the lowest number of HBs because of mismatching between ssDNA T bases and unpaired T bases of the pore. (Figure 4.4.c)

To see the changes in the interaction energies during translocation of ssDNA in the presence of DNA origami nanopore, we computed the interaction energies between the atoms of the translocating poly(dA) and the DNA origami nanoplate (Figure 4.4.d). There is a high correlation between the interaction energies and the stepwise translocation history (Figure 4.4.d). For example, some bases were stuck in time windows of 7-10 ns and 14-16 ns (long-lasting flat steps are the signatures of bases being stuck, Figure 4.4.d), and at the same time instances, we observed a peak (local maxima) in the interaction energies (190 Kcal/mol and 210 Kcal/mol, respectively). In other words, at time instances when the DNA origami and the translocating DNA are engaged and fully interact with each other, the electrophoretic forces could not overcome the friction between the DNA origami and the translocating DNA, which gives rise to higher residence time/dwell time. At the time instances where successive translocation occurs, the average interaction energies are lower and around 110 Kcal/mol.

In order to explore the ionic current characteristic of the hybrid pore, we averaged the ionic current associated with the translocation of each poly-ssDNA type (Figure 4.5.a). The order of the

averaged ionic current is A>C>T>G. Figure 4.5.b illustrates the schematic of the system being used for ionic current simulations. This figure shows how the dangling T bases of the pore are in contact with the translocating bases of ssDNA's.

In order to see the stability and arrangement of the dangling bases around the pore, we monitored the number of bases which reside around the pore for the translocation of poly(dA)$_{20}$ (see APPENDIX C for the detail analysis of DNA origami density in the vicinity of the pore). The geometrical space that we examined the bases within is an infinitely long cylinder concentric with the pore center and with the radius of 22.4 Å. The most prevailed base type around the pore is T which resides around the pore in a stable manner (Figure 4.5.c). The other base types (i.e A, C, G) occupy the pore vicinity approximately one third of the base type T which implies that the initial functionalized pore with base type T is stable even with the presence of thermal noise, water and ions permeation and DNA electrophoretic translocation (Figure 4.5.c).

In order to investigate the status of pore functionalization during the translocation of the other base types, we averaged the number of bases residing in the geometrical space (we explained above) in all simulations over the whole period of DNA translocation (Figure 4.5.d). 10-13 T bases occupy the pore mouth and only 4-6 bases of A, C and G types stay at the pore. Interestingly, bases of poly(dA) and poly(dC) attract the T bases type of DNA origami nanoplate more than poly(dG) and poly(dT) do (Figure 4.5.d-green line). For translocating nucleotide A, higher number of hydrogen bonds combined with the high density occupation of complimentary T bases around the pore creates specific interactions which yield to a higher dwelling time for base type A.

Due to the challenges posed by amplifier bandwidth limitations, the higher residence time of the single base at the pore would be beneficial for read out. Longer residence time and slower speed

of DNA translocation will insure higher resolution signal acquisition. In nanopores, usually the speed of translocation is so fast even at the low biases around 100 mV that the MHz bandwidth of the current amplifiers may not be able to resolve the single base readouts. Among the solutions that were proposed for speed reduction, we can name the usage of high viscosity buffer solution, lower temperature, flexible MscL nanopore and pore functionalization.[12] Presence of DNA origami on top of graphene nanopore not only creates additional signature for recognition, but reduces the speed of translocation. To quantify and compare the speed of translocation of polyDA in hybrid and bare graphene nanopores, we performed simulations up to 70 ns at different biases. At biases between 2-4 V, the translocation time for hybrid pore is 4-6 times slower than bare graphene pore (Figure 4.6).

4.4 Conclusion

We demonstrated that the hybrid pore of DNA origami-graphene can yield distinguishable dwell time for DNA bases. Four different nanopores i.e. bare graphene, 1 layer DNA origami, 1 layer DNA origami -graphene, and 2layer DNA origami-graphene were characterized in terms of ionic current, conductance and resistance. The pore conductance highly correlates with the thickness of the pore. The initial functionalization of graphene pore with base T remains intact during electrophoretic translocation of DNA bases. The combination of distinguishable dwell time and ionic current along the slower speed of translocation make hybrid origami-graphene pore amenable for better DNA detection. The hydrogen bonds between translocating DNA and DNA origami at the pore are the origin of distinguishable dwell time.

4.5 Figures

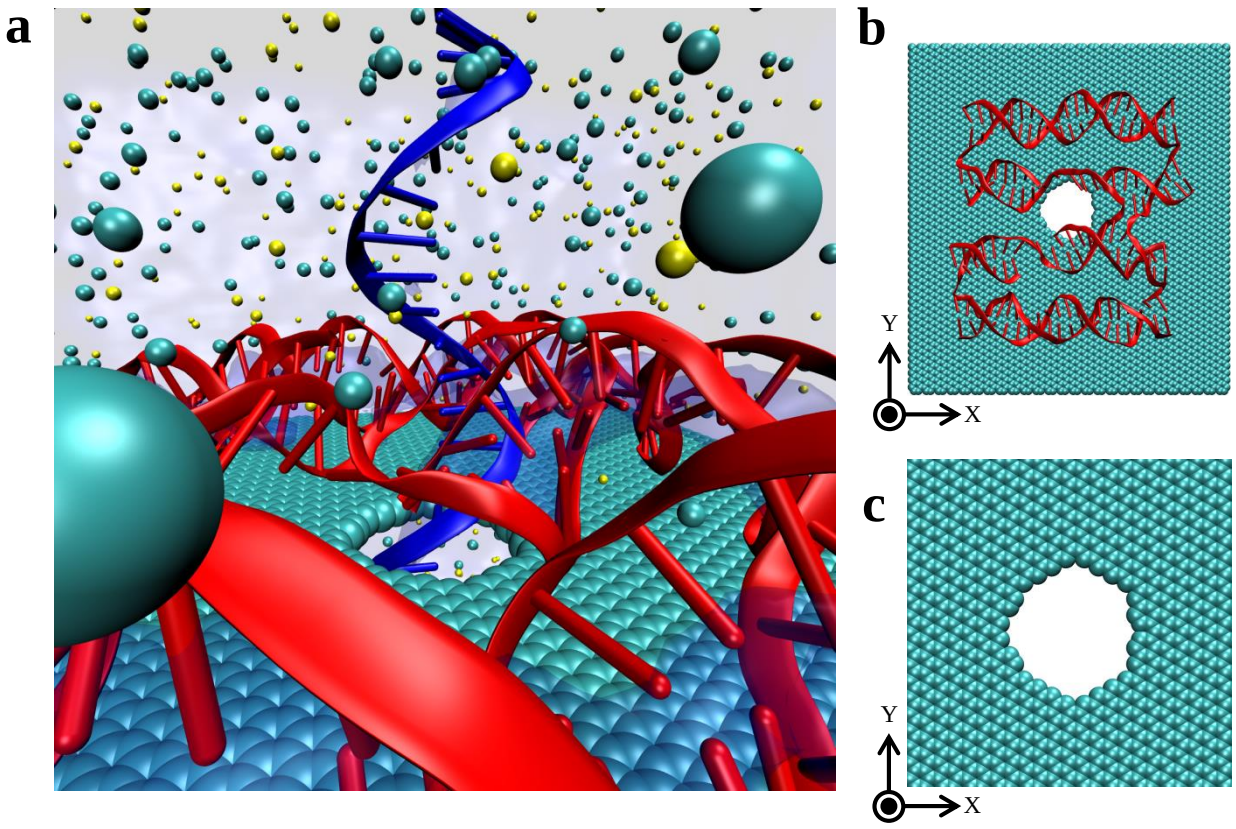

Figure 4.1. a| Simulation box consisting of single layer DNA origami (depicted in red), graphene sheet, water, ions, and translocating DNA (depicted in blue). **b|** Single layer DNA origami on top of graphene. **c|** Pristine (bare) graphene nanopore.

a

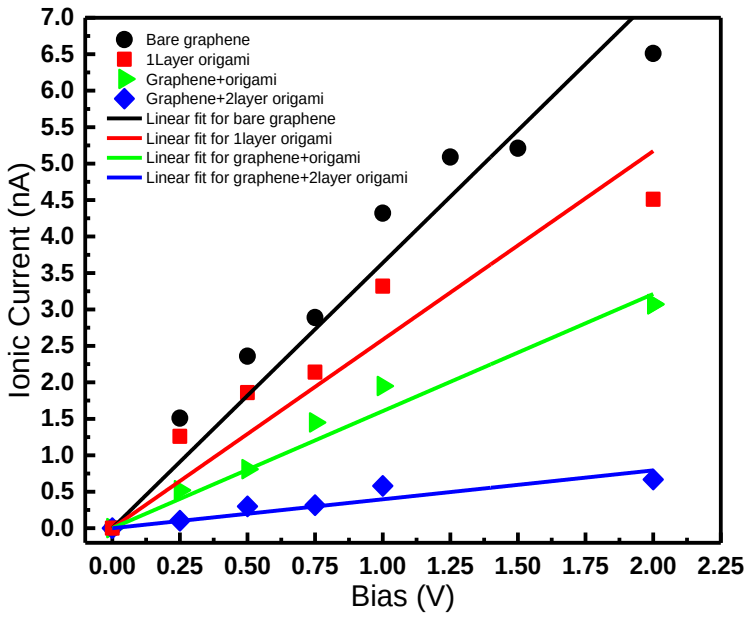

b

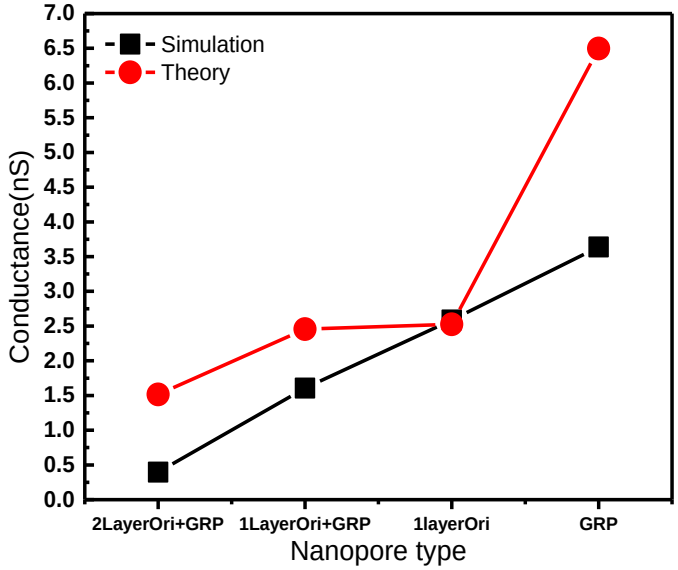

Figure 4.2.a| *I-V* curves for four types of nanopores. **b|** Conductance of different pores and their comparison with theoretical predictions.

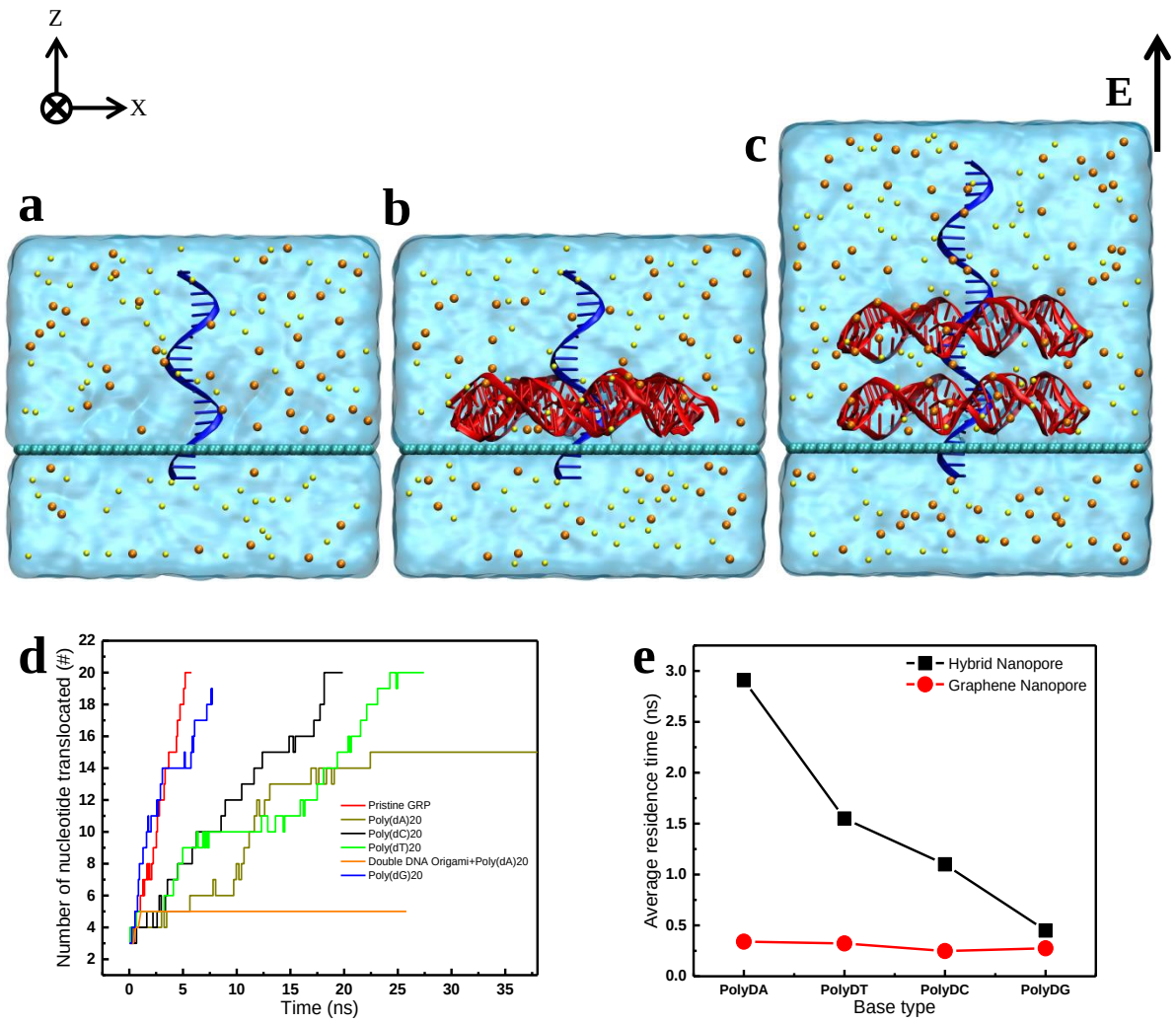

Figure 4.3. a| Simulation system of DNA sequencing through bare graphene nanopore. The all atom model contains graphene nanopore, ssDNA (depicted in blue), water and ions. **b|** Simulation system of DNA sequencing through single layer DNA origami-graphene hybrid nanopore. The all atom model contains single layer DNA origami (depicted in red), graphene nanopore, ssDNA (depicted in blue), water and ions. **c|** Simulation system of DNA sequencing through double layers DNA origami-graphene hybrid nanopore. The all atom model contains double layers DNA origami (depicted in red), graphene nanopore, ssDNA (depicted in blue), water and ions. **d|** Translocation history of ssDNA's in different pores. **e|** Average residence time of different base types in hybrid and bare graphene nanopores.

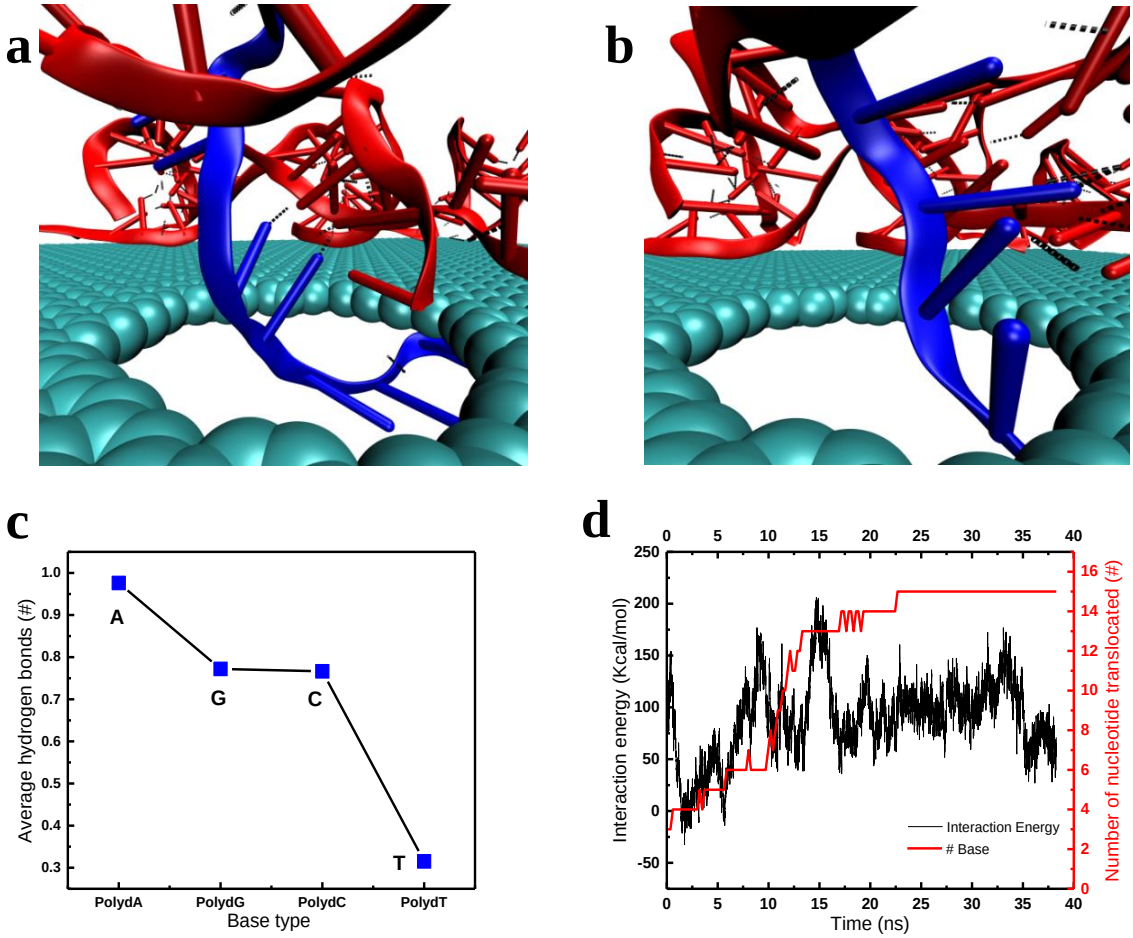

Figure 4.4. a| Snapshot of hydrogen bonds between poly(dA) and DNA origami (the black dash lines represent HBs) **b|** Snapshot of hydrogen bonds between poly(dT) and DNA origami (the black dash lines represent HBs) **c|** Average number of HBs between ssDNA's and DNA origami nanoplate. **d|** Time dependent interaction energies between poly(dA) and DNA origami nanoplate (black). Translocation plot of poly(dA) through hybrid nanopore (red).

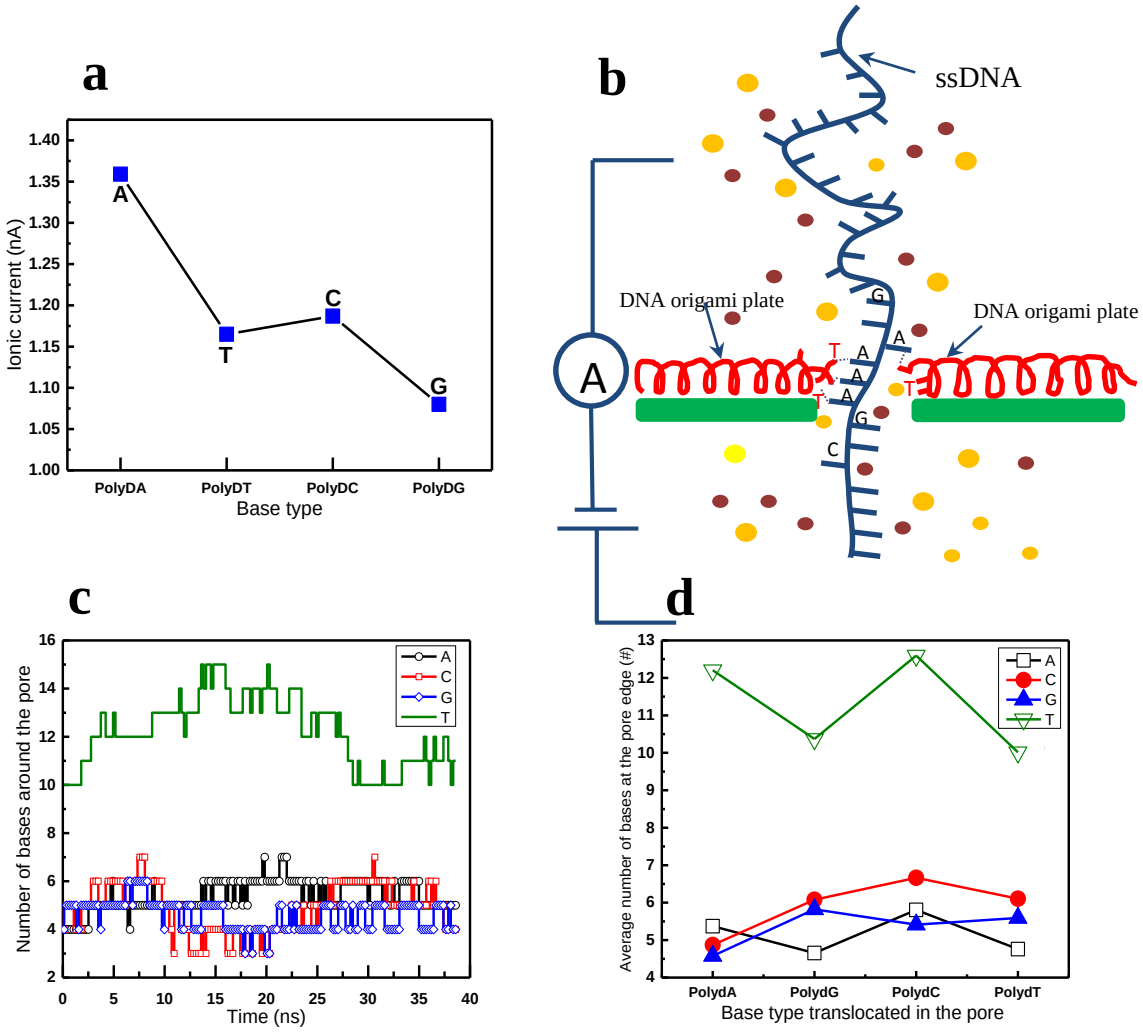

Figure 4.5. a| Ionic currents for different base types computed for the translocation of poly-ssDNA's through the single layer DNA origami-graphene hybrid nanopore .**b|** Schematic of the ionic current simulations system showing the complimentary bases (A-T) interacting. **c|** Density of different base types of DNA origami nanoplate in the vicinity of the pore versus simulation time for poly(dA) **d|** Average density of different base types of DNA origami nanoplate in the vicinity of the pore during poly-ssDNA's translocations.

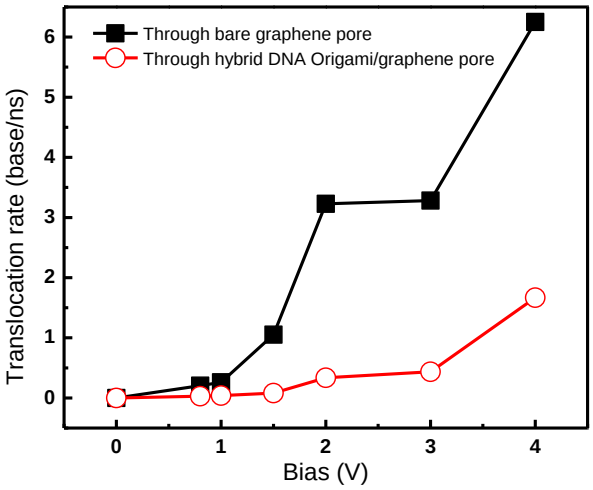

Figure 4.6. Comparison of polyDA translocation rate through single layer DNA origami-graphene hybrid nanopore and bare graphene nanopore.

4.6 References

1. Venkatesan, B. M.; Bashir, R. Nanopore Sensors for Nucleic Acid Analysis. *Nat. Nanotechnol.* 2011, 6, 615-624.
2. Keyser, U. F. Controlling Molecular Transport through Nanopores. *J. R. Soc. Interface* 2011, 8, 1369-1378.
3. Kasianowicz, J. J.; Brandin, E.; Branton, D.; Deamer, D. W. Characterization of Individual Polynucleotide Molecules Using a Membrane Channel. *Proc. Natl. Acad. Sci. U. S. A.* 1996, 93, 13770-13773.
4. Bayley, H.; Cremer, P. S. Stochastic Sensors Inspired by Biology. *Nature* 2001, 413, 226-230.
5. Deamer, D. W.; Branton, D. Characterization of Nucleic Acids by Nanopore Analysis. *Accounts Chem. Res.* 2002, 35, 817-825.
6. Dekker, C. Solid-State Nanopores. *Nat. Nanotechnol.* 2007, 2, 209-215.
7. Branton, D.; Deamer, D. W.; Marziali, A.; Bayley, H.; Benner, S. A.; Butler, T.; Di Ventra, M.; Garaj, S.; Hibbs, A.; Huang, X. H.; Jovanovich, S. B.; Krstic, P. S.; Lindsay, S.; Ling, X. S. S.; Mastrangelo, C. H.; Meller, A.; Oliver, J. S.; Pershin, Y. V.; Ramsey, J. M.; Riehn, R.; Soni, G. V.; Tabard-Cossa, V.; Wanunu, M.; Wiggin, M.; Schloss, J. A. The Potential and Challenges of Nanopore Sequencing. *Nat. Biotechnol.* 2008, 26, 1146-1153.
8. Farimani, A. B.; Min, K.; Aluru, N. R. DNA Base Detection Using a Single-Layer MoS_2. *ACS Nano* 2014, 8, 7914-22.
9. Liu, K.; Feng, J. D.; Kis, A.; Radenovic, A. Atomically Thin Molybdenum Disulfide Nanopores with High Sensitivity for DNA Trans Location. *ACS Nano* 2014, 8, 2504-2511.
10. Schneider, G. F.; Kowalczyk, S. W.; Calado, V. E.; Pandraud, G.; Zandbergen, H. W.; Vandersypen, L. M. K.; Dekker, C. DNA Translocation through Graphene Nanopores. *Nano Lett.* 2010, 10, 3163-3167.
11. Rosenstein, J. K.; Wanunu, M.; Merchant, C. A.; Drndic, M.; Shepard, K. L. Integrated Nanopore Sensing Platform with Sub-Microsecond Temporal Resolution. *Nat. Methods* 2012, 9, 487-U112.
12. Farimani, A. B.; Heiranian, M.; Aluru, N. R. Electromechanical Signatures for DNA Sequencing through a Mechanosensitive Nanopore. *J. Phys. Chem. Lett.* 2015, 6, 650-657.
13. Luan, B. Q.; Stolovitzky, G.; Martyna, G. Slowing and Controlling the Translocation of DNA in a Solid-State Nanopore. *Nanoscale* 2012, 4, 1068-1077.
14. Butler, T. Z.; Pavlenok, M.; Derrington, I. M.; Niederweis, M.; Gundlach, J. H. Single-Molecule DNA Detection with an Engineered Mspa Protein Nanopore. *Proc. Natl. Acad. Sci. U. S. A.* 2008, 105, 20647-20652.
15. Sint, K.; Wang, B.; Kral, P. Selective Ion Passage through Functionalized Graphene Nanopores. *J. Am. Chem. Soc.* 2008, 130, 16448.
16. Wei, R. S.; Martin, T. G.; Rant, U.; Dietz, H. DNA Origami Gatekeepers for Solid-State Nanopores. *Angew. Chem.-Int. Edit.* 2012, 51, 4864-4867.
17. Yusko, E. C.; Johnson, J. M.; Majd, S.; Prangkio, P.; Rollings, R. C.; Li, J. L.; Yang, J.; Mayer, M. Controlling Protein Translocation through Nanopores with Bio-Inspired Fluid Walls. *Nat. Nanotechnol.* 2011, 6, 253-260.
18. Martin, C. R.; Siwy, Z. S. Learning Nature's Way: Biosensing with Synthetic Nanopores. *Science* 2007, 317, 331-332.
19. Iqbal, S. M.; Akin, D.; Bashir, R. Solid-State Nanopore Channels with DNA Selectivity. *Nat. Nanotechnol.* 2007, 2, 243-248.
20. Rothemund, P. W. K. Folding DNA to Create Nanoscale Shapes and Patterns. *Nature* 2006, 440, 297-302.
21. Sobczak, J. P. J.; Martin, T. G.; Gerling, T.; Dietz, H. Rapid Folding of DNA into Nanoscale Shapes at Constant Temperature. *Science* 2012, 338, 1458-1461.

22. Hernandez-Ainsa, S.; Bell, N. A. W.; Thacker, V. V.; Gopfrich, K.; Misiunas, K.; Fuentes-Perez, M. E.; Moreno-Herrero, F.; Keyser, U. F. DNA Origami Nanopores for Controlling DNA Translocation. *ACS Nano* 2013, 7, 6024-6030.
23. Seifert, A.; Gopfrich, K.; Burns, J. R.; Fertig, N.; Keyser, U. F.; Howorka, S. Bilayer-Spanning DNA Nanopores with Voltage-Switching between Open and Closed State. *ACS Nano* 2015, 9, 1117-1126.
24. Andersen, E. S.; Dong, M.; Nielsen, M. M.; Jahn, K.; Subramani, R.; Mamdouh, W.; Golas, M. M.; Sander, B.; Stark, H.; Oliveira, C. L. P.; Pedersen, J. S.; Birkedal, V.; Besenbacher, F.; Gothelf, K. V.; Kjems, J. Self-Assembly of a Nanoscale DNA Box with a Controllable Lid. *Nature* 2009, 459, 73-U75.
25. Han, D. R.; Pal, S.; Nangreave, J.; Deng, Z. T.; Liu, Y.; Yan, H. DNA Origami with Complex Curvatures in Three-Dimensional Space. *Science* 2011, 332, 342-346.
26. Gu, H. Z.; Chao, J.; Xiao, S. J.; Seeman, N. C. A Proximity-Based Programmable DNA Nanoscale Assembly Line. *Nature* 2010, 465, 202-U86.
27. Langecker, M.; Arnaut, V.; Martin, T. G.; List, J.; Renner, S.; Mayer, M.; Dietz, H.; Simmel, F. C. Synthetic Lipid Membrane Channels Formed by Designed DNA Nanostructures. *Science* 2012, 338, 932-936.
28. Wei, R. S.; Gatterdam, V.; Wieneke, R.; Tampe, R.; Rant, U. Stochastic Sensing of Proteins with Receptor-Modified Solid-State Nanopores. *Nat. Nanotechnol.* 2012, 7, 257-263.
29. Yoo, J.; Aksimentiev, A. In Situ Structure and Dynamics of DNA Origami Determined through Molecular Dynamics Simulations. *Proc. Natl. Acad. Sci. U. S. A.* 2013, 110, 20099-20104.
30. Li, C. Y.; Hemmig, E. A.; Kong, J. L.; Yoo, J.; Hernandez-Ainsa, S.; Keyser, U. F.; Aksimentiev, A. Ionic Conductivity, Structural Deformation, and Programmable Anisotropy of DNA Origami in Electric Field. *ACS Nano* 2015, 9, 1420-1433.
31. Gu, H. Z.; Chao, J.; Xiao, S. J.; Seeman, N. C. Dynamic Patterning Programmed by DNA Tiles Captured on a DNA Origami Substrate. *Nat. Nanotechnol.* 2009, 4, 245-248.
32. Teshome, B.; Facsko, S.; Keller, A. Topography-Controlled Alignment of DNA Origami Nanotubes on Nanopatterned Surfaces. *Nanoscale* 2014, 6, 1790-1796.
33. Yun, J. M.; Kim, K. N.; Kim, J. Y.; Shin, D. O.; Lee, W. J.; Lee, S. H.; Lieberman, M.; Kim, S. O. DNA Origami Nanopatterning on Chemically Modified Graphene. *Angew. Chem.-Int. Edit.* 2012, 51, 912-915.
34. Zhang, X. N.; Rahman, M.; Neff, D.; Norton, M. L. DNA Origami Deposition on Native and Passivated Molybdenum Disulfide Substrates. *Beilstein J. Nanotechnol.* 2014, 5, 501-506.
35. Bell, N. A. W.; Keyser, U. F. Nanopores Formed by DNA Origami: A Review. *FEBS Lett.* 2014, 588, 3564-3570.
36. Kale, L.; Skeel, R.; Bhandarkar, M.; Brunner, R.; Gursoy, A.; Krawetz, N.; Phillips, J.; Shinozaki, A.; Varadarajan, K.; Schulten, K. NAMD2: Greater Scalability for Parallel Molecular Dynamics. *J. Comput. Phys.* 1999, 151, 283-312.
37. Humphrey, W.; Dalke, A.; Schulten, K. VMD: Visual Molecular Dynamics. *J. Mol. Graph.* 1996, 14, 33-38.
38. Douglas, S. M.; Marblestone, A. H.; Teerapittayanon, S.; Vazquez, A.; Church, G. M.; Shih, W. M. Rapid Prototyping of 3d DNA-Origami Shapes with Cadnano. *Nucleic Acids Res.* 2009, 37, 5001-5006.
39. Ryckaert, J. P.; Ciccotti, G.; Berendsen, H. J. C. Numerical-Integration of Cartesian Equations of Motion of a System with Constraints - Molecular-Dynamics of N-Alkanes. *J. Comput. Phys.* 1977, 23, 327-341.
40. MacKerell, A. D.; Banavali, N. K. All-Atom Empirical Force Field for Nucleic Acids: Ii. Application to Molecular Dynamics Simulations of DNA and Rna in Solution. *J. Comput. Chem.* 2000, 21, 105-120.
41. Darden, T.; York, D.; Pedersen, L. Particle Mesh Ewald - an N. Log(N) Method for Ewald Sums in Large Systems. *J. Chem. Phys.* 1993, 98, 10089-10092.

42. Nose, S. A Unified Formulation of the Constant Temperature Molecular-Dynamics Methods. *J. Chem. Phys.* 1984, 81, 511-519.
43. Hoover, W. G. Canonical Dynamics - Equilibrium Phase-Space Distributions. *Phys. Rev. A* 1985, 31, 1695-1697.
44. Brunger, A. T.; Adams, P. D.; Clore, G. M.; DeLano, W. L.; Gros, P.; Grosse-Kunstleve, R. W.; Jiang, J. S.; Kuszewski, J.; Nilges, M.; Pannu, N. S.; Read, R. J.; Rice, L. M.; Simonson, T.; Warren, G. L. Crystallography & Nmr System: A New Software Suite for Macromolecular Structure Determination. *Acta Crystallogr. Sect. D-Biol. Crystallogr.* 1998, 54, 905-921.
45. Wells, D. B.; Belkin, M.; Comer, J.; Aksimentiev, A. Assessing Graphene Nanopores for Sequencing DNA. *Nano Lett.* 2012, 12, 4117-4123.
46. Kowalczyk, S. W.; Grosberg, A. Y.; Rabin, Y.; Dekker, C. Modeling the Conductance and DNA Blockade of Solid-State Nanopores. *Nanotechnology* 2011, 22.

CHAPTER 5: **Protein Recognition Using Graphene Nanopore**

5.1 Introduction

In spite of significant advances in the detection, separation and counting of single proteins with solid-state nanopores[1-5], atomically-resolved scanning of protein structure remains a significant challenge. In most nanopore-based DNA sequencing[6-10] and single molecule detection techniques[11], ionic current blockade and blockade duration are the primary signatures associated with reading and scanning.[6, 12, 13] Although these techniques are good enough for single molecule detection, they are not sophisticated enough to analyze and detect fine structures, homologues and mutagenesis.[11] For example, many subtle differences in antibody proteins, specifically in Immunoglobin Gamma (IgG) subclasses, lie in the number of amino acid compositions and disulfide bonds in their hinge region. Reading and discriminating between these minute structural differences requires a high resolution, single-atom thick and functionalizable nanopores. Biological nanopores[14, 15] are too small (~2 nm diameter pore) to study large molecules such as natively folded proteins and antibodies.[10, 16, 17] To-date, all fabricated solid-state nanopores are thick (e.g. Si_3N_4 functionalized pore has a thickness of 5-10 nm) that they completely envelope the whole protein.[2] As a result, the ionic current read by the nanopore sensor represents the single protein as a whole.[3, 12] The thickness of these membranes highly limits the potential to scan the spatial biological degeneracies and structure of the proteins at the single atom level.[10, 11, 17, 18]

Graphene is a robust, single-atom-thick lattice of carbon atoms with high electrical conductivity[19] and mechanical strength. The attractive properties of graphene can be exploited for high resolution, nanopore-based sequencing of single DNA molecules.[10, 20-23] The small thickness (0.34 nm) of the graphene membrane combined with the chemical inertness[20] provides a good spatial resolution/reading of the nucleic acid.[22, 24, 25] Graphene nanopore can also be easily configured[23, 26], resized[27, 28] and anchored with biological markers.[29] The single-atom thick graphene nanopore can read the DNA bases at atomic scale by taking advantage of the ionic current blockade.[30] Prior research has shown that graphene can also be used to detect DNA bases in the transverse direction by using quantum tunneling currents.[31] Quantum conductance tunneling in the transverse direction of graphene can detect the bases with a good resolution. [32-34]

In this study, we investigate graphene nanopore for scanning and detection of protein structures. Specifically, we focus on the detection of IgG subclasses. Detection, counting and distinguishing IgG subclasses is of utmost importance in immuno-competitive processes and immunology.[35] In fact, statistics of IgG subclasses in human serum are important towards mapping the immune system of the body and the attributed diseases. Perhaps, as a general concept, the proteome is a better molecular signature of the health status of humans than the genome; however, proteomic data are much more difficult to acquire and analyze.[32]

Two well-known issues of graphene nanopores in single molecule detection are the high speed of translocation and the noise.[23, 28] In this work, to overcome these issues, graphene nanopore is anchored with protein G[36] as a sensor. Protein G is a Streptococcal bacteria that is used for purifying antibodies through its binding to Fc (Fragment constant) and Fab (Fragment antigen binding).[37] During IgG translocation through a graphene nanopore, protein G interrogates different fragments of IgG through binding and protein-protein interactions,[37] which give rise to new

signatures and better signal to noise ratio (SNR) in detection of these fragments (Figure 5.1.a). Nanofluidic measurements also provide useful signatures for discrimination of IgG subclasses and their shapes. We computed the flux of water molecules through a graphene nanopore for different IgG subclasses. To show the versatility of our approach, we detected and scanned a large number of different classes of transmembrane, peripheral, globular and antibody proteins. To compare the atomic resolution obtained with a graphene nanopore to solid-state nanopores, we also tested the Si_3N_4 solid-state nanopore for IgG subclasses.

5.2 Methods

We performed extensive molecular dynamics (MD) simulations with NAMD 2.6 using the petascale Blue Waters machine.[38] The visualization of a typical simulation set up consisting of the protein, graphene nanopore, water and ions (~700,000 atoms) is shown in Figure 5.1.b. IgG, which is a protein complex composed of four peptide chains, contains two identical heavy chains and two identical light chains arranged in a Y-shape (Figure 5.1.c). The four subclasses of IgG show more than 95% homology in the amino acid sequences of the constant domains.[37, 39] The four IgG subclasses show their most conspicuous differences in the amino acid composition and structure of the 'hinge region', which is part of the molecule containing disulfide bonds (in cysteine residues) between the Y-heavy chains (Figure 5.1.c). For IgG2, we used the intact structure of anti-canine lymphoma monoclonal antibody (IgG2a with PDB code: 1IGT)[40]. For IgG3, we reconstructed the hinge region (with 11 disulfide bonds) based on the amino-acid decomposition described in Reference[41] (IgG2 and IgG3 structures are shown in Figure 5.1.c). For the functionalized pores, we anchored protein G (PDB code: 1GB1).[36] A pore with a diameter of 10.0 nm is drilled in the center of a 20 nm × 20 nm single layer graphene. Our initial studies show that a pore diameter of less than 10 nm cleaves the IgG proteins. Initially, proteins were placed at the

mouth of the graphene nanopore where the protein axis (z direction) is along the graphene pore axis (Figure 5.1.b). Proteins and graphene nanopore are submersed in water and salt ionic solution. The ionic concentration of NaCl is 0.5 M. We used the CHARMM27 force field[42] parameters for all the proteins, TIP3P water molecules, graphene and ions. SHAKE algorithm was used to maintain the rigidity of the water molecules. Periodic boundary condition is applied in all the three directions. The cut off distance for the LJ interactions is 15 Å. The long-range electrostatic interactions were computed by using the Particle-Mesh-Ewald (PME) method. The time step is selected to be 1 fs. For each simulation, energy minimization was performed for 100,000 steps. Systems were then equilibrated for 1 ns with NPT ensemble at 1 atm pressure and 300 K temperature. NPT simulation ensures that the water concentration is equal to the bulk value of 1 g/cm^3. The simulation was then performed in NVT ensemble. Temperature was maintained at 300 K by applying the Nosè-Hoover thermostat with a time constant of 0.1 ps. Before applying the electric field, equilibration for 2 ns was performed in NVT. Production simulations were performed by applying an external electric field in the z-direction. The external electric fields are reported in terms of a transmembrane voltage difference $V = EL_z$, where E is the electric field strength and L_z is the length of the simulation system in the z direction.[28] To overcome computational limitations, we used steered molecular dynamics (SMD) with a very slow velocity of 0.00001 Å/fs which results in translocation times in the order of nanoseconds. We monitored the time-dependent ionic current, *I(t)*, in the pore. We computed the ionic current through the nanopore by using the definition of current, $I=dq/dt$, as $I(t) = \frac{1}{L_z}\sum_{i=1}^{n} q_i \left[\frac{z_i(t+\delta t) - z_i(t)}{\delta t} \right]$, where the sum is for all the ions, δt is chosen to be 5 ps, and z_i and q_i are the z-coordinate and charge of ion i, and n is the total number of ions, respectively. The ionic current data is block averaged over intervals of 100 ps. We computed the time-dependent flux of water through the graphene nanopore

by counting the net amount of water molecules transported through the pore every 0.25 ns.[43] Each simulation was repeated 5 times with different velocity seeds to collect enough statistics.

5.3 Results and Discussion

We found distinguishable ionic current signals for the translocation of IgG2 and IgG3 through a graphene nanopore (Figures 5.1.d and 5.1.e). The ionic currents are in the order of nA which are consistent with experimental results.[1] In all time-dependent ionic current plots, the molecular features of the protein are reflected in the ionic current fluctuations as the protein translocates through the nanopore. As IgG protein translocates, Fc blocks the pore to a large extent (Figures 5.1.d and 5.1.e). I_0 represents the statistically averaged ionic current for the graphene nanopore in the absence of protein, which is 8.5 nA for an applied potential of V=180 mV (dashed line in Figures 5.1.d and 5.1.e). When Fc translocates through the pore, the averaged ionic current of Fc drops to 5.5 ~ 6.5 nA ($0.6I_0$ ~ $0.65I_0$). After Fc is translocated, the hinge region crosses the nanopore. A significant current recovery (I=8.25 nA) is observed during hinge translocation of IgG3 with the hinge current blockade duration of ~2 ns (Figure 5.1.e). For IgG2, due to the shorter hinge region (3 cysteine residues), the current only increases to I=7.85 nA and the hinge current blockade duration is ~0.4 ns (Table 5.1). The approximate translocation time for each hinge disulfide bridge is 0.11 ns. Based on our calculations, on an average, the hinge region ionic current is 0.92 I_0. The combination of translocation time and ionic current of the hinge region can be used to discriminate between IgG subclasses because the minor structural differences in the subclasses lie within the hinge region and the number of disulfide bonds. Another striking difference between IgG2 and IgG3 ionic current signature is associated with the Fab current. IgG2 Fabs translocate separately while IgG3 Fabs translocate together and simultaneously through the pore (we observed this phenomena in all our simulations). Figure 5.1.d shows a current recovery between Fab1 and

Fab2 translocation for IgG2, while Figure 5.1.e shows no current recovery for IgG3 Fabs translocation. The total ionic currents for IgG2 and IgG3 are 7.12 and 6.14 nA which serve as another signature to distinguish between the two subclasses. To demonstrate the applicability and reproducibility of our results, we increase the bias to V=480 mV and repeat the simulations. The *I-V* curve of the graphene nanopore with diameter, D=10 nm, shows a current of I_0=21 nA for V=480 mV (Figure 5.1.f). The translocation history and the change in ionic current of IgG2 and IgG3 through a graphene nanopore with V=480 mV show the same characteristics as the V=180 mV case (Figures 5.1.g and 5.1.h). The total ionic currents of IgG2 and IgG3 (18.72 and 17.10 nA, respectively) also exhibit similar characteristics. The average ionic current recovery for the hinge region is 0.86 I_0. Also, in the case of V=480 mV, the translocation time of IgG3 hinge is 5 times higher than that of IgG2. The simultaneous translocation of IgG3 Fabs occurs more clearly in the higher potential case (a long and continuous blockade in the Fabs translocation seen in Figure 5.1.h). Table 5.1 summarizes the ionic current signatures for IgG2 and IgG3 and the structural features that can be extracted from the signal (at bias=180 mV).

Water flux calculations for IgG2 and IgG3 translocation reveal a significant difference both in the total number (3448 more water molecules transported for IgG2 compared to IgG3) and the average flux (IgG2:456 #/ns, IgG3: 247.12 #/ns) (Figures 5.1.i and 5.1.j, and Table 5.1). During passage of Fc and Fabs, the flux of water decreases because of the pore blockade (Figures 5.1.i and 5.1.j). IgGs act like a “syringe”, mechanically pumping water during translocation. Before Fc passage (designated as pre-Fc period in Figures 5.1.i and 5.1.j), water flux increases significantly. During translocation of the hinges, water flux decreases due to the absence of the syringe effect. Therefore, the longer hinge region and simultaneous Fab translocation of IgG3 causes less pumping of water

molecules. The proximity of the Fabs to Fc in IgG2 makes its syringe behavior less leaky and more efficient, giving rise to better recognition of IgGs through their shape (Table 5.1).

To compare the flexibility of IgG2 and IgG3 during translocation, we monitored the Fab1-Fab2 angle (θ) while translocation occurs (Figure 5.2.a). First, we observed that the change in θ for IgG3 occurs with a 1.5 ns delay compared to that of IgG2 and this can be attributed to the longer hinge of IgG3. Second, change in θ is more pronounced in IgG3 compared to IgG2. Minimum θ is 65° and 23° for IgG2 and IgG3, respectively (Figure 5.2.a). Prior studies have shown that the flexibility of IgG3 is the highest among all the other subclasses of IgG.[44] Our results are consistent with the experimental measurement of the flexibility of IgGs.[44] Once the IgGs translocate through the pore, the Y-shape of the IgGs is recovered. The snapshots of IgG3 translocation are shown in Figure 5.2.b. The conformational changes of IgG mostly occur in the Fab segments. Some of these conformational changes (changes in θ) are due to the partial adhesion of Fabs to the graphene surface. We also computed the single Fab stretch (elongation) during the translocation process (see APPENDIX D). The stretching of IgG2 Fabs is more than that of IgG3 Fabs due to the sequential translocation of Fabs in IgG2.

To further differentiate between various IgG subclasses, we anchored biological markers to graphene. Protein G[36] receptor is a molecular interrogator of various IgG subclasses because it binds to Fc/Fab regions of IgGs[37, 39]. In prior experiments in solid state Si_3N_4 receptor-modified nanopore, protein A was used.[1] First, we tethered a single protein G to graphene nanopore and a bias of 180 mV is applied (Figure 5.3.a). I_0 does not change significantly compared to the pristine graphene nanopore (I_0=8.86 nA). $I_{Fc,Func}$ (the current associated with Fc translocation) is 3.56 nA for both IgG2 and IgG3 translocation (in protein G functionalized pore) compared to the pristine graphene nanopore with I_{Fc}= 5.25 nA (Figure 5.3.b and 5.3.c). SNR of I_{Fc} for pristine graphene is,

SNR_p= 6.23, and for the functionalized protein G case, SNR_G=10.1, revealing that the detection of Fc is enhanced for the functionalized pore (see APPENDIX D for SNR calculation). We did not observe a significant change in I_{Hinge} with protein G functionalization; however, the complete blockade of Fc with protein G functionalization provides a better estimation of the hinge length since I_{Hinge} starts right after I_{Fc}. To understand why $I_{Fc, Func} < I_{Fc}$, we computed the hydrogen bonds (HB) formed between protein G and IgG2 during translocation (Figure 5.3.d). 4-5 HB are formed during Fc translocation which highlights the strong electrostatic interactions between protein G and Fc. Surprisingly; no HB is formed during hinge and Fab translocation. HB forms between the residue MET1 of protein G and residues His 302, 464, 467 and MET 265 of Fc segment (Figure 5.3.e) which is consistent with ^{13}C-NMR experimental data on the binding sites of protein G.

To further understand the effect of protein G functionalization, we tethered four protein Gs which are equi-spaced on the edge of the graphene nanopore (Figure 5.3.f). In this case, I_0 reduces to 8.0 nA and Fc blockade is enhanced for both IgG2 (2.1 nA, Figure 5.3.g) and IgG3 (1.8 nA, Figure 5.3.h). The computed SNR for Fc current ($I_{Fc, Func-4G}$) is equal to 12.3. The enhancement in the ionic signal is due to the enhanced blockade of the Fc segment which can be explained from the stronger electrostatic protein-protein interactions (Figure 5.3.f).

The averaged ionic current associated with Fc and hinge for different graphene nanopore architectures (*e.g.* pristine, functionalized with a single protein G and functionalized with four proteins Gs) is summarized in Figure 5.4.a. I_{Fc} decreases as we increase the number of anchored protein Gs on the edge, giving rise to a higher SNR and better recognition of Fc translocation and identification of hinge data. Once Fc translocation is complete for each IgG, IgG subclasses can be distinguished from the duration of the ionic current recovery of the hinge region (IgG3 is 5 times higher than that of IgG2). A non-significant drop in the current of the hinge fragment is

observed as we increase the number of protein Gs which can be attributed to van der Waals interaction of Cysteine-Proline residues with protein G.

To compare the performance of a graphene nanopore with a solid-state nanopore (Si_3N_4),[1, 2, 18] we translocated IgG2 and IgG3 through a solid-state nanopore (Figure 5.4.b) with a diameter of D=10 nm (the same diameter as that of a graphene nanopore) and an applied potential difference of V=180 mV (see simulation details in APPENDIX D). Generally, the length of solid-state nanopores is 5-10 nm.[1, 2] During translocation of both IgG2 and IgG3, a solid-state nanopore envelopes the whole protein, mixing the currents from different fragments of IgGs. We observed a flat, indistinguishable current during translocation of IgG2 (Figure 5.4.c) and IgG3 (see APPENDIX D). Thus, many structural details of IgGs are missed with a solid-state nanopore. Our finding is consistent with the experimental results of a pristine solid-state nanopore (not functionalized) being unable to discriminate between IgG subclasses.[1, 2] Also, the signal strength is in the range of noise, giving a low SNR of 2.0 which makes detection difficult.

To demonstrate the versatility of our molecular recognition approach in proteomics and structural biology, we scanned 4 different types of proteins: Titin, Myoglobin (globular), Ubiquitin (peripheral) and MTHK (transmembrane ion channel) by translocating them through a graphene nanopore (Figure 5.4.d, APPENDIX D for detailed time-dependent ionic current data). We found different nanopore blockade times (τ_b) representing different protein lengths (Figure 5.4.e). The blockade time and time-dependent ionic current can be used to detect, count and discriminate between these types of proteins. Moreover, the profile and shape of each protein, scanned by the graphene nanopore, is presented in the APPENDIX D. Our ionic current results should also hold for the mixture of proteins since the proteins translocate through the comparably-narrow nanopore one at a time.

5.4 Conclusion

In summary, we have used graphene nanopores for sequencing proteins using ionic current blockade and water flux measurement. IgG subclasses, with subtle differences in their hinge amino acids compositions, were distinguished by the recovery current signatures (hinge translocation time and current intensity). Functionalizing a graphene nanopore with protein G receptor increases SNR of Fc detection giving rise to a better detection of IgG subclasses. We have also demonstrated that a graphene nanopore can detect different protein types. The comparison of a single-atom thick graphene nanopore with a solid-state nanopore reveals that IgG subclasses could not be discriminated with a solid-state nanopore. IgG subclasses exhibit distinguishable water pump strength through graphene nanopores giving rise to an additional subclass discrimination mechanism. Combination of the two signals (ionic current and water flux) can greatly contribute to high precision detection and discrimination between IgGs.

5.5 Figures

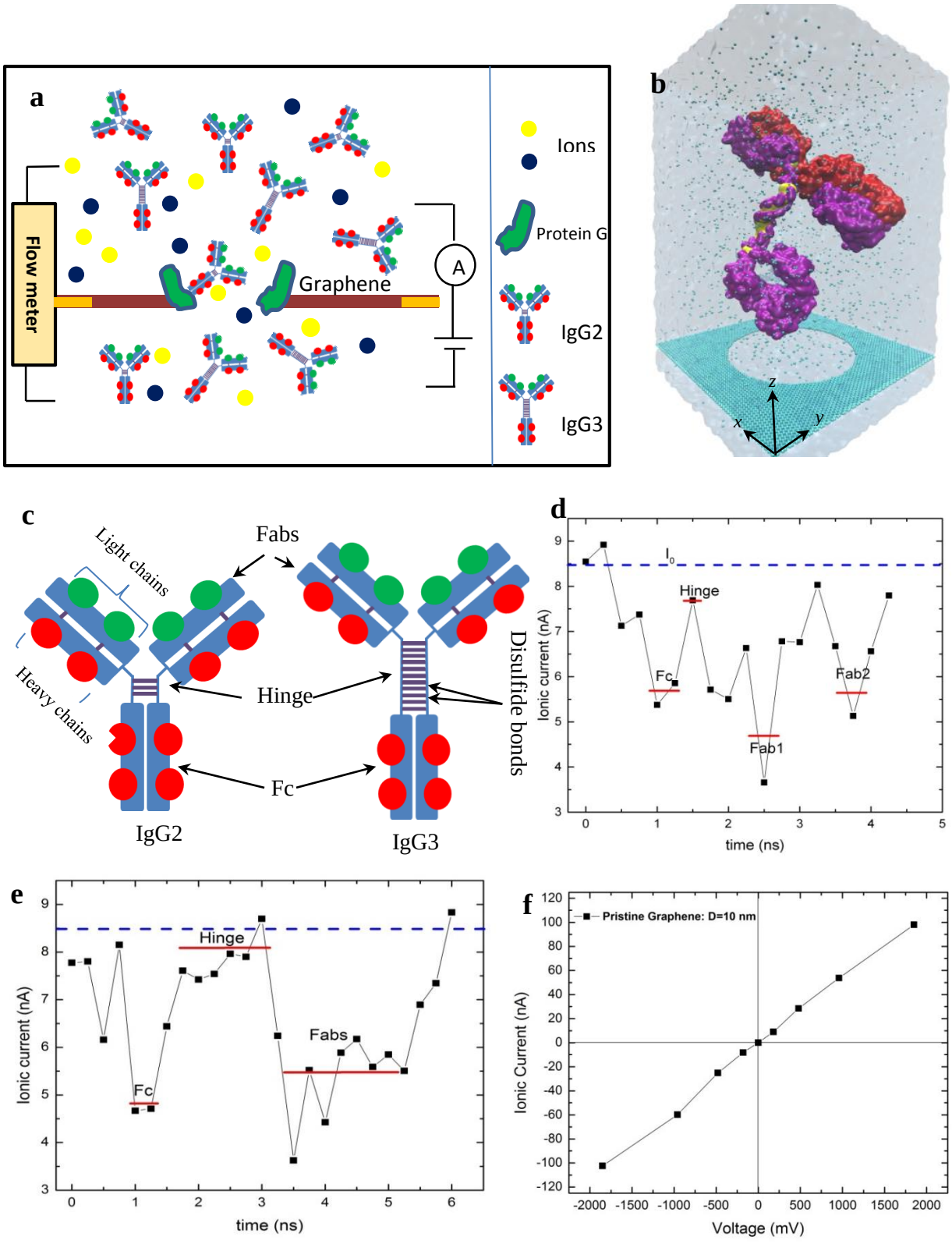

Figure 5.1

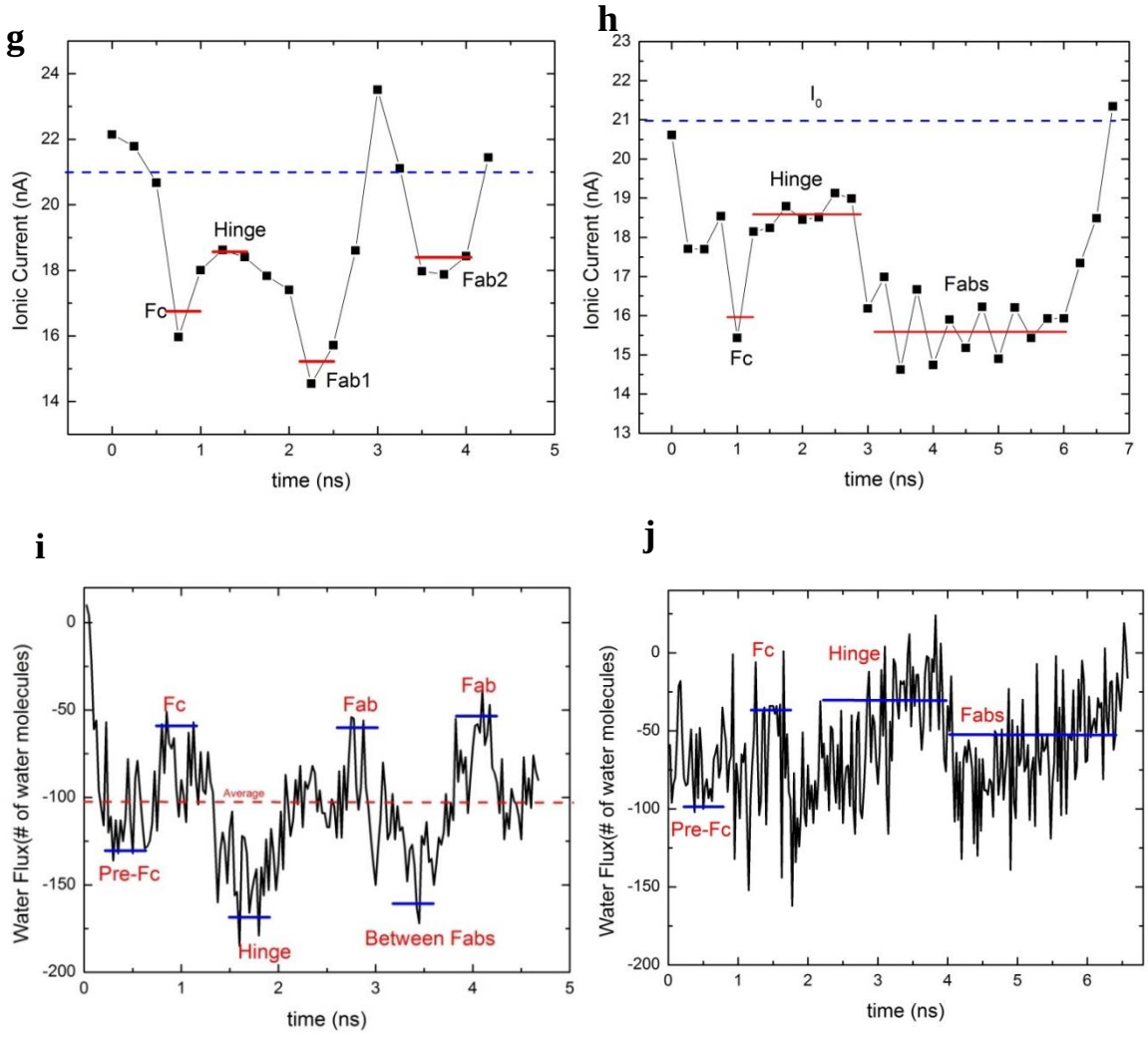

Figure 5.1. (cont.) a| Cartoon representation of a graphene nanopore protein sensor and scanner. Graphene can be anchored with biological markers like protein G receptor (Green molecule anchored to graphene edge) or protein A. Ionic solution (dark blue and yellow) molecules are electro-kinetically driven through the pore by applying an electrical potential gradient. Proteins (here IgG2 and IgG3) are scanned and detected by transient blockades, transverse tunneling current and water flux. **b|** Simulation system consisting of IgG3 protein (red: light chains, velvet: heavy chains, yellow: disulfide bonds in the hinge region), ions (pale green) and graphene is green. **c|** Comparison of the structural differences in IgG2 and IgG3. The most notable difference between IgG subclasses is in the hinge regions with variable number of amino-acids and disulfide bonds in cysteine residues. **d|** Time-dependent ionic current of IgG2 translocation through a pristine graphene nanopore. The blue dashed line represents I_0 (graphene nanopore ionic current at the same applied bias (V=180 mV) without protein translocation). **e|** plot **d** for IgG3 translocation. **f|** Characteristic **I-V** curve of graphene nanopore without protein. **g|** Time-dependent ionic current plot of IgG2 translocation for a bias of 480 mV. **h|** Time-dependent ionic current plot of IgG3 translocation for a bias of 480 mV. **i|** Water flux fluctuations during IgG2 translocation (V=180 mV). Different segments of IgG2 are designated to indicate their relative flux. The average and total flux are noted. **j|** Water flux fluctuations during IgG3 translocation (V=180 mV). Different segments of IgG3 are designated to show their relative flux. The average and total flux are noted.

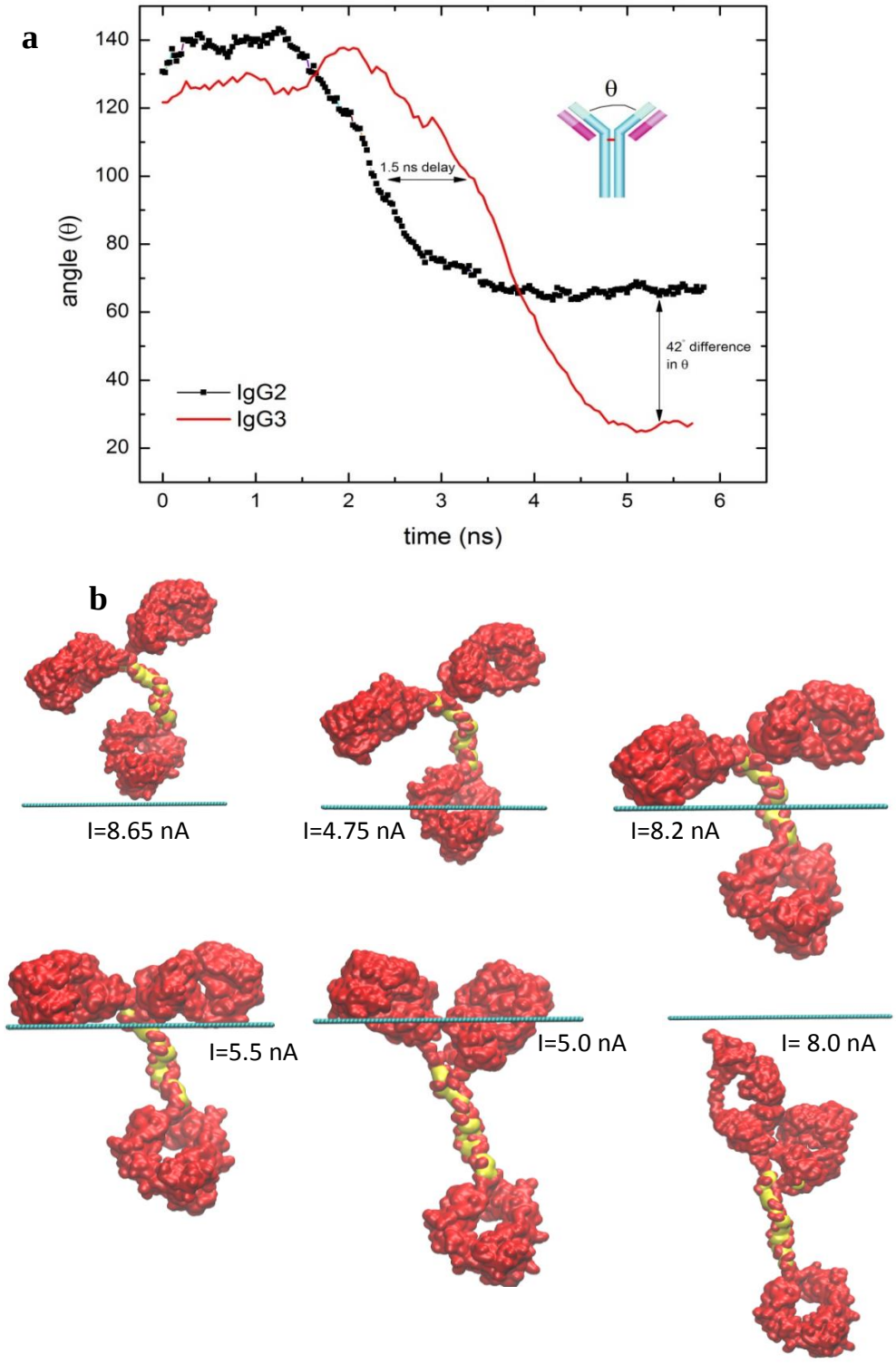

Figure 5.2. a| Fab-Fab angular (θ) deflection during translocation of IgG2 and IgG3. **b|** snapshots of conformational changes, averaged current and translocation history of IgG3 through a graphene nanopore (yellow color in the hinge region representing the disulfide bonds); similar snapshots for IgG2 are presented in APPENDIX D.

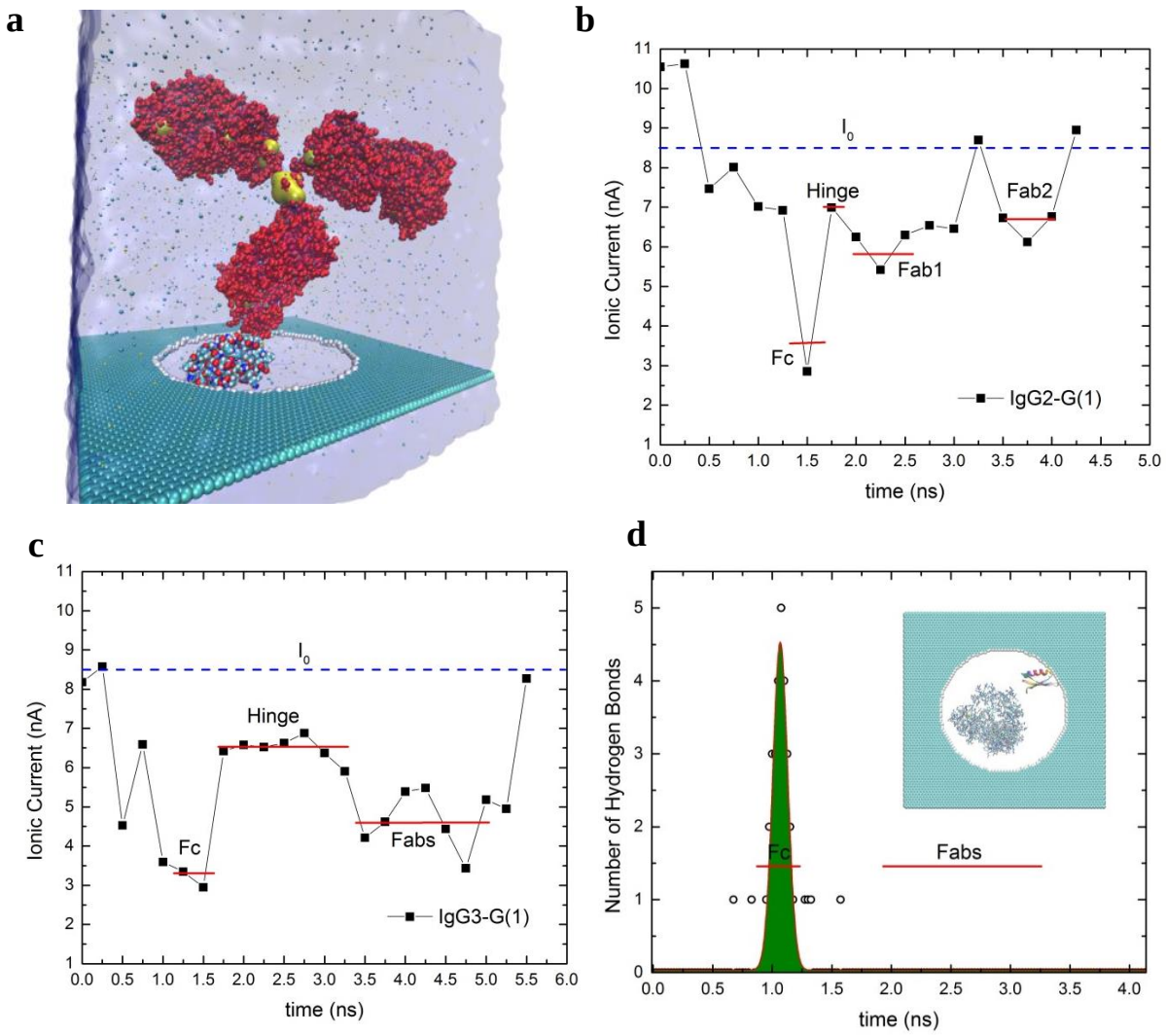
a
b
Ionic Current (nA)
time (ns)
I_0
Hinge
Fab2
Fab1
Fc
IgG2-G(1)
c
Ionic Current (nA)
time (ns)
I_0
Hinge
Fc
Fabs
IgG3-G(1)
d
Number of Hydrogen Bonds
time (ns)
Fc
Fabs

Figure 5.3

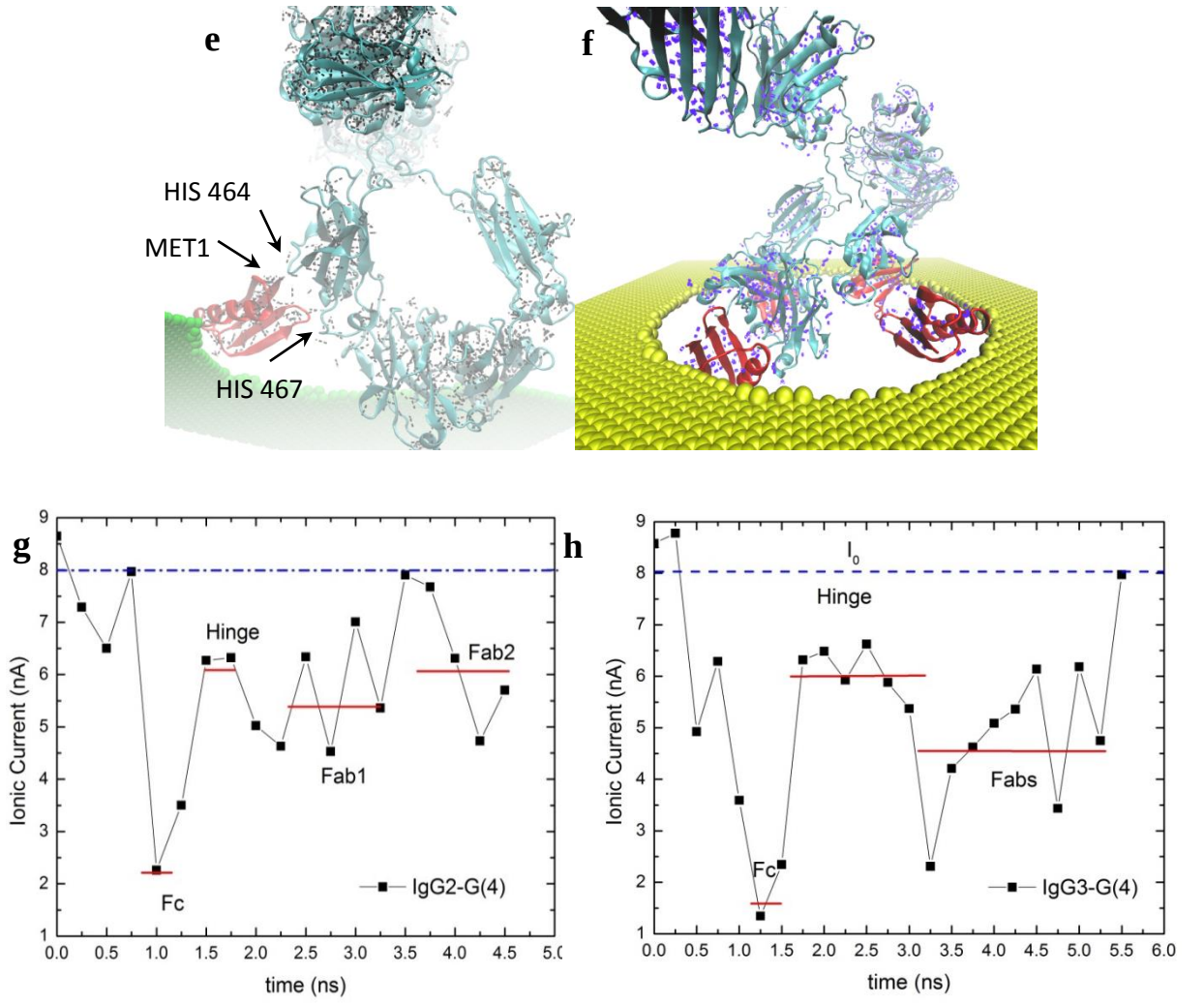

Figure 5.3. (cont.) a| Simulation box including graphene nanopore, protein G tethered to graphene nanopore edge, and solutes. The disulfide bonds in Cysteine residues at the hinge are shown in yellow. **b|** Time-dependent ionic current of IgG2 for a potential difference of V=180 mV and **c|** Plot (b) for IgG3 **d|** Time-dependent hydrogen bonds formed between protein G and IgG2, the Gaussian curve is peak enveloped to hydrogen bond numbers to demonstrate the intensity and peak of electrostatic bonding activity between IgG and protein G marker. **Inset**: top view of graphene nanopore, protein G and Fc part of IgG2. **e|** Hydrogen bond network within IgG2, protein G and between protein G and Fc part of IgG2. HIS (marked) residues in Fc fragment and MET residues in protein G are responsible for protein-protein interactions. **f|** Graphene nanopore functionalized with four protein G molecules and the complex hydrogen bond/electrostatic network of protein-protein interactions during Fc translocation. The complex HB network, Fc and protein G almost block the pore entirely, leaving no more space for ionic current. **g|** Ionic current of IgG2 translocation through a graphene nanopore functionalized with four protein G molecules. **h|** Ionic current of IgG3 translocation through a graphene nanopore functionalized with four protein G molecules.

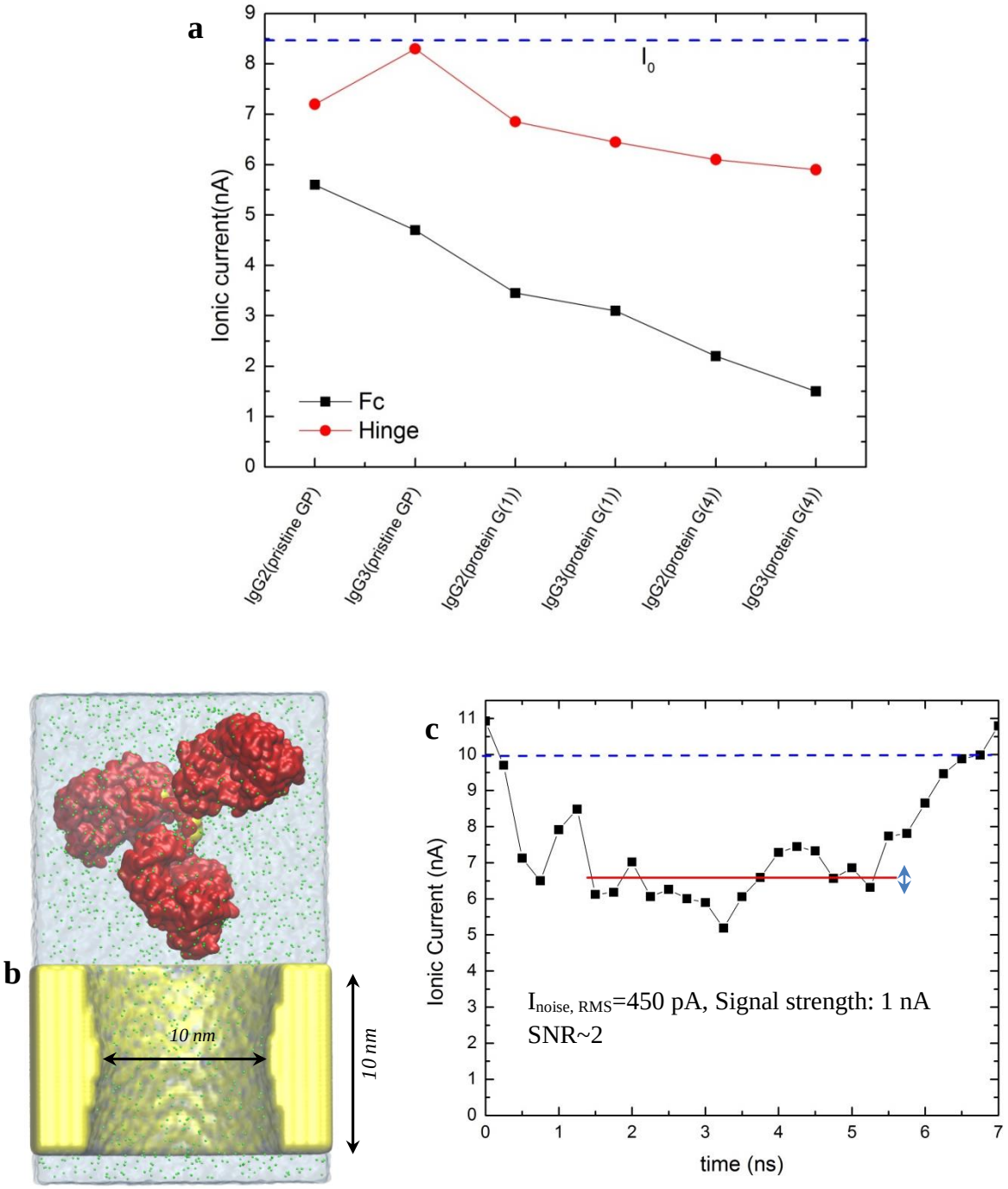

Figure 5.4. a| Averaged ionic current associated with different fragments of IgG2 and IgG3 for different pores (pristine nanopore, single protein G functionalization and four protein G functionalization). **b|** simulation set up for IgG2 translocation through a Si_3N_4 nanopore. **c|** Time dependent ionic current for IgG2 translocation through a Si_3N_4 solid-state nanopore. The red line represents the translocation history of IgG2 when its center of mass (COM) is inside the pore

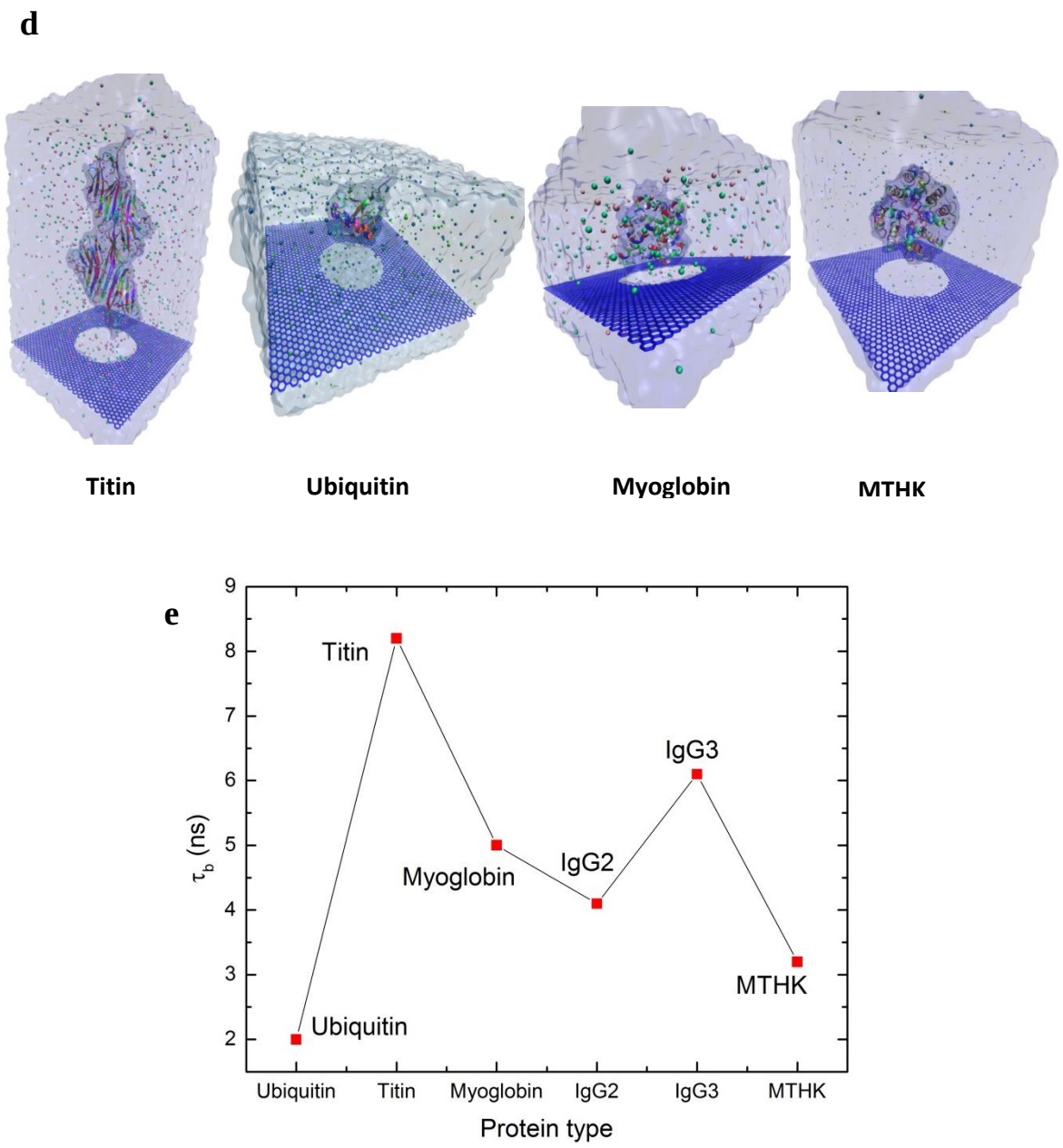

Figure 5.4.(Cont.) d| simulation snapshots of 4 diverse protein types (Titin, Myoglobin, Ubiquitin and MTHK). **e|** blockade time (τ_b) associated with the translocation of different proteins.

	Ionic current (IC) signatures				Water flux (#/ns)
IgG subclass	Blockade time (τ_b) (ns)	Hinge IC (nA)	Hinge blockade time ($\tau_{H,b}$)	Total IC (nA)	
IgG2	4.4	7.85	0.4	7.12	-456
IgG3	6.2	8.25	2.0	6.14	-247.12

Table 5.1. Signatures obtained through two different signal types for detection and discrimination of IgG subclasses (IC signatures and water flux data are taken at bias=180 mV).

5.6 References

1. Wei, R. S.; Gatterdam, V.; Wieneke, R.; Tampe, R.; Rant, U. Stochastic Sensing of Proteins with Receptor-Modified Solid-State Nanopores. *Nat. Nanotechnol.* 2012, 7, 257-263.
2. Yusko, E. C.; Johnson, J. M.; Majd, S.; Prangkio, P.; Rollings, R. C.; Li, J. L.; Yang, J.; Mayer, M. Controlling Protein Translocation through Nanopores with Bio-Inspired Fluid Walls. *Nat. Nanotechnol.* 2011, 6, 253-260.
3. Han, A.; Creus, M.; Schurmann, G.; Linder, V.; Ward, T. R.; de Rooij, N. F.; Staufer, U. Label-Free Detection of Single Protein Molecules and Protein-Protein Interactions Using Synthetic Nanopores. *Anal. Chem.* 2008, 80, 4651-4658.
4. Han, A. P.; Schurmann, G.; Mondin, G.; Bitterli, R. A.; Hegelbach, N. G.; de Rooij, N. F.; Staufer, U. Sensing Protein Molecules Using Nanofabricated Pores. *Appl. Phys. Lett.* 2006, 88.
5. Kowalczyk, S. W.; Kapinos, L.; Blosser, T. R.; Magalhaes, T.; van Nies, P.; Lim, R. Y. H.; Dekker, C. Single-Molecule Transport across an Individual Biomimetic Nuclear Pore Complex. *Nat. Nanotechnol.* 2011, 6, 433-438.
6. Aksimentiev, A.; Heng, J. B.; Timp, G.; Schulten, K. Microscopic Kinetics of DNA Translocation through Synthetic Nanopores. *Biophys. J.* 2004, 87, 2086-2097.
7. Dekker, C. Solid-State Nanopores. *Nat. Nanotechnol.* 2007, 2, 209-215.
8. Li, J. L.; Gershow, M.; Stein, D.; Brandin, E.; Golovchenko, J. A. DNA Molecules and Configurations in a Solid-State Nanopore Microscope. *Nat. Mater.* 2003, 2, 611-615.
9. Howorka, S.; Cheley, S.; Bayley, H. Sequence-Specific Detection of Individual DNA Strands Using Engineered Nanopores. *Nat. Biotechnol.* 2001, 19, 636-639.
10. Venkatesan, B. M.; Bashir, R. Nanopore Sensors for Nucleic Acid Analysis. *Nat. Nanotechnol.* 2011, 6, 615-624.
11. Branton, D.; Deamer, D. W.; Marziali, A.; Bayley, H.; Benner, S. A.; Butler, T.; Di Ventra, M.; Garaj, S.; Hibbs, A.; Huang, X. H.; Jovanovich, S. B.; Krstic, P. S.; Lindsay, S.; Ling, X. S. S.; Mastrangelo, C. H.; Meller, A.; Oliver, J. S.; Pershin, Y. V.; Ramsey, J. M.; Riehn, R.; Soni, G. V.; Tabard-Cossa, V.; Wanunu, M.; Wiggin, M.; Schloss, J. A. The Potential and Challenges of Nanopore Sequencing. *Nat. Biotechnol.* 2008, 26, 1146-1153.
12. Majd, S.; Yusko, E. C.; Billeh, Y. N.; Macrae, M. X.; Yang, J.; Mayer, M. Applications of Biological Pores in Nanomedicine, Sensing, and Nanoelectronics. *Curr. Opin. Biotechnol.* 2010, 21, 439-476.
13. Steinbock, L. J.; Krishnan, S.; Bulushev, R. D.; Borgeaud, S.; Blokesch, M.; Feletti, L.; Radenovic, A. Probing the Size of Proteins with Glass Nanopores. *Nanoscale* 2014, 6, 14380-14387.
14. Derrington, I. M.; Butler, T. Z.; Collins, M. D.; Manrao, E.; Pavlenok, M.; Niederweis, M.; Gundlach, J. H. Nanopore DNA Sequencing with Mspa. *Proc. Natl. Acad. Sci. U. S. A.* 2010, 107, 16060-16065.
15. Purnell, R. F.; Schmidt, J. J. Discrimination of Single Base Substitutions in a DNA Strand Immobilized in a Biological Nanopore. *ACS Nano* 2009, 3, 2533-2538.
16. Deamer, D. W.; Akeson, M. Nanopores and Nucleic Acids: Prospects for Ultrarapid Sequencing. *Trends Biotechnol.* 2000, 18, 147-151.
17. Bayley, H.; Cremer, P. S. Stochastic Sensors Inspired by Biology. *Nature* 2001, 413, 226-230.
18. Larkin, J.; Henley, R. Y.; Muthukumar, M.; Rosenstein, J. K.; Wanunu, M. High-Bandwidth Protein Analysis Using Solid-State Nanopores. *Biophys. J.* 2014, 106, 696-704.
19. Geim, A. K.; Novoselov, K. S. The Rise of Graphene. *Nat. Mater.* 2007, 6, 183-191.
20. Garaj, S.; Hubbard, W.; Reina, A.; Kong, J.; Branton, D.; Golovchenko, J. A. Graphene as a Subnanometre Trans-Electrode Membrane. *Nature* 2010, 467, 190-U73.
21. Sathe, C.; Zou, X. Q.; Leburton, J. P.; Schulten, K. Computational Investigation of DNA Detection Using Graphene Nanopores. *ACS Nano* 2011, 5, 8842-8851.

22. Merchant, C. A.; Healy, K.; Wanunu, M.; Ray, V.; Peterman, N.; Bartel, J.; Fischbein, M. D.; Venta, K.; Luo, Z. T.; Johnson, A. T. C.; Drndic, M. DNA Translocation through Graphene Nanopores. *Nano Lett.* 2010, 10, 2915-2921.
23. Schneider, G. F.; Kowalczyk, S. W.; Calado, V. E.; Pandraud, G.; Zandbergen, H. W.; Vandersypen, L. M. K.; Dekker, C. DNA Translocation through Graphene Nanopores. *Nano Lett.* 2010, 10, 3163-3167.
24. Nelson, T.; Zhang, B.; Prezhdo, O. V. Detection of Nucleic Acids with Graphene Nanopores: Ab Initio Characterization of a Novel Sequencing Device. *Nano Lett.* 2010, 10, 3237-3242.
25. Traversi, F.; Raillon, C.; Benameur, S. M.; Liu, K.; Khlybov, S.; Tosun, M.; Krasnozhon, D.; Kis, A.; Radenovic, A. Detecting the Translocation of DNA through a Nanopore Using Graphene Nanoribbons. *Nat. Nanotechnol.* 2013, 8, 939-945.
26. Sint, K.; Wang, B.; Kral, P. Selective Ion Passage through Functionalized Graphene Nanopores. *J. Am. Chem. Soc.* 2008, 130, 16448-+.
27. Venkatesan, B. M.; Estrada, D.; Banerjee, S.; Jin, X. Z.; Dorgan, V. E.; Bae, M. H.; Aluru, N. R.; Pop, E.; Bashir, R. Stacked Graphene-Al_2O_3 Nanopore Sensors for Sensitive Detection of DNA and DNA-Protein Complexes. *ACS Nano* 2012, 6, 441-450.
28. Wells, D. B.; Belkin, M.; Comer, J.; Aksimentiev, A. Assessing Graphene Nanopores for Sequencing DNA. *Nano Lett.* 2012, 12, 4117-4123.
29. Garaj, S.; Liu, S.; Golovchenko, J. A.; Branton, D. Molecule-Hugging Graphene Nanopores. *Proc. Natl. Acad. Sci. U. S. A.* 2013, 110, 12192-12196.
30. Farimani, A. B.; Min, K.; Aluru, N. R. DNA Base Detection Using a Single-Layer MoS_2. *ACS Nano* 2014, 8, 7914-7922.
31. Saha, K. K.; Drndic, M.; Nikolic, B. K. DNA Base-Specific Modulation of Microampere Transverse Edge Currents through a Metallic Graphene Nanoribbon with a Nanopore. *Nano Lett.* 2012, 12, 50-55.
32. Yanan Zhao, B. A., Peiming Zhang, Hao Liu, Suman Sen, Weisi Song, JongOne Im, Brett Gyarfas, Saikat Manna, Sovan Biswas, Chad Borges, Stuart Lindsay. Single-Molecule Spectroscopy of Amino Acids and Peptides by Recognition Tunnelling. *Nat. Nanotechnol.* 2014.
33. Prasongkit, J.; Grigoriev, A.; Pathak, B.; Ahuja, R.; Scheicher, R. H. Transverse Conductance of DNA Nucleotides in a Graphene Nanogap from First Principles. *Nano Lett.* 2011, 11, 1941-1945.
34. Tsutsui, M.; Taniguchi, M.; Yokota, K.; Kawai, T. Identifying Single Nucleotides by Tunnelling Current. *Nat. Nanotechnol.* 2010, 5, 286-290.
35. Taussig, M. J. Studies on Antigenic Competition .1. Antigenic Competition between Fc and Fab Fragments of Rabbit Igg in Mice. *Immunology* 1971, 21, 51.
36. Gronenborn, A. M.; Filpula, D. R.; Essig, N. Z.; Achari, A.; Whitlow, M.; Wingfield, P. T.; Clore, G. M. A Novel, Highly Stable Fold of the Immunoglobulin Binding Domain of Streptococcal Protein-G. *Science* 1991, 253, 657-661.
37. Guss, B.; Eliasson, M.; Olsson, A.; Uhlen, M.; Frej, A. K.; Jornvall, H.; Flock, J. I.; Lindberg, M. Structure of the Igg-Binding Regions of Streptococcal Protein-G. *Embo J.* 1986, 5, 1567-1575.
38. Kale, L.; Skeel, R.; Bhandarkar, M.; Brunner, R.; Gursoy, A.; Krawetz, N.; Phillips, J.; Shinozaki, A.; Varadarajan, K.; Schulten, K. Namd2: Greater Scalability for Parallel Molecular Dynamics. *J. Comput. Phys.* 1999, 151, 283-312.
39. Ravetch, J. V.; Kinet, J. P. Fc-Receptors. *Annu. Rev. Immunol.* 1991, 9, 457-492.
40. Harris, L. J.; Larson, S. B.; Hasel, K. W.; McPherson, A. Refined Structure of an Intact IgG2a Monoclonal Antibody. *Biochemistry* 1997, 36, 1581-1597.
41. Michaelsen, T. E.; Frangione, B.; Franklin, E. C. Primary Structure of Hinge Region of Human Igg3 - Probable Quadruplication of a 15-Amino Acid Residue Basic Unit. *J. Biol. Chem.* 1977, 252, 883-889.
42. MacKerell, A. D.; Banavali, N. K. All-Atom Empirical Force Field for Nucleic Acids: Application to Molecular Dynamics Simulations of DNA and Rna in Solution. *J. Comput. Chem.* 2000, 21, 105-120.

43. Suk, M. E.; Aluru, N. R. Water Transport through Ultrathin Graphene. *J. Phys. Chem. Lett.* 2010, 1, 1590-1594.
44. Roux, K. H.; Strelets, L.; Michaelsen, T. E. Flexibility of Human IgG Subclasses. *J. Immunol.* 1997, 159, 3372-3382.

CHAPTER 6: **Conclusions**

In conclusion, we studied and investigated different nanopore architectures and materials to detect and sense biological molecules. We tried to address the challenges facing the nanopore sensors in their functionality using extensive atomistic simulations and modeling. We demonstrated that Molybdenum Disulphide (MoS_2) nanopore shows a distinct ionic current signal for single nucleobase detection with a SNR of 15. MoS_2 also shows a characteristic response in total DOS change for each base. The band gap of MoS_2 is significantly changed when bases are placed on the top of pristine MoS_2, which makes it a good material for base detection. In contrast to graphene, for MoS_2 nanopore, DNA shows a more distinguishable signature per base. During translocation of DNA, bases stick to the graphene surface while MoS_2 nanopore shows a non-sticky behavior.

In chapter 3, we introduced mechano-sensitive channel of large conductance, MscL as an alternative to Alpha-Hemolysin and MspA pores for DNA detection. We have shown that a mechanical signature, namely tension in the membrane, can be effective for DNA detection through MscL. Four distinct force signals were detected for bases with forces decreasing in the order T> G> C>A. An initially-closed MscL opens to ssDNA due to electric-field mediated translocation and the pore geometry adapts to the size of each base. Ionic current signal is also distinct for each base, making MscL pore amenable for detecting bases with two parallel signals, namely, membrane tension and ionic current. We found a completely different gating mechanism of MscL during ssDNA translocation compared to its normal operation. The translocation speed of DNA in MscL is roughly one order of magnitude slower compared to that in MspA.

We also demonstrated that the hybrid pore of DNA origami-graphene can yield distinguishable dwell time for DNA bases. Four different nanopores i.e. bare graphene, 1 layer DNA origami, 1

layer DNA origami -graphene, and 2layer DNA origami-graphene were characterized in terms of ionic current and conductance. The pore conductance highly correlates with the thickness of the pore. The initial functionalization of graphene pore with base T remains intact during electrophoretic translocation of DNA bases. The combination of distinguishable dwell time and ionic current along the slower speed of translocation make hybrid origami-graphene pore amenable for better DNA detection compared to bare graphene. The hydrogen bonds between translocating DNA and DNA origami at the pore are the origin of distinguishable dwell time.

In addition to DNA sequencing studies that we performed, we used graphene nanopore for the detection of natively folded proteins. We mainly focused on the detection of IgG subclasses. IgG subclasses, with subtle differences in their hinge amino acids compositions, were distinguished by the recovery current signatures (hinge translocation time and current intensity). Functionalizing a graphene nanopore with protein G receptor increases SNR of Fc detection giving rise to a better detection of IgG subclasses. We have also demonstrated that a graphene nanopore can detect different protein types. The comparison of a single-atom thick graphene nanopore with a solid-state nanopore reveals that IgG subclasses could not be discriminated with a solid-state nanopore. IgG subclasses exhibit distinguishable water pump strength through graphene nanopores giving rise to an additional subclass discrimination mechanism. Combination of the two signals (ionic current and water flux) can greatly contribute to high precision detection and discrimination between IgGs.

APPENDIX A

A.1 Orientation of the bases inside the pore

The ionic current blockade variations for bases can be explained by the topology, partial charges and mainly, the orientation of each base inside the pore[1, 2]. We measured the time-averaged orientation of each base as it passes through the MoS_2 nanopore. For each base, we defined the plane, P1, as passing through the hexagonal ring of the base. θ is defined as the angle between the MoS_2 plane (xy) and the plane P1 that passes through the hexagonal ring of base G and is about y axis (θ for base G is shown in Figure A.1). α is defined as the angle between MoS_2 plane (xy) and P1 planes that is about x axis. For each base, angles θ and α are defined accordingly. For biases of V=2.0-3.0 volts, the angles θ and α are averaged for each base and for the time the base occupied the pore. Figure A.2 and A.3 represent the time-averaged θ and α angles for different biases.

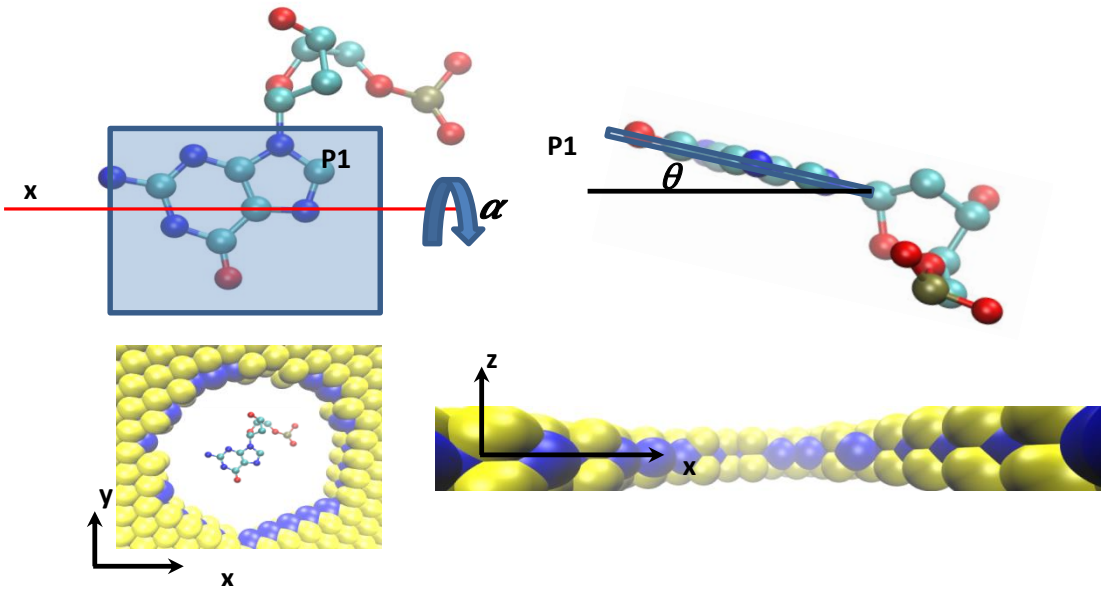

Figure A.1: The orientation of base G and the definition of angles **θ** and **α** with respect to the MoS_2 nanopore plane (xy).

In Figure A.2, it can be observed that the opening of the pore is larger for A and T bases compared to C and G (angle **θ** is larger). Angle θ is largest for base A and smallest for base C and follows the relation A>T>G>C which is consistent with the ionic current blockade and experimental results presented in the main text. It's notable that a similar correlation is not observed for angle **α** for different biases as shown in Figure A.3.

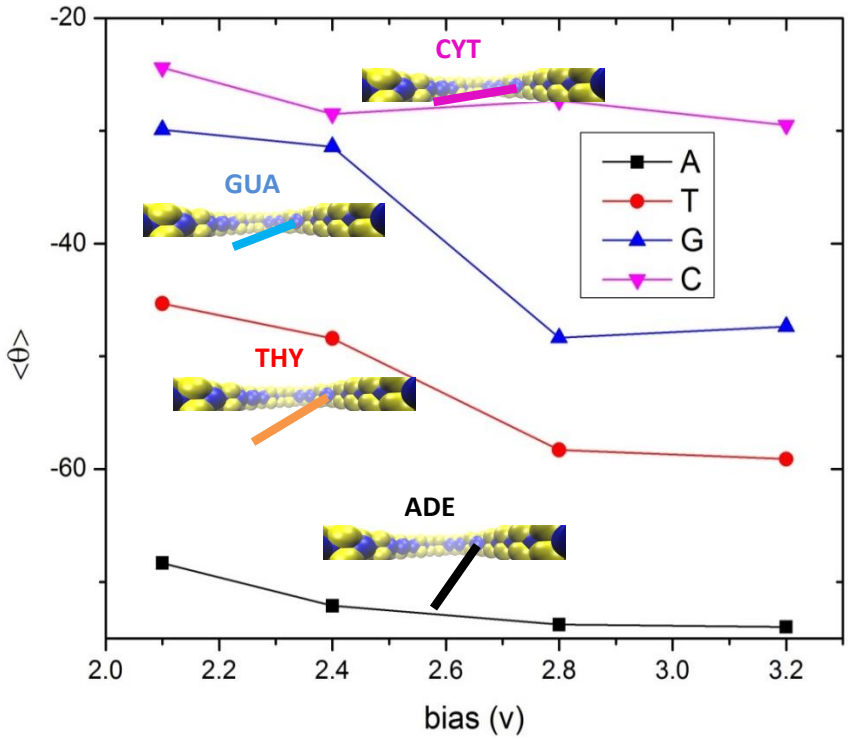

Figure A.2: The time-averaged angle **θ** for biases 2.1-3.2 volts for bases A, G, C and T inside the MoS_2 nanopore.

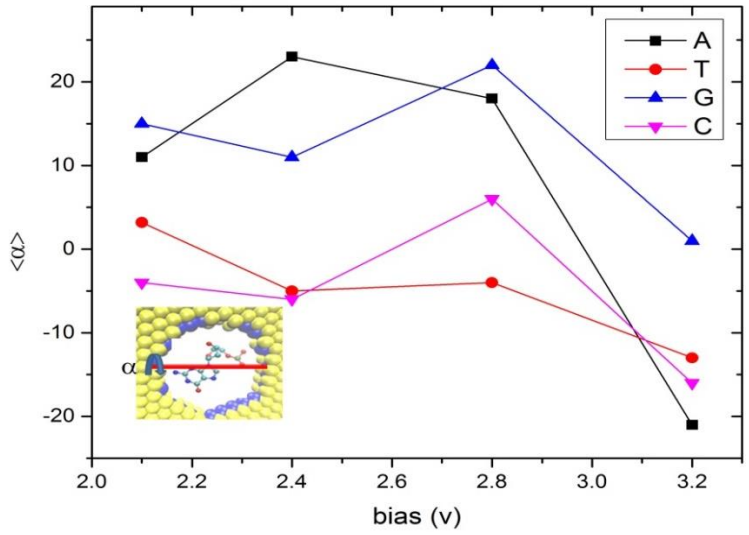

Fig A.3: The time-averaged angle α for biases 2.1-3.2 volts for bases A, G, C and T inside the MoS_2 nanopore.

A.2 Water flux through the MoS_2 pore during DNA translocation

We computed water flux through the nanopore during the translocation of DNA. Without the applied bias, the time-averaged flux of water is zero. Figure A.4 shows the initial configuration of DNA with respect to the pore mouth, ions and water. When a bias is applied, the negatively charged DNA translocates through the nanopore. During the translocation of nucleotides, based on the charges of the bases that occupy the pore, a transient flux of ions and water is observed. We monitored the flux of water by counting the permeated water molecules through the pore. Figure A.2.b shows the flux of water molecules versus time for a bias of V=2.6 volts. Initially, for t=0 to 40 ps, the flux is near zero. During this time window, DNA approaches the nanopore mouth. For t>40 ps, water molecules (normally 1-2) are pulled through the nanopore by both DNA bases and ions. In Figure A.5, the number of water molecules passing through the pore is shown. Due to translocation, bases mostly occupy the pore and there is less space for water molecules and ions to

be translocated (for larger diameter pore, the number of water molecules and ions significantly increases). For t>400 ps, the flux of water becomes zero.

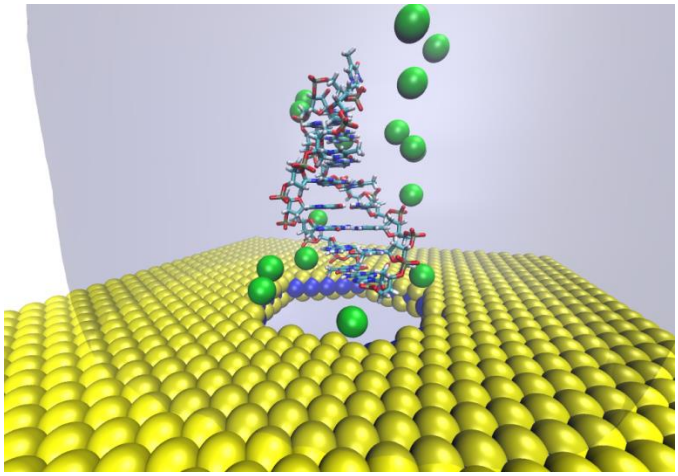

Figure A.4: snapshot of DNA, ions, water and MoS_2 nanopore.

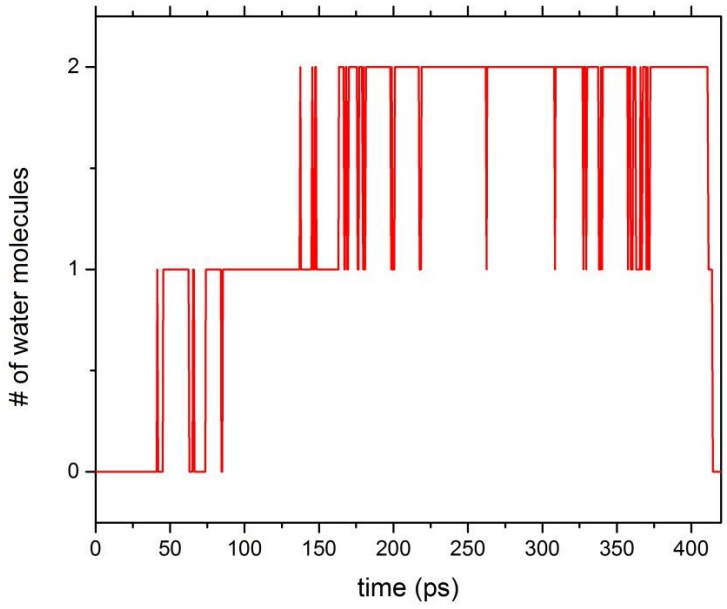

Figure A.5: Water flux through MoS_2 nanopore during DNA translocation.

A.3 Translocation time correlation for different biases

The translocation time of hairpin DNA with 16 bases was estimated for different biases. The translocation time of DNA nucleotides is defined as the time needed for complete translocation of all the 16 bases. For all biases, the DNA is placed at the mouth of the nanopore and translocation time is determined to be the time the last atom of DNA exits the pore. For biases smaller than 1.4 volts, complete translocation isn't observed in nanosecond scale (perhaps the translocation event occurs in ~μs scale). Figure A.6 shows the translocation time for different biases. Extrapolating the data for biases of 500 mV-1000 mV, we infer that the translocation time will be in the order of ~5-10 μs which is consistent with experimental results.[3, 4]

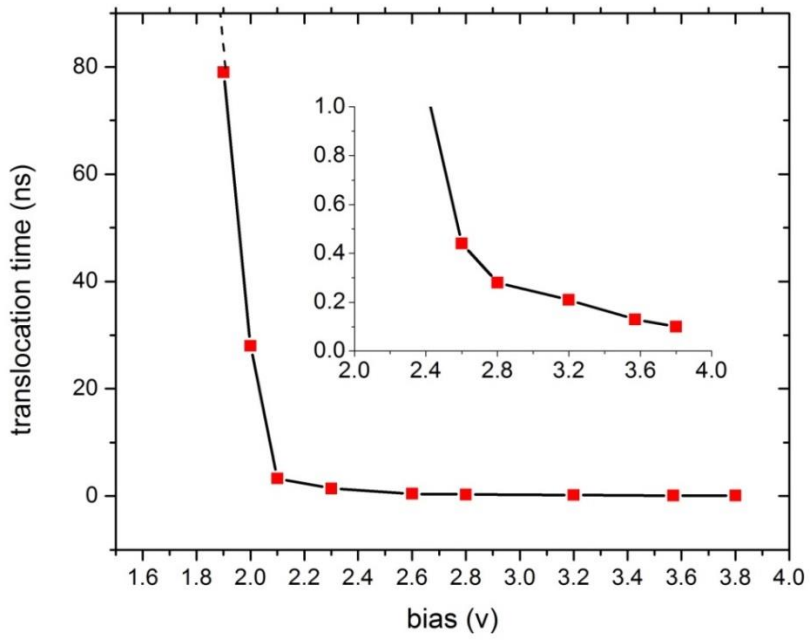

Figure A.6: DNA translocation time through the MoS_2 nanopore for different biases.

A.4 Comparison of conductance states and signal/noise ratio in MoS_2 and Graphene nanopores.

A.4.1 Conduction States

We characterize the current blockades produced when each base of DNA was electrophoretically driven through the MoS_2 and graphene nanopores. The ionic current blockade is a function of pore thickness, pore material, applied bias, etc.[4,5] To compare the ionic current blockade characteristics for the two pores (MoS_2 and graphene), we simulated the same DNA type (1ac7 structure, www.pdb.org)[6] and applied the same bias of 2.6 volts. The initial number of ions and water molecules are selected to be identical. The pore diameter is selected to be 2.3 nm for both MoS_2 and graphene nanopore. We computed the ionic current by using the method explained in the main text. The ionic current is shown in Figure A.7. The significant difference between the ionic current plots for MoS_2 and graphene is the number of blockade states (or conductance states). For graphene, we observed only two states for ionic current blockade while for MoS_2 nanopore, 4 conductance states were observed. Higher states of conductance can provide more distinct sequencing signals for distinguishing among the four bases. The average residence time of the bases is 2 times longer in MoS_2 than in graphene. It's notable that the ionic current is 8 nA for the bias of 2.6 volts and without DNA.

The small thickness of graphene compared to MoS_2 and the existence of hydrophilic sites of Molybdenum is the origin of noise and lower ionic conductance states. Interestingly, it's been shown that multilayer graphene (with higher thickness) gives better ionic current signal compared to a single layer graphene and this is consistent with our observations.[1, 7]

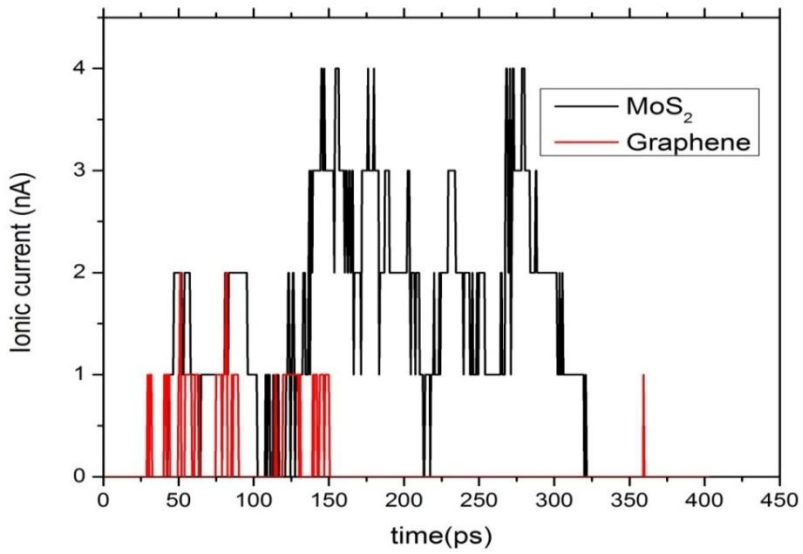

Figure A.7: Ionic current for DNA translocation through the MoS_2 and graphene nanopore for the bias (2.6 volts).

A.4.2 Signal to noise ratio (SNR)

The SNR is defined as[8]

$$SNR = \frac{|\Delta I|}{I_{noise,RMS}} \tag{A.4.1}$$

where $|\Delta I|$ is the absolute current change due to DNA translocation and $I_{noise,RMS}$ is the root-mean-square current noise. $|\Delta I|$ for MoS_2 and graphene is 4 nA and 2 nA, respectively (see Figure A.4). It's noteworthy that $I_{noise,RMS}$ equals the square root of the integral of the high-frequency current power spectral densities, that is defined as:

$$I_{noise,RMS} = \left(\int_0^{BW} S_I df \right)^{\frac{1}{2}} \tag{A.4.2}$$

where *BW* is the bandwidth and S_I is the power spectral density. The current power spectral density S_I is defined as:

$$S_I = \int_0^{\infty} < I(t).I(0) > \cos(\omega t) dt \qquad \text{(A.4.2)}$$

where *I(t)* is the instantaneous ionic current. Based on our calculation, $I_{noise,RMS}$ for MoS_2 and graphene are 0.2663 nA and 0.602 nA, respectively.

We measured $I_{noise,\,RMS}$ for a range of voltages (0.5 volts – 3.5 volts) and two different temperatures (T=325 K and T=300 K). We found that as temperature increases, $I_{noise,\,RMS}$ increases (Figure A.8). Also, as the bias increases, we observed that $I_{noise,\,RMS}$ decreases (Figure A.8). Although increasing the bias helps reducing the noise in the nanopore, it increases the translocation speed, which can be a challenge in experimental measurements.

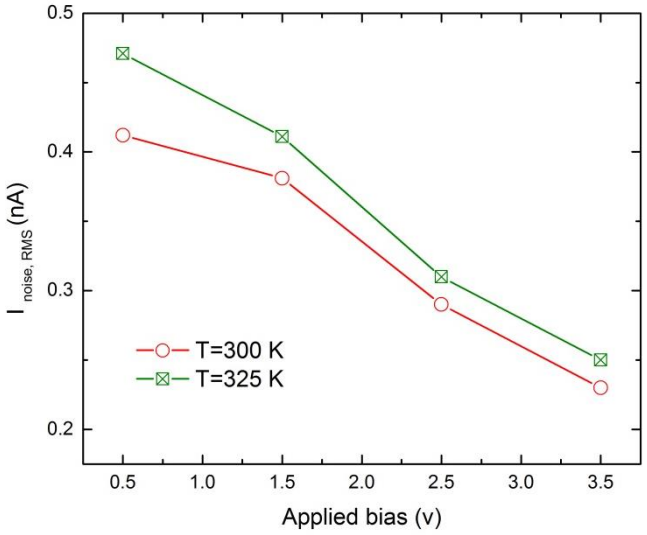

Figure A.8: Root Mean Square (RMS) noise in current for different temperatures and biases.

A.5 Structural and electronic properties of a single-layer MoS_2 and DNA bases

To investigate the sensing mechanism between a single-layer MoS_2 and DNA bases, the fundamental structural and electronic properties are obtained from DFT simulations. First, we constructed an 8x8 unit cell of MoS_2 as shown in Figure A.9.a and Figure A.9.b (each unit cell consists of one Molybdenum (Mo) and two Sulfur (S) atoms). After minimizing the structure, we obtained the bond-length of Mo-S (2.444 Å), S-S (3.193 Å) and lattice constant (a=3.2042 Å), which are in good agreement with previous results.[9, 10] It has been confirmed by several experimental and simulation results that a single-layer MoS_2 has a direct band gap.[9, 11] We computed the electronic band structure (Figure A.9.c) and the total Density of States (DOS) (Figure A.9.d) of a single-layer MoS_2 and determined the direct band gap to be 1.687 eV, which is consistent with previous results.

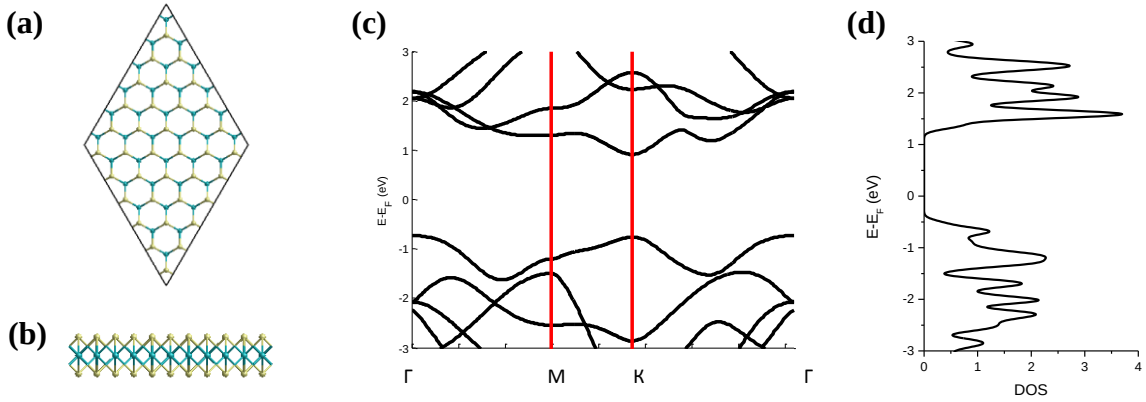

Figure A.9: A single-layer of MoS_2. Structure from (a) top view and (b) side view. (blue ball: Molybdenum, yellow ball: Sulfur) (c) Electronic band structure and (d) Total Density of States (DOS)

The Highest Occupied Molecular Orbital (HOMO) and Lowest Unoccupied Molecular Orbital (LUMO) information for DNA bases are obtained after minimization and the energy gap shows agreement with previous result as shown in Table A.1

Base	HOMO-LUMO gap, (eV)	Previous result [12] , (eV)
A	3.83	3.81
C	3.54	3.52
G	3.89	3.83
T	3.78	3.74

Table A.1: HOMO-LUMO energy gap of DNA bases.

A.6 Edge terminations

We showed in the main text that Mo-only terminated edge exhibits higher response to the nucleobases. Here, we also considered and investigated the sensitivity of the S-only terminated edge. Similar procedures are followed from Mo-only case. Nucleobases are placed horizontally, and after structural minimization, the total DOS is obtained and compared for each base. First, electronic properties of MoS_2 with S-only terminated edge shows finite states around Fermi-level. [13] As shown in Figure A.10, for all DNA bases, the overall curve shape of total DOS is maintained. There is no unique/characteristic response, which means that this type of device setup (S-only terminated edge) is not able to distinguish each base. This is different from Mo-only terminated

edge, which showed distinct change in the response of total DOS for each base as discussed in the main text. The binding energy calculation also confirms that the interaction between S-only terminated edge and each base is weaker than Mo-only case. (Table A.2)

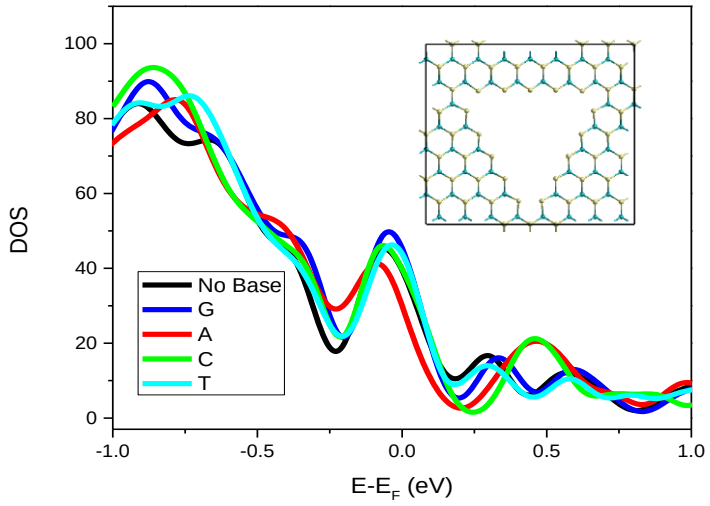

Figure A.10: Total DOS of a single-layer of MoS_2 (nanopore is terminated with S only) interacting with DNA bases. (Inset: Molecular snapshot of S-only terminated edge)

DNA Base	Binding Energy, (eV)
A	1.68
C	1.59
G	2.04
T	1.58

Table A.2: Binding energy between each base and MoS_2 terminated with S-only.

The nanopore configuration in MoS_2 can also be terminated with both Mo- and S-atoms. DNA bases are placed horizontally and each structure is minimized. Similar to the previous two cases, there are induced metallic features (finite states around Fermi level). The total DOS of each structure in Figure A.11.a shows that there is no remarkable change in the response to all bases. To further confirm this result, the edges are terminated with hydrogen. (Figure A.11.b) In this case, an energy gap is partially recovered in the higher energy region, but there is still no clear total DOS difference when the device interacts with DNA bases.

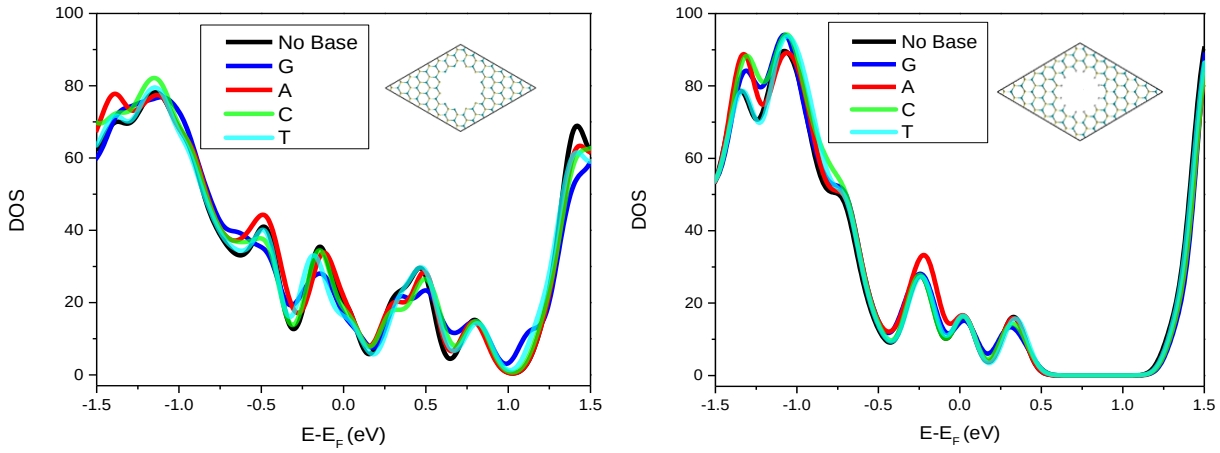

Figure A.11: Total DOS of a single-layer of MoS_2 with nanopore (a) terminated with both Mo- and S-atom and (b) terminated with hydrogen. (Insets: Molecular snapshot of systems)

A.7 Pristine MoS_2 interacting with DNA bases

The system setup of the armchair MoS_2 nanoribbon (AMNR) with each base is shown in Figure A.12. Hydrogen termination is used in the armchair direction. Each Mo and S atom is terminated with two- and one-hydrogen, respectively. After the structure minimization, the total DOS of AMNR is obtained and the band gap is 0.5349 eV (see Figure A.13), which is comparable to the previous result.[14]

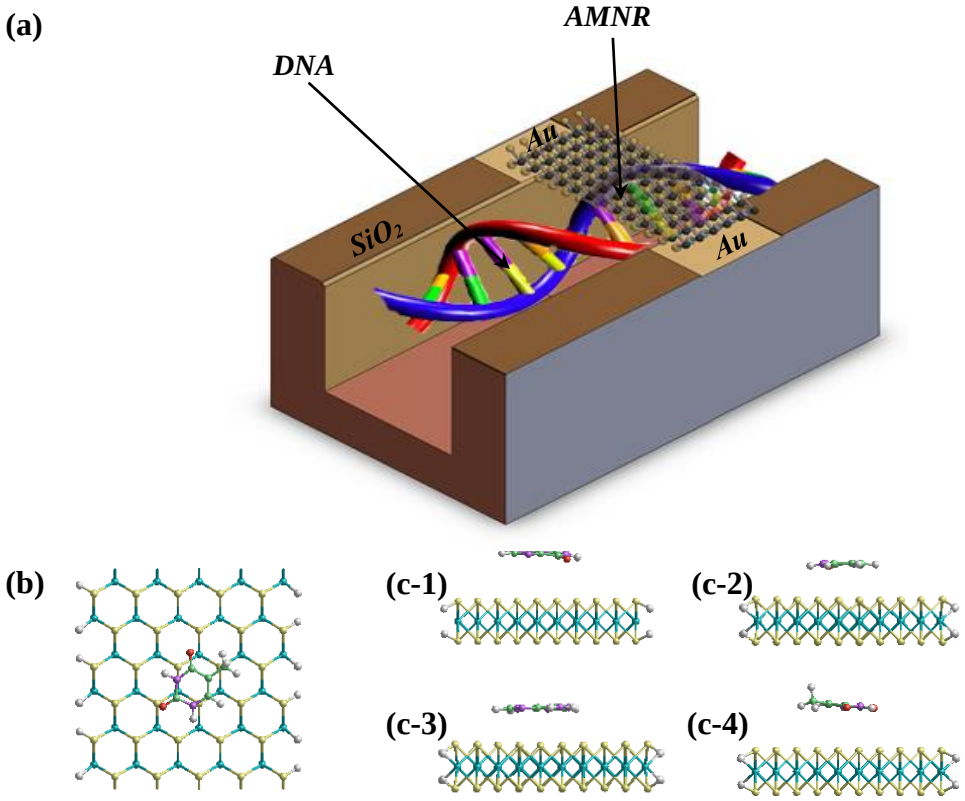

Figure A.12: (a) Schematic device setup for AMNR based DNA sensor. Molecular snapshots of a pristine single-layer MoS_2 (b) and with each DNA base, (c-1) Guanine, (c-2) Thymine, (c-3) Adenine, and (c-4) Cytosine placed on the top.

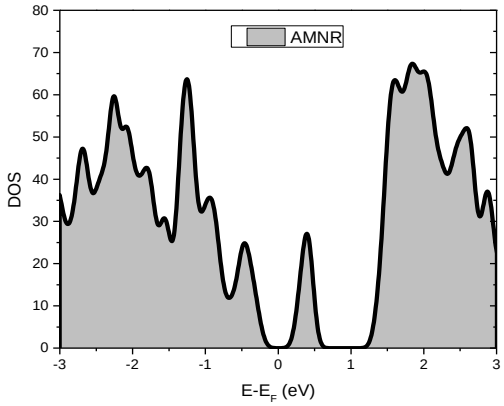

Figure A.13. Total DOS of AMNR

The interaction between a single-layer MoS_2 (bulk) and DNA bases is also investigated to further confirm and support the AMNR results. All the results are found to be similar to those for AMNR case. G nucleobase strongly affects the total DOS of the system, which reduces the band gap by about 0.3 eV. The order of change in energy gap is, G>A>C>T, and the binding energy calculation is consistent with this result (Figure A.14). The overlapping energy states from bases is also observed, which leads to the change in band gap (Figure A.15).

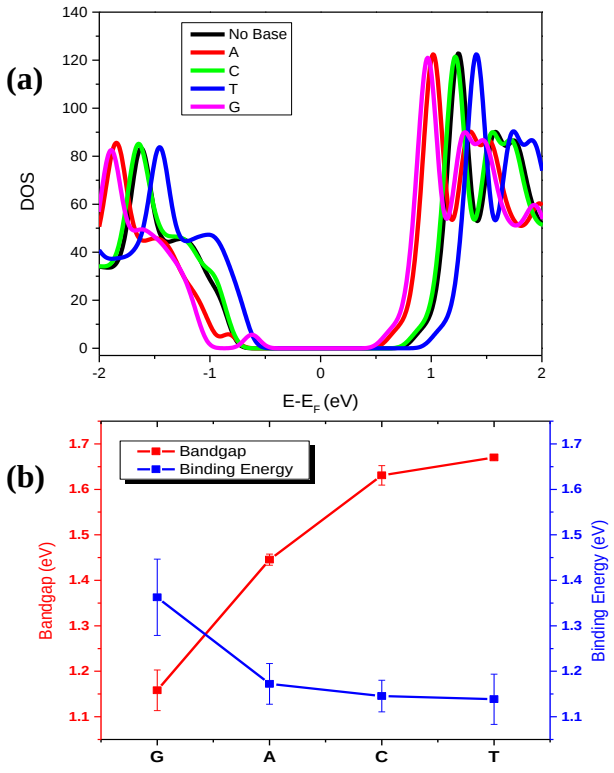

Figure A.14: (a) Total DOS and (b) band gap and binding energy of a pristine single-layer MoS_2 interacting with each DNA base placed on the top.

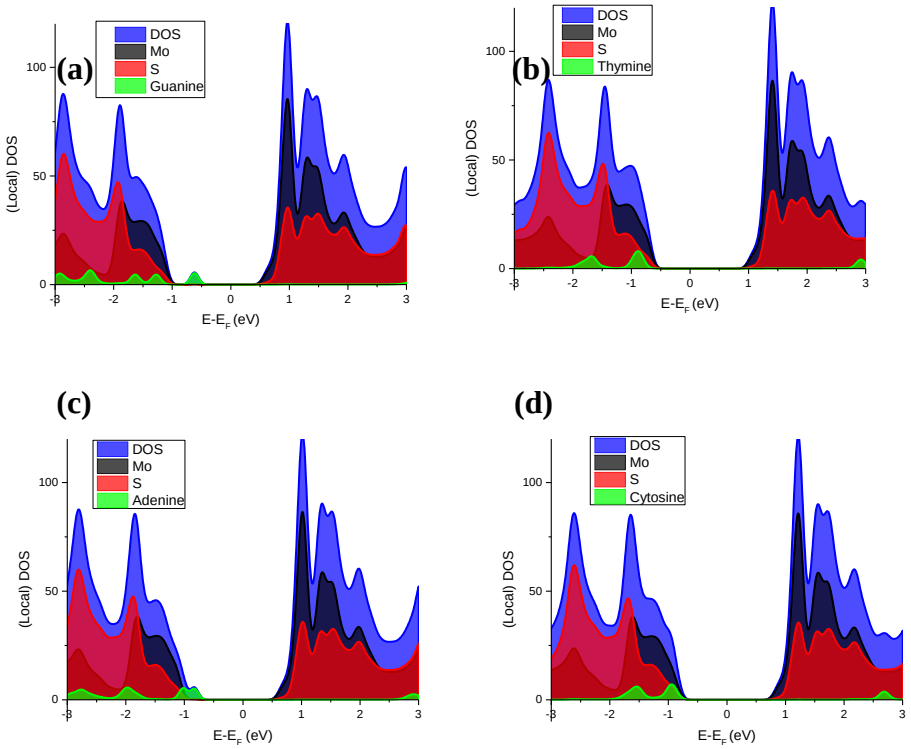

Figure A.15: (a) Total and local DOS of a pristine single-layer MoS_2 with each DNA base (a) Guanine, (b) Thymine, (c) Adenine, (d) Cytosine placed on the top

A.8 The effect of ions and water on interaction between bulk MoS_2 and DNA bases

The effect of water and ions on the electronic properties of bulk MoS_2 with DNA bases is investigated. Two DNA bases, G having the most effect and T having the least effect on MoS_2, are chosen, and water and ions are systematically added. (Table A.3) Adding water on the top of MoS_2 plane slightly reduces the band gap change in the case when no base is placed and when G is placed. When Na^+ and Cl^- ions are added with base G, it shows the largest change in band gap. It is interesting to note that ions have a significant effect in the case of base T.

Base	Water	Na^+, Cl^-	Band gap, (eV)	Difference*	Binding Energy, (eV)
No Base	O	X	1.6875	-0.0001	0.3872
	X	O	1.3262	0.3612	1.2971
	O	O	1.3772	0.3102	2.4213
G	X	X	1.2003	0.4871	1.3623
	O	X	1.2492	0.4382	2.0624
	X	O	0.9917	0.6957	4.9554
	O	O	1.0021	0.6853	5.5802
T	X	X	1.6713	0.0161	1.1388
	O	X	1.6553	0.0321	1.8972
	X	O	1.0031	0.6843	4.5954
	O	O	1.0045	0.6829	4.6233

Table A.3: Band gap and binding energy shift when water and ions are added on the top of bulk MoS_2 interacting with DNA bases. (*Band gap difference is from the bulk MoS_2 band gap, 1.6874 eV) (O: Present, X: Absent)

A.9 Stickiness of the pores

Alternative solutions like using nano-tweezers were suggested to avoid the adherence of DNA to the graphene surface.[15] These solutions may work for ionic current blockade measurements but would complicate the transverse current tunneling because of DNA physisorption.[16, 17] To investigate and compare the adherence of the bases to the surface of MoS_2 and graphene, we simulated DNA translocation events in MoS_2 and graphene with an applied bias of 2.8 volts (using MD). Both graphene and MoS_2 nanopore approximately have the pore size of 2.3 nm. Figure A.16.a and Figure A.16.b show the adherence of bases to the graphene surface and the non-stickiness behavior of the MoS_2 nanopore. To quantify the adherence of the bases for graphene and MoS_2, we counted the DNA atoms in a disc (virtual geometrical space) with a thickness of 1

nm, the internal hole diameter of 2.3 nm and concentric with the graphene and MoS_2 pores. We positioned the hollow disc on the top of the pores. The outer diameter of the hollow disc is selected to be 8 nm. Using this, the number of adhered atoms of DNA to the pore surface for both MoS_2 and graphene is shown in Figure A.16. 14-18 atoms are constantly adsorbed to the surface of graphene while 3-5 atoms are stuck on the surface of MoS_2. The calculation of DNA center of mass (COM) with respect to the pore axis for graphene and MoS_2 reveals that dsDNA COM has an offset of 1.28 nm from the central pore axis in the graphene nanopore. The COM offset is only 0.33 nm for the case of MoS_2 nanopore. The larger offset can be attributed to the stickiness of the graphene nanopore that holds DNA on the surface. Eccentricity of DNA COM from the pore central axis increases the noise in the pore to a large extent.[18]

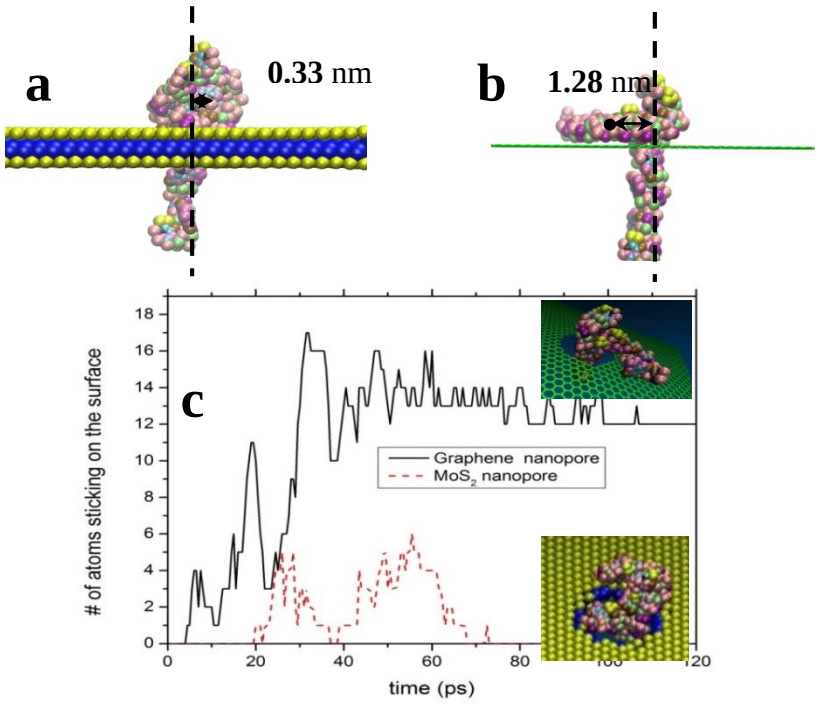

Figure A.16: (a) Translocation of DNA through a MoS_2 nanopore and non-stickiness of MoS_2 surface, dsDNA COM offset is shown. (b) Translocation of DNA through graphene nanopore and adherence of bases to the surface of graphene, dsDNA COM offset is shown. (c) Comparison of stickiness of the MoS_2 and graphene nanopore. Each graph shows the number of atoms sticking to the surface of graphene/MoS_2 as DNA translocates through the pore

.

A.10 References

1. Wells, D. B.; Belkin, M.; Comer, J.; Aksimentiev, A. Assessing Graphene Nanopores for Sequencing DNA. *Nano Lett.* 2012, 12, 4117-4123.
2. Siwy, Z. S.; Davenport, M. Nanopores Graphene Opens up to DNA. *Nat. Nanotechnol.* 2010, 5, 697-698.
3. Branton, D.; Deamer, D. W.; Marziali, A.; Bayley, H.; Benner, S. A.; Butler, T.; Di Ventra, M.; Garaj, S.; Hibbs, A.; Huang, X. H.; Jovanovich, S. B.; Krstic, P. S.; Lindsay, S.; Ling, X. S. S.; Mastrangelo, C. H.; Meller, A.; Oliver, J. S.; Pershin, Y. V.; Ramsey, J. M.; Riehn, R.; Soni, G. V.; Tabard-Cossa, V.; Wanunu, M.; Wiggin, M.; Schloss, J. A. The Potential and Challenges of Nanopore Sequencing. *Nat. Biotechnol.* 2008, 26, 1146-1153.
4. Aksimentiev, A. Deciphering Ionic Current Signatures of DNA Transport through a Nanopore. *Nanoscale* 2010, 2, 468-483.
5. Cracknell, J. A.; Japrung, D.; Bayley, H. Translocating Kilobase Rna through the Staphylococcal Alpha-Hemolysin Nanopore. *Nano Lett.* 2013, 13, 2500-2505.
6. vanDongen, M. J. P.; Mooren, M. M. W.; Willems, E. F. A.; vanderMarel, G. A.; vanBoom, J. H.; Wijmenga, S. S.; Hilbers, C. W. Structural Features of the DNA Hairpin D(Atccta-Gtta-Taggat): Formation of a G-a Base Pair in the Loop. *Nucleic Acids Res.* 1997, 25, 1537-1547.
7. Li, J. P.; Zhang, Y.; Yang, J. K.; Bi, K. D.; Ni, Z. H.; Li, D. Y.; Chen, Y. F. Molecular Dynamics Study of DNA Translocation through Graphene Nanopores. *Phys. Rev. E* 2013, 87.
8. Smeets, R. M. M.; Keyser, U. F.; Dekker, N. H.; Dekker, C. Noise in Solid-State Nanopores. *Proc. Natl. Acad. Sci. U. S. A.* 2008, 105, 417-421.
9. Ataca, C.; Sahin, H.; Akturk, E.; Ciraci, S. Mechanical and Electronic Properties of MoS_2 Nanoribbons and Their Defects. *The Journal of Physical Chemistry C* 2011, 115, 3934-3941.
10. Li, Y.; Zhou, Z.; Zhang, S.; Chen, Z. MoS_2 Nanoribbons: High Stability and Unusual Electronic and Magnetic Properties. *J. Am. Chem. Soc.* 2008, 130, 16739-16744.
11. Radisavljevic, B.; Radenovic, A.; Brivio, J.; Giacometti, V.; Kis, A. Single-Layer MoS_2 Transistors. *Nat. Nanotechnol.* 2011, 6, 147-150.
12. Kilina, S.; Tretiak, S.; Yarotski, D. A.; Zhu, J.-X.; Modine, N.; Taylor, A.; Balatsky, A. V. Electronic Properties of DNA Base Molecules Adsorbed on a Metallic Surface. *The Journal of Physical Chemistry C* 2007, 111, 14541-14551.
13. Zhou, Y.; Yang, P.; Zu, H.; Gao, F.; Zu, X. Electronic Structures and Magnetic Properties of Mos2 Nanostructures: Atomic Defect, Nanohole, Nanodot and Antidot. *Phys. Chem. Chem. Phys.* 2013.
14. Dolui, K.; Pemmaraju, C. D.; Sanvito, S. Electric Field Effects on Armchair MoS_2 Nanoribbons. *ACS Nano* 2012, 6, 4823-4834.
15. Sathe, C.; Zou, X. Q.; Leburton, J. P.; Schulten, K. Computational Investigation of DNA Detection Using Graphene Nanopores. *ACS Nano* 2011, 5, 8842-8851.
16. Lee, J.-H.; Choi, Y.-K.; Kim, H.-J.; Scheicher, R. H.; Cho, J. H. Physisorption of DNA Nucleobases on H-BN and Graphene: Vdw-Corrected DFT Calculations. *The Journal of Physical Chemistry C* 2013.
17. Le, D.; Kara, A.; Schröder, E.; Hyldgaard, P.; Rahman, T. S. Physisorption of Nucleobases on Graphene: A Comparative Van Der Waals Study. *Journal of Physics: Condensed Matter* 2012, 24, 424210.
18. Lu, B.; Albertorio, F.; Hoogerheide, D. P.; Golovchenko, J. A. Origins and Consequences of Velocity Fluctuations During DNA Passage through a Nanopore. *Biophys. J.* 2011, 101, 70-79.

APPENDIX B

B.1 Molecular structure of DNA bases

The molecular representations of DNA nucleotides (A, C, G and T) are illustrated in Figure B1. The interaction of each nucleotide with the MscL pore depends on the structure and type of the atoms of each base. These interactions involve both VdW and Coulombic forces which are parameterized by the Lennard-Jones parameters (σ and ε) and the partial charges on each atom (tabulated in Table B.1 and Table B.2). The Lennard-Jones interaction energy is highest for oxygen atoms (ε_O=0.210), therefore, bases containing these protruding oxygen atoms exhibit stronger VdW interactions with the atoms of the pore. As shown in Figure B.1, base T has two oxygen atoms while base A does not contain any oxygen atoms which are consistent with the interaction forces in chapter 3. The other Lennard-Jones parameter σ, which is representative of the size of an atom, plays an important role in the ionic current blockade.

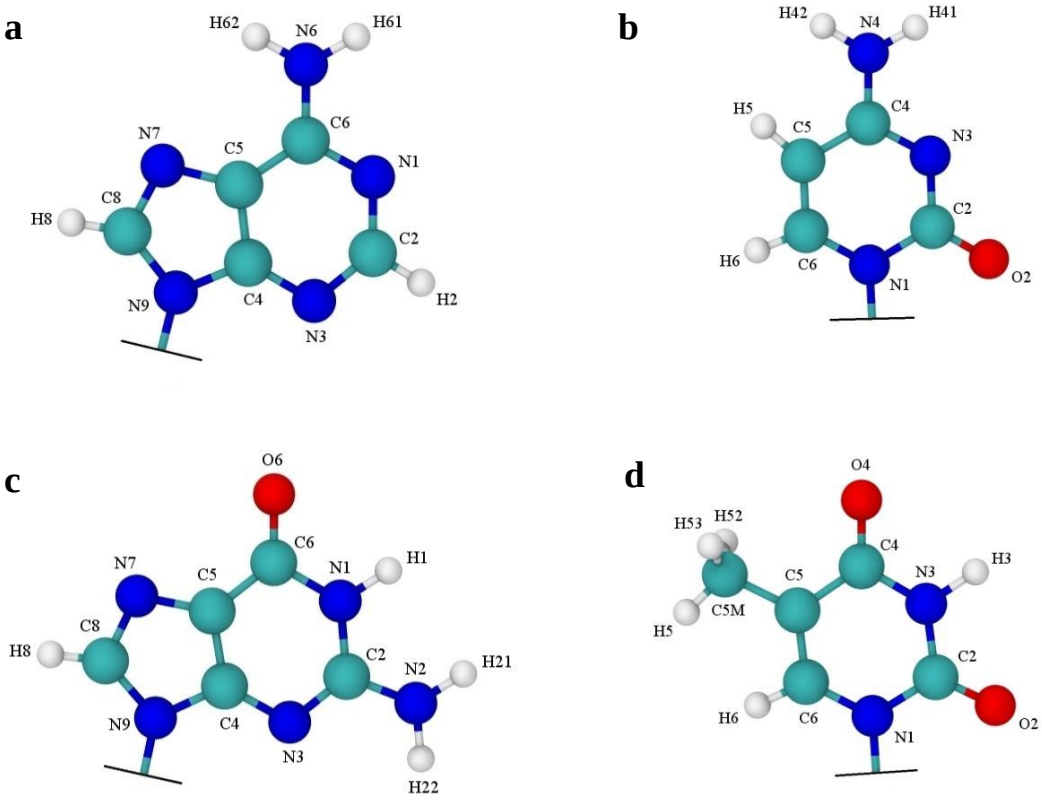

Figure B.1. Representation of DNA bases with their atom types (white: hydrogen atoms, blue: nitrogen atoms, cyan: carbon atoms and red: oxygen atoms). **a|** Base A. **b|** Base C. **c|** Base G. **d|** Base T.

Atom	σ (Å)	ε (kcal/mol)
O	2.96	0.210
N	3.25	0.170
C in C=O	3.75	0.105
All C (not in C=O)	3.50	0.080
H bonded to N	0.00	0.000
H Bonded to C	2.50	0.050

Table B.1 Lennard-Jones parameters for atoms of bases.

Base A atom	Charge (e)	Base C atom	Charge (e)	Base G atom	Charge (e)	Base T atom	Charge (e)
N1	-0.6710	N1	-0.8420	N1	-0.6710	N1	-0.8680
C2	0.3434	C2	0.9470	H1	0.4050	C2	1.0340
H2	0.1610	O2	-0.6190	C2	0.9748	O2	-0.6040
N3	-0.6360	N3	-0.721	N2	-0.9560	N3	-0.1850
C4	0.6380	C4	0.6740	H21	0.3990	H3	0.4250
C5	0.0860	N4	-0.9240	H22	0.4170	C4	0.8270
C6	0.6510	H41	0.3940	N3	-0.7200	O4	-0.5880
N6	-0.7800	H42	0.4110	C4	0.6480	C5	-0.185
H61	0.3280	C5	-0.3830	C5	-0.0290	C5M	-0.1100
H62	0.3370	H5	0.2160	C6	0.8300	H5	0.0700
N7	-0.5877	C6	0.1950	O6	-0.5950	H52	0.0700
C8	0.3510	H6	0.2400	N7	0.5090	H53	0.0700
H8	0.1820			C8	0.2730	C6	0.1500
N9	-0.7430			H8	0.2220	H6	0.2400
				N9	-0.8240		

Table B.2 Partial charges on atoms of DNA bases.[2]

B.2 Ionic current in MspA and MscL

To understand the effect of pore elasticity on the ionic current signals we acquired in MscL, we compared the ionic current signals obtained from translocation of ssDNAs in MspA and MscL pores (Figure B.2). In the main text, we already computed the time averaged ionic current for 4 different nucleotides in MscL. Here, using the same simulation approach already explained in the Methods section of the main manuscript, we simulated the translocation of 4 ssDNA (PolydA(60), PolydT(60), PolydG(60) and PolydC(60)) through MspA. The only difference between MscL and MspA simulations is the type of protein. For MspA, we used the crystallography data with the PDB code:1UUN. The snapshots of the initial simulation of PolydA through MspA and MscL are shown in Figure B.2.

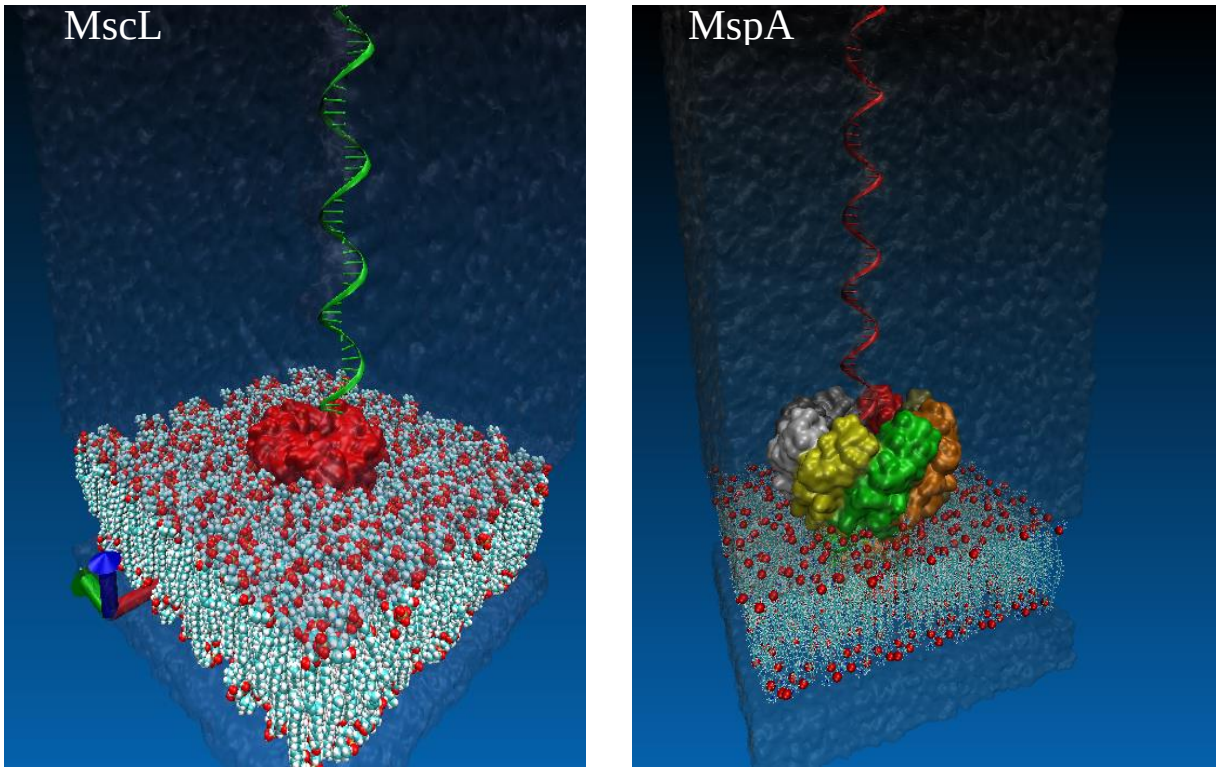

Figure B.2. Snapshots of simulation set up Left) MscL and Right) MspA.

The transmembrane bias of 0.5 V is applied in all cases. The average ionic current for bases A, C, G, and T through MspA and MscL are shown in Figure S3. The level of currents for MspA is lower than the one in MscL. Also the order of currents for 4 bases is different in the two pores.

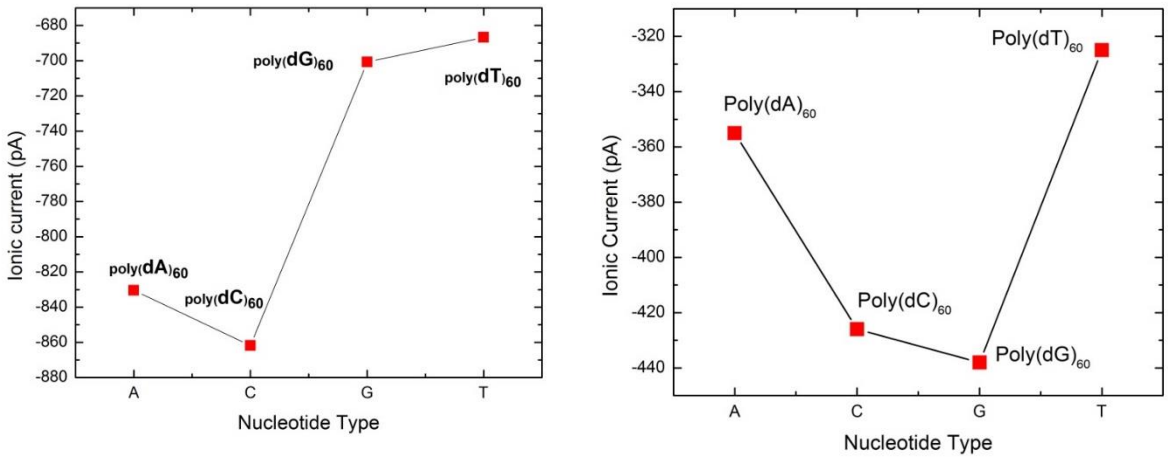

Figure B.3. Averaged ionic current for Poly(dA)$_{60}$, Poly(dC)$_{60}$, Poly(dT)$_{60}$ and Poly(dG)$_{60}$ for Left) MscL and Right) MspA

The maximum and minimum current difference, ΔI, is 113.1 pA and 189.2 pA for MspA and MscL, respectively. The signal strength is higher for MscL compared to MspA.

B.3 Signal to Noise (SNR) calculation

SNR is defined as[1]

$$SNR = \frac{|\Delta I|}{I_{noise,RMS}} \tag{B.3.1}$$

where $|\Delta I|$ is the absolute current change due to protein translocation and $I_{noise,RMS}$ is the root-mean-square current noise. It is noteworthy that $I_{noise,RMS}$ equals the square root of the integral of the high-frequency current power spectral densities, which is defined as:

$$I_{noise,RMS} = \left(\int_0^{BW} S_I df \right)^{\frac{1}{2}} \tag{B.3.2}$$

where BW is the bandwidth and S_I is the power spectral density. The current power spectral density (S_I) is defined as:

$$S_I = \int_0^{\infty} < I(t) \cdot I(0) > \cos(\omega t) dt \tag{B.3.3}$$

where $I(t)$ is the instantaneous ionic current.

References

1. Dekker, C. Solid-State Nanopores. *Nat. Nanotechnol.* 2007, 2, 209-215.

2. MacKerell, A. D.; Banavali, N. K. All-Atom Empirical Force Field for Nucleic Acids: Application to Molecular Dynamics Simulations of DNA and Rna in Solution. *J. Comput. Chem.* 2000, 21, 105-120.

APPENDIX C

C.1 Calculations of conductivity

Conductivity of our systems has been calculated by taking advantage of the electrical scheme depicted in the Figure C.1. Since in all of our studies, an external electric field is applied in z direction, wherever in this text we mention resistance or conductance, it means resistance or conductance in z direction.

In each system, the resistance of the solution is connected to the resistance of the nanopore in series; therefore, the total resistance can be calculated as

$$R_t = R_s + R_n \tag{C.1.1}$$

Where R_s is the resistance of the solution and R_n is the resistance of the nanopore. The solution resistance is computed as

$$R_S = \sigma \frac{L_z}{A_{xy}} \tag{C.1.2}$$

Where σ stands for resistivity of buffer, L_z is the length of the system in z direction and A_{xy} is the area of the water box in xy −plane. In order to estimate the bulk resistivity σ, we performed five ionic current simulations with biases of 0.25 v, 0.5 v, 0.75 v, 1 v and 2 v for a 10.9 nm × 11.9 nm × 10.0 nm 1M NaCl solution cell. Figure C.2 illustrates the currents versus applied biases for these simulations. Then we could calculate bulk resistivity as

$$\sigma = r \frac{A_{xy}}{L_z} \tag{C.1.2}$$

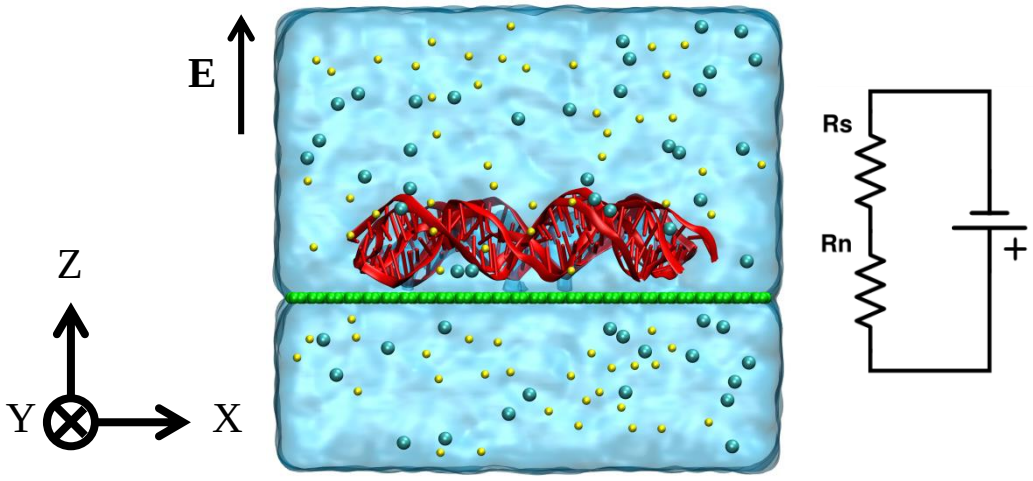

Figure C.1: Simulation system of 1 layer DNA origami-graphene hybrid nanopore under an external electric field applied toward z direction. The equivalent electrical circuit consists of two resistor connected in series. In this case, R_s and R_n represent the resistivity of the solution and the 1 layer DNA origami-graphene hybrid nanopore respectively. Resistivity of the nanopore R_n depends on the simulation case, which may be made up with the resistivity of 0/1/2 layer(s) of DNA origami nanoplate and/or the resistivity of the graphene sheet.

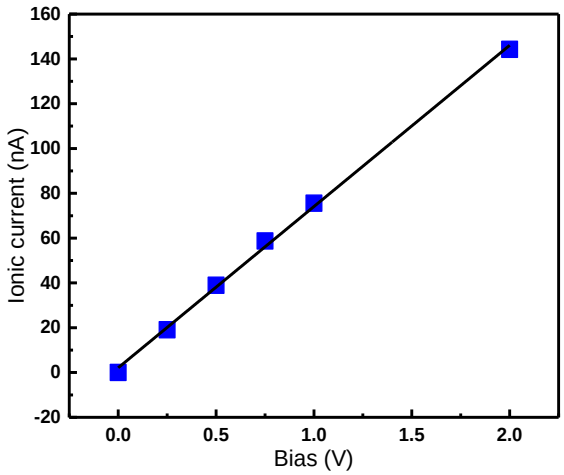

Figure C.2: *I-V* curves generated from ionic current simulations on a 1M NaCl solution cell.

Where *r* is the inverse slope of the *I-V* curve corresponding to the simulated cell (Figure C.2), A_{xy} and L_z are the area of the cell in *xy*-plane and its length toward z direction respectively. The resistivity of buffer is computed to be $\sigma = 5.6\frac{\Omega}{m}$ using $r = 71.98\, n\Omega$, $A_{xy} = 129.71\, nm^2$ and $L_z = 10.0\, nm$. Since the dimensions of the simulated cell and the solution box are the same, we obtain $R_s = r = 71.98\, n\Omega$.

The resistance of the nanopore in each case depends on the number of the layers of DNA origami nanoplate used in the structure. It should be noted that in all of our cases, the resistor of the component(s) of the nanopore are connected in series. So, the most resistive structure is Double layer DNA origami-graphene nanopore that its resistance can be calculated as:

$$R_t = 2R_d + R_g + R_s \tag{C.1.2}$$

Where R_d is the resistance of one layer DNA origami nanopore (just accounts for the effect of the middle pore and not the gaps and holes between the DNA strands), R_g is the resistance of the graphene nanopore and R_s is the solution resistivity. Here, we simply consider R_t as the inverse slope of the *IV* curve of the corresponding simulation, which is modeled by the slope of the linear fit onto corresponding simulation data. Then, conductivity G is defined as the inverse of the resistance

$$G = \frac{1}{R} \tag{C.1.2}$$

Table C.1 shows the calculated conductance for different cases.

Nanopore	**Conductance (ns)**
2Layer DNA origami + Graphene	1.516
1Layer DNA origami + Graphene	2.457
1Layer DNA origami	2.526
Graphene	6.497

Table C.1: The conductance of nanopores obtained using the mathematical model.

C.2 DNA origami design

Because of some restrictions in converting caDNAno files to NAMD input files, we made two additional break points in the scaffold strand of the DNA origami nanoplate. These additional break points used to sequence the plate in a way to have more T bases in the scaffold strand at the location of the pore. The DNA origami pore was created by eliminating some A bases of staple strands at the middle of the nanoplate. The additional break points were filled again to have a single scaffold strand after the pore was created. Figure C.3 illustrates the connectivity map of the DNA origami nanoplate used in our simulations.

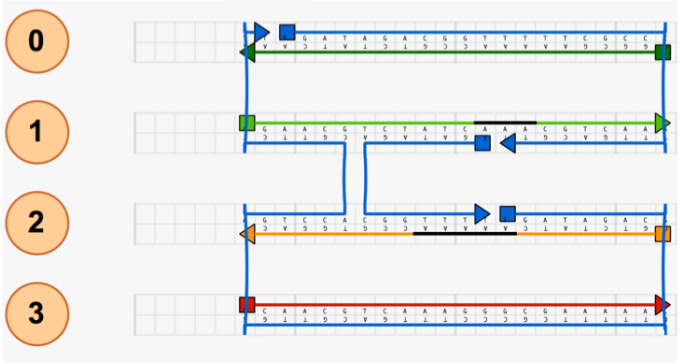

Figure C.3| Connectivity map of the DNA origami nanoplate. The additional break points at the middle of the nanoplate were just generated to increase the number of T bases in the scaffold strand at the location of the pore. These break points were filled up again to have a single scaffold strand before starting the simulations.

C.3 DNA origami bases around the nanopore

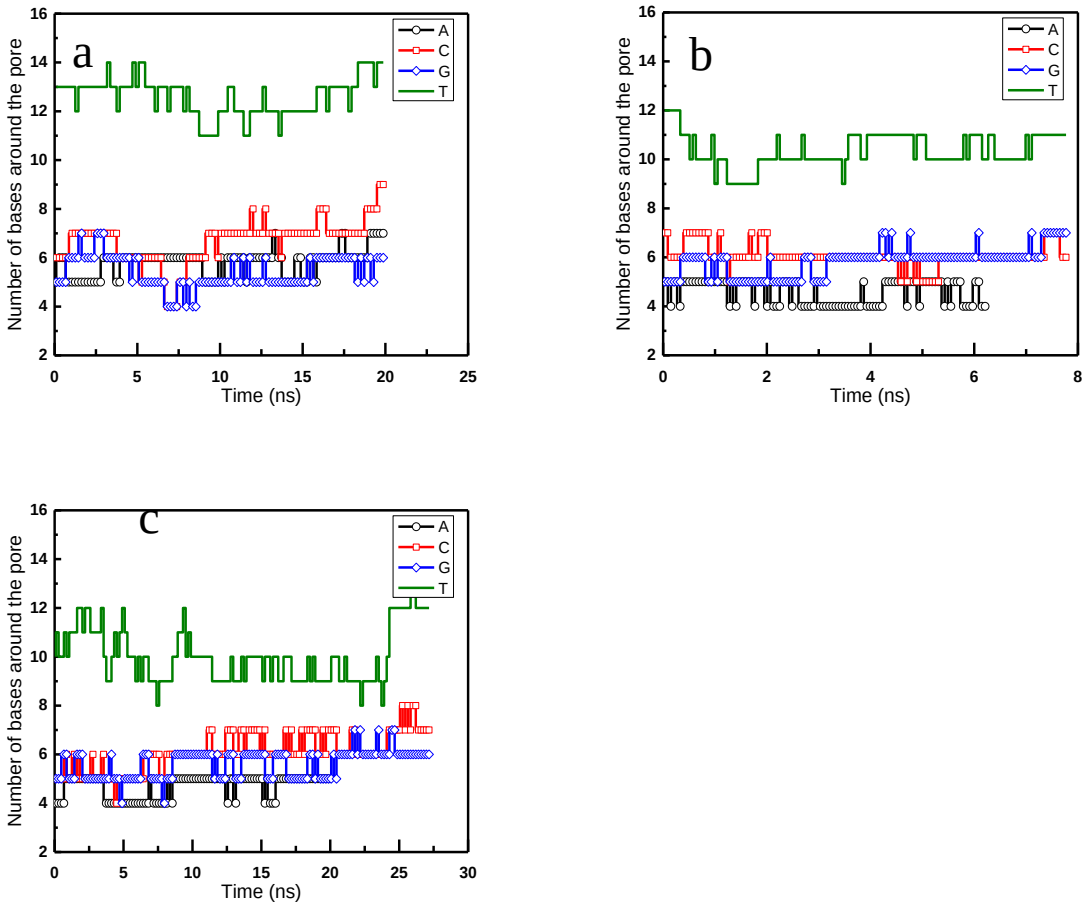

Figure C.4 Number of different base types in a ring with the radius of 22.4 Å centered with the pore for the translocation of (a) Poly(dC)$_{20}$ ssDNA (b) Poly(dG)$_{20}$ ssDNA (c) Poly(dT)$_{20}$ ssDNA. In all simulation, number of A bases residing beside the pore is greater than the other base types. Moreover, the small amplitude fluctuations of the number of bases indicate that all bases of ssDNA's observe the same environment during the simulation time.

APPENDIX D

D.1 Translocation of different proteins

We translocated 4 different protein types: Titin, Myoglobin, Ubiquitin and MTHK (Methanobacterium thermoautrophicum K^+). A graphene nanopore (GNP) with diameter of 5 nm is used for the translocation of these 4 proteins. Titin is a very large protein (with the diameter of 3.1 nm and the length of 8.1 nm) in muscles which dampens biological forces at the molecular level,[1] such as during extension of a muscle fiber under stress. We translocated Titin (PDB code: 1YA5)[1] through GNP to analyze the time-dependent ionic current (Figure D.1). The time-dependent ionic current plot shows a blockade time of 8 ns (Figure D.2). At t=10 ns, the blockade is full (I=0 nA) suggesting that the pore is largely occupied by the large diameter Titin.

Next, we translocated Myoglobin protein through GNP (Figure D.3). Myoglobin is a small (with diameter of ~3.5 nm), monomeric protein that functions as an intracellular oxygen storage site.[2] It is found in abundance in the skeletal muscle of vertebrates, and is responsible for the red color of muscle tissue. Myoglobin is closely related to hemoglobin, which consists of four myoglobin-like subunits that form a tetramer, and is responsible for carrying oxygen in blood. In humans, blood-borne cardiac myoglobin can serve as a biomarker of heart attack.[2]

We translocated Myoglobin (PDB code: 1MBC)[2] through GNP. Ionic current fluctuations for Myoglobin translocation reveal that the blockade time is τ_b=5 ns and the average current associated with translocation is 2 nA (Figure D.4).

The third protein we translocated was Ubiquitin. Ubiquitin is a small (with the diameter of 2.3 nm, 8.5 kDa) regulatory protein that has been found in almost all tissues (ubiquitously) of eukaryotic organisms.[3] We can use structures resulting from x-ray crystallography to examine ubiquitin in more detail. The best

crystallography resolution data available for Ubiquitin structure (PDB code: 1UBQ)[3] is at 1.8 Å. Its compact structure becomes evident as seen in Figure D.5. The average ionic current is 2.23 nA and the blockade time is τ_b=2 ns (Figure D.6)

The other protein we targeted was MTHK (Figure D.7). MTHK is a transmembrane K+ channel which is activated with Ca^{++}.[4] The ionic current plot associated with MTHK translocation is presented in Figure D.8. The average ionic current is 1.1 nA and the blockade time is τ_b=3 ns.

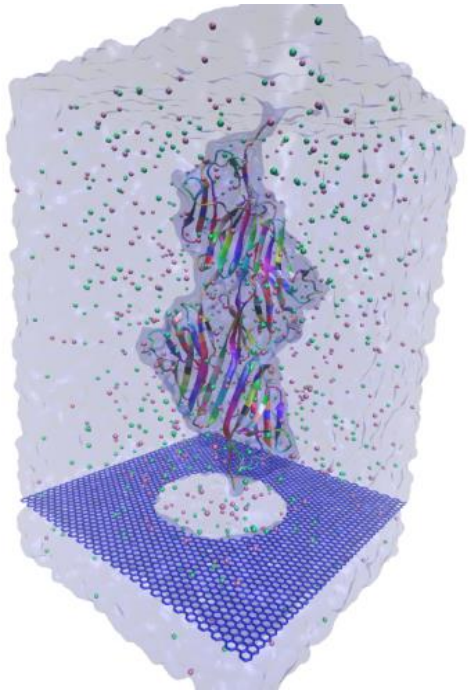

Figure D.1: Titin translocation through GNP with water and ions.

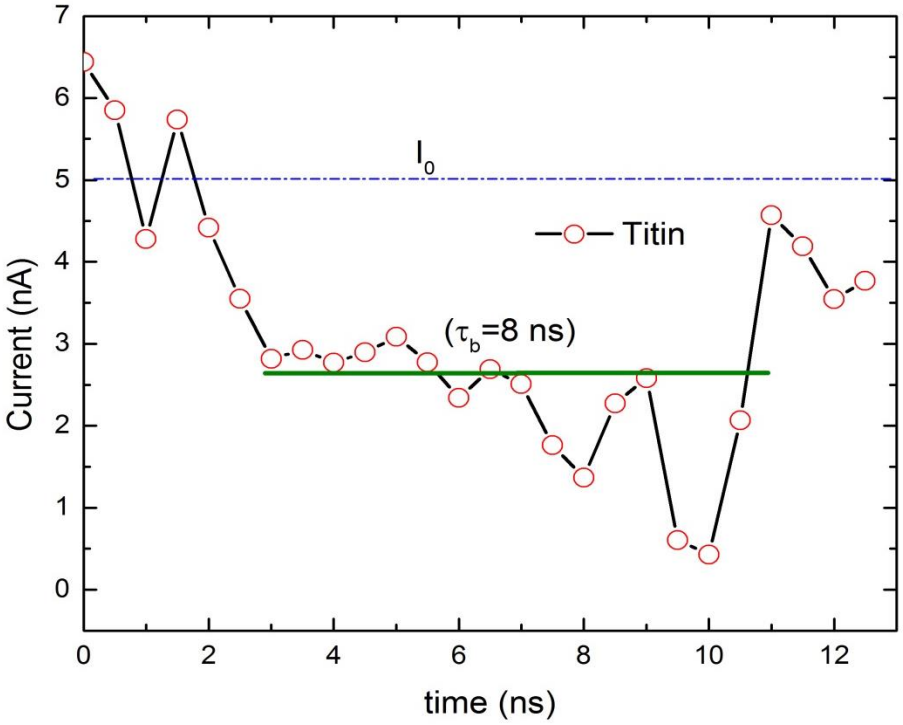

Figure D.2: Time-dependent ionic current and blockade time for Titin translocation through GNP.

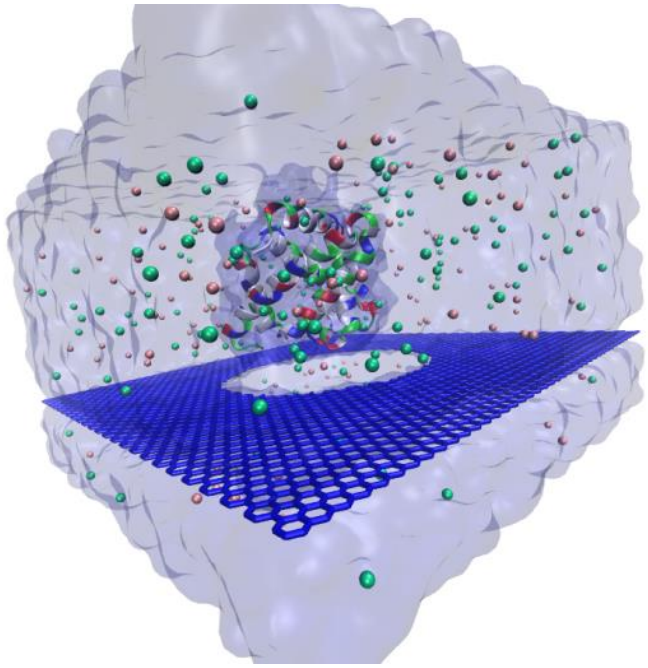

Figure D.3: Myoglobin translocation through GNP with water and ions.

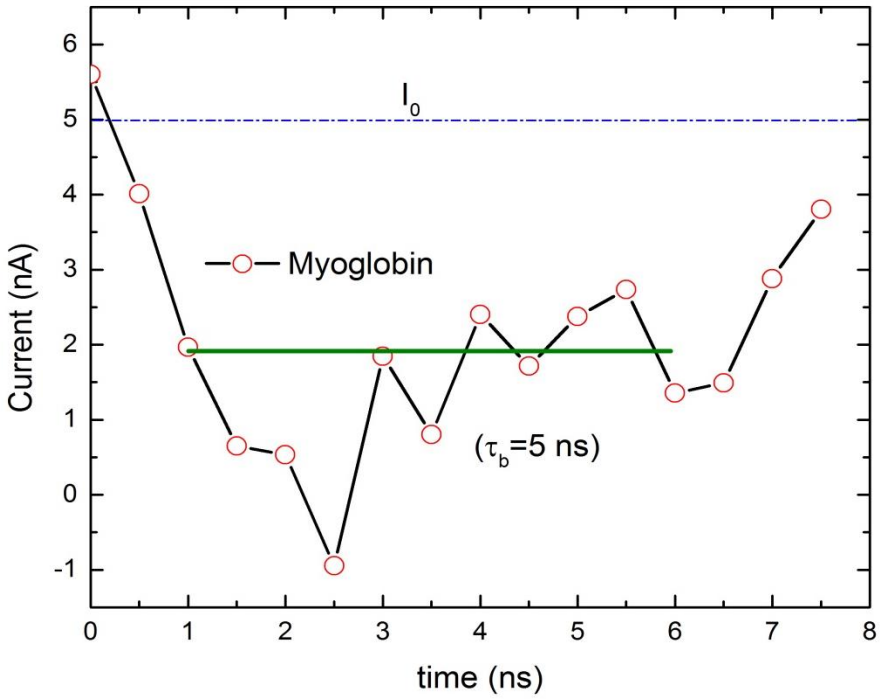

Figure D.4: Time-dependent ionic current and blockade time for Myoglobin translocation through graphene nanopore.

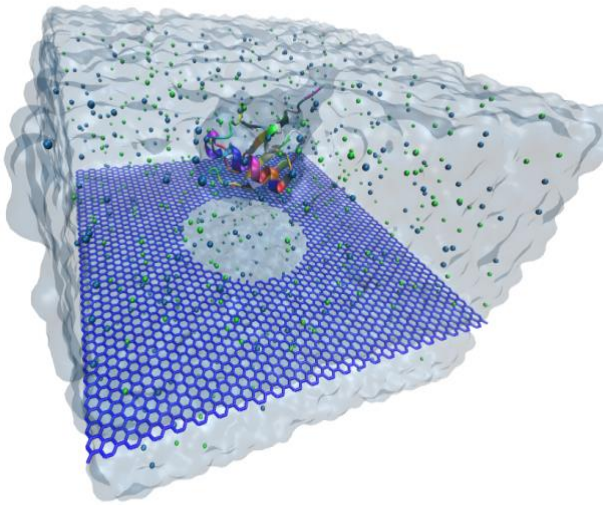

Figure D.5: Ubiquitin translocation through GNP with water and ions

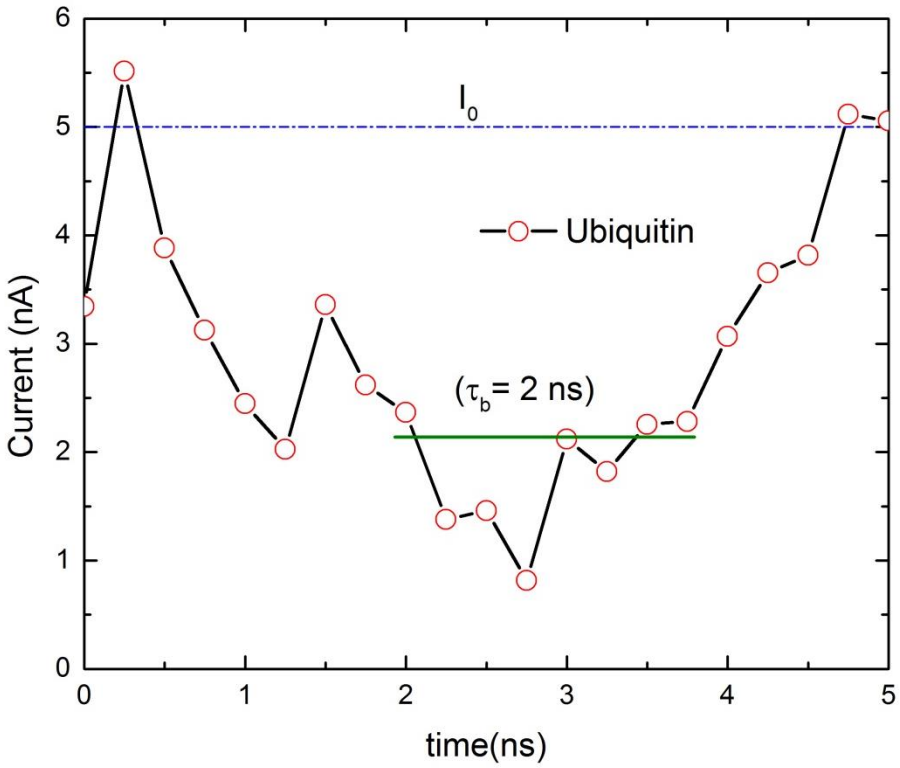

Figure D.6: Time-dependent ionic current and blockade time for Ubiquitin translocation through GNP.

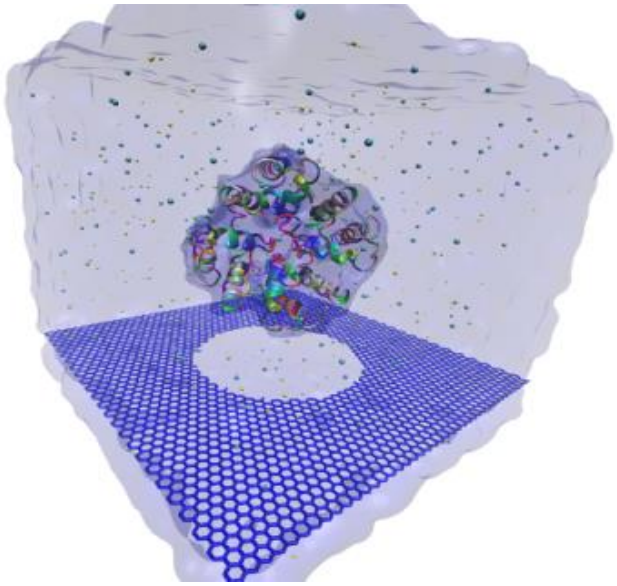

Figure D.7: MTHK (transmembrane channel) translocation through GNP with water and ions.

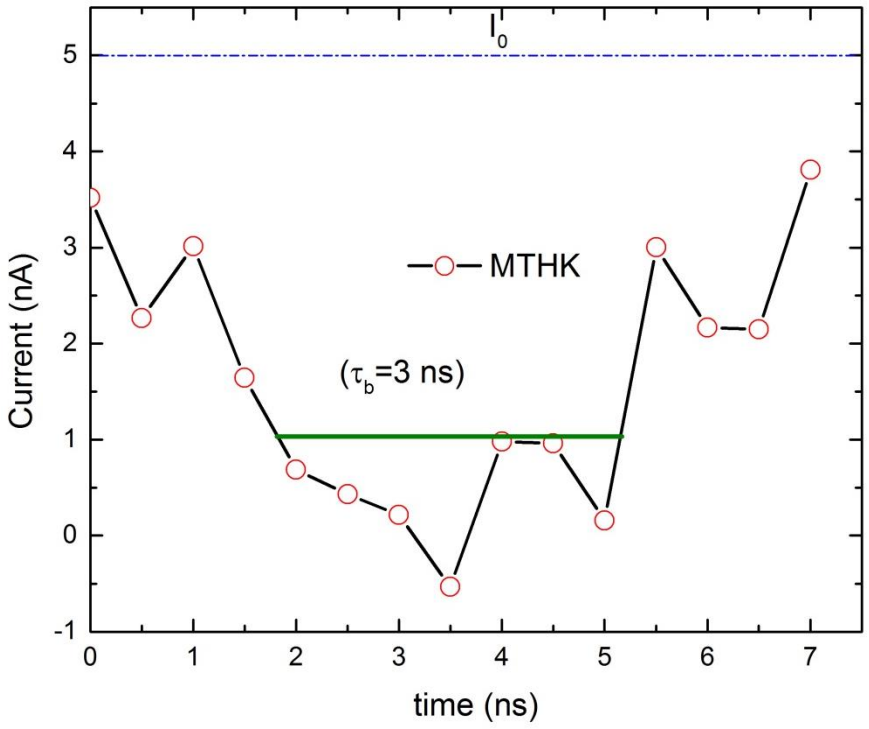

Figure D.8: Time-dependent ionic current and blockade time for Ubiquitin translocation through GNP.

D.2 Stretching and conformational changes of IgGs

During IgGs translocation process, IgGs undergo various conformational changes. One of these conformational changes is the stretching and elongation of Fabs. The elongation occurs due to the interaction of graphene with Fabs. IgG2 Fabs are more stretched compared to IgG3 (Figure D.9). The Fabs elongation starting point is delayed in IgG3 compared to IgG2 which can be attributed to the longer hinge region of IgG3.

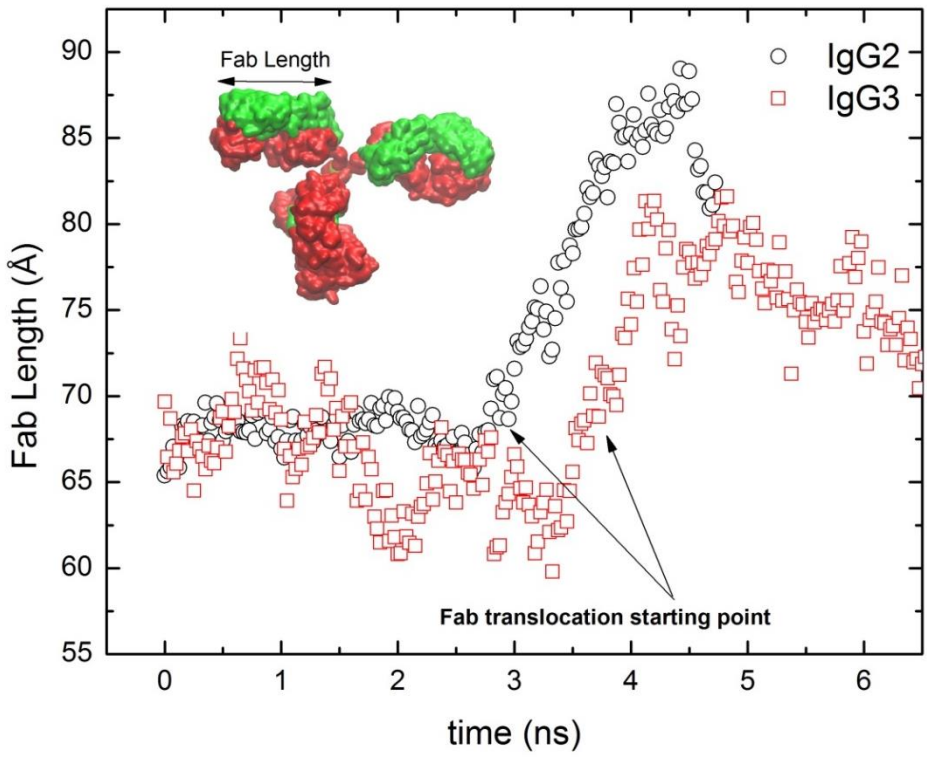

Figure D.9: Fab length changes during translocations of IgG2 and IgG3.

D.3 Signal to Noise (SNR) calculation

The SNR is defined as[5]

$$SNR = \frac{|\Delta I|}{I_{noise,RMS}} \tag{D.3.1}$$

where $|\Delta I|$ is the absolute current change due to protein translocation and $I_{noise,RMS}$ is the root-mean-square current noise. It is noteworthy that $I_{noise,RMS}$ equals the square root of the integral of the high-frequency current power spectral density, which is defined as:

$$I_{noise,RMS} = \left(\int_0^{BW} S_I df \right)^{\frac{1}{2}} \tag{D.3.2}$$

where BW is the bandwidth and S_I is the power spectral density. The current power spectral density (S_I) is defined as:

$$S_I = \int_0^{\infty} < I(t) \cdot I(0) > \cos(\omega t) dt \tag{D.3.3}$$

where $I(t)$ is the instantaneous ionic current.

D.4 History of IgG2 translocation through graphene nanopore

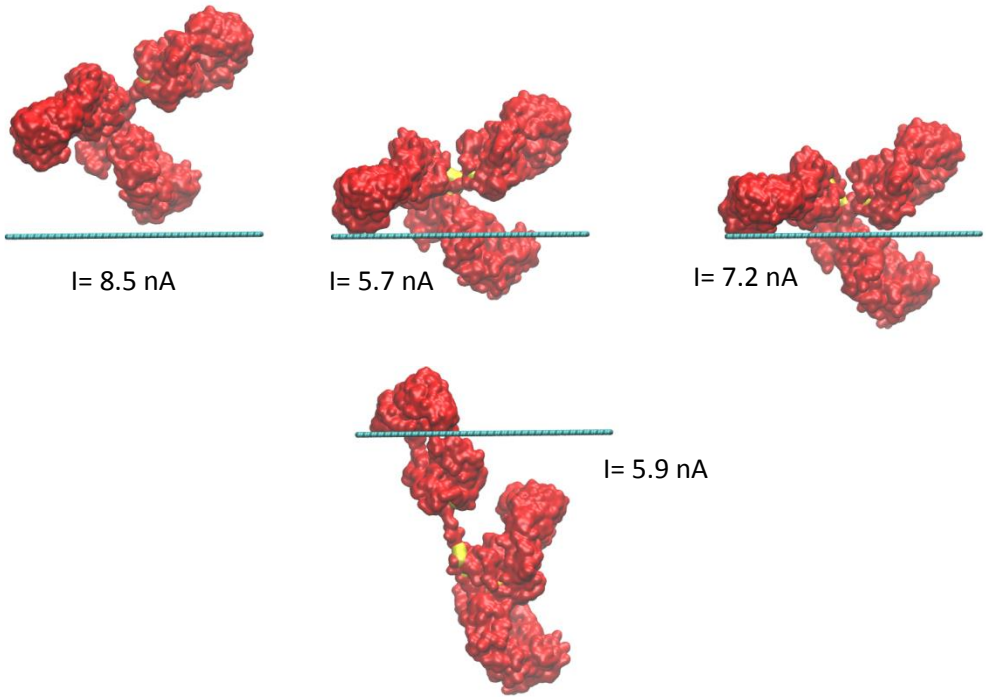

Figure D.10: Snapshots of IgG2 translocation and the current associated with the snapshot.

D.5 Silicon Nitride nanopore simulation setup

As mentioned in the main article, a thick silicon nitride pore (Si_3N_4) of the same diameter (10 nm) as graphene nanopore's diameter is used to compare with the one-atom-thick graphene nanopore. The thickness of the silicon nitride membrane is taken to be 10 nm. The Inorganic Builder plugin in VMD[6] was used to create a hexagonal structure of the membrane which is computationally more efficient than a square structure due to its reduced number of atoms. To drill a conical pore in the solid state silicon nitride, the method proposed by J. R. Comer *et al.*[7] was employed where the atoms were removed based on the following criterion:

$$\sqrt{x^2 + y^2} < \frac{D_\circ}{2} + |z| tan(\beta) \qquad \text{(D.5.1)}$$

where x, y and z are the coordinates of an atom, $D_\circ$ is the minimum required pore diameter and β is the angle between the pore surface and the centerline of the pore. Figure D.11 represents the front and side views of this pore which contains about 150,000 atoms. The system along with the protein was solvated and ionized as shown in Figure D.12. For this hexagonal system, periodic boundary condition was applied in three directions with non-orthogonal basis vectors.

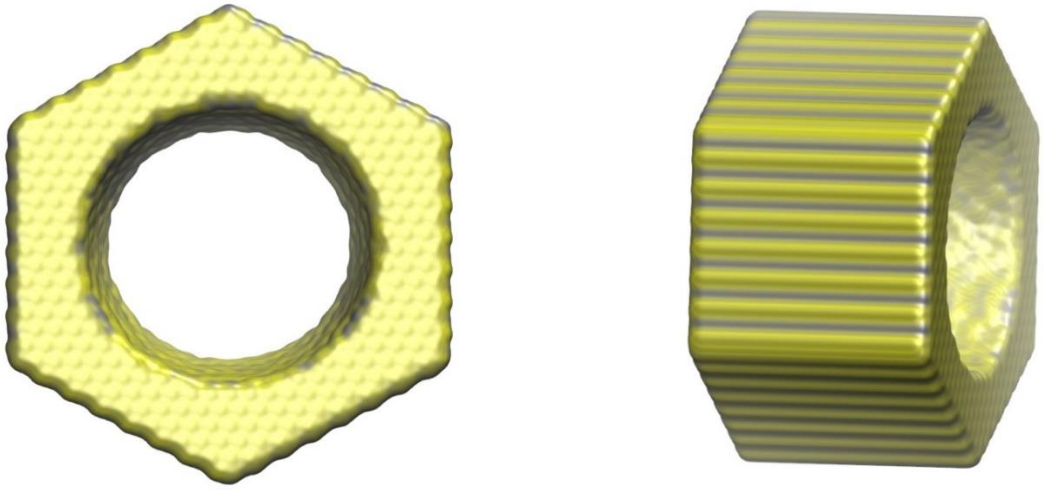

Figure D.11: Front and side views of hexagonal silicon nitride nanopore.

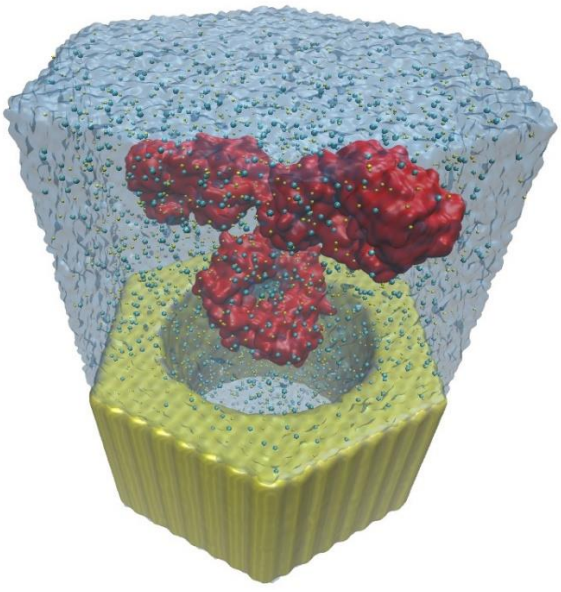

Figure D.12: Entire system including silicon nitride (yellow), protein (red), water (transparent blue) and ions (cyan and yellow spheres).

D.6 Diameter scans of proteins

It has been shown that the average diameter and charge of protein can be computed from the average ionic current associated with protein translocation.[8] Protein diameters can be estimated from the current blockage by the following equation:[9]

$$d_m \cong [(\Delta I / I_0)(h_{eff} + 0.8 d_p) d_p^2]^{1/3} \quad \text{(D.6.1)}$$

where d_m is the protein diameter, d_p is the pore diameter, and $\Delta I/I_0$ is the ratio of the mean blocked current for each computed point to the mean open-pore current level, respectively. It is notable that the term (h_{eff} + $0.8d_p$) is used as a correction factor. We used the approximation (d_p=h_{eff}) that is shown to be the best practice.[9]

Our ionic current calculations were substituted for $\Delta I/I_0$. As an example, we computed the scanned diameter of MTHK (see ionic current plot in D.1.8) ion channel (Figure D.13).

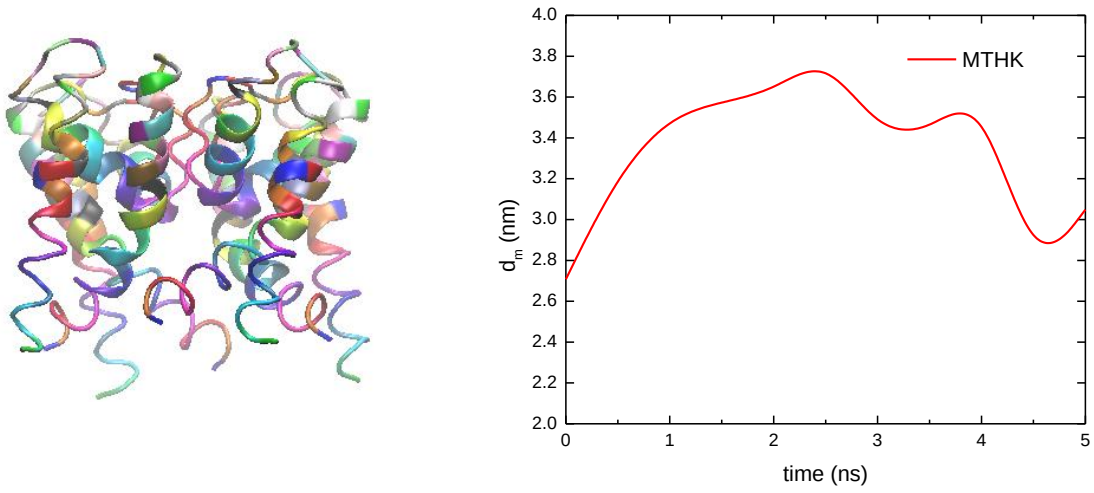

Figure D.13: A snapshot of MTHK (left). The scanned diameter (d_m) of MTHK ion channel (right).

D.7 References

1. Zou, P. J.; Pinotsis, N.; Lange, S.; Song, Y. H.; Popov, A.; Mavridis, I.; Mayans, O. M.; Gautel, M.; Wilmanns, M. Palindromic Assembly of the Giant Muscle Protein Titin in the Sarcomeric Z-Disk. *Nature* 2006, 439, 229-233.
2. Kuriyan, J.; Wilz, S.; Karplus, M.; Petsko, G. A. X-Ray Structure and Refinement of Carbon-Monoxy (Fe-Ii)-Myoglobin at 1.5-a Resolution. *J. Mol. Biol.* 1986, 192, 133-154.
3. Vijaykumar, S.; Bugg, C. E.; Cook, W. J. Structure of Ubiquitin Refined at 1.8 a Resolution. *J. Mol. Biol.* 1987, 194, 531-544.
4. Jiang, Y. X.; Lee, A.; Chen, J. Y.; Cadene, M.; Chait, B. T.; MacKinnon, R. The Open Pore Conformation of Potassium Channels. *Nature* 2002, 417, 523-526.
5. Dekker, C. Solid-State Nanopores. *Nat. Nanotechnol.* 2007, 2, 209-215.
6. Humphrey, W.; Dalke, A.; Schulten, K. Vmd: Visual Molecular Dynamics. *J. Mol. Graph.* 1996, 14, 33-38.
7. Comer, J.; Ho, A.; Aksimentiev, A. Toward Detection of DNA-Bound Proteins Using Solid-State Nanopores: Insights from Computer Simulations. *Electrophoresis* 2012, 33, 3466-3479.
8. Larkin, J.; Henley, R. Y.; Muthukumar, M.; Rosenstein, J. K.; Wanunu, M. High-Bandwidth Protein Analysis Using Solid-State Nanopores. *Biophys. J.* 2014, 106, 696-704.
9. Deblois, R. W.; Bean, C. P. Counting and Sizing of Submicron Particles by Resistive Pulse Technique. *Rev. Sci. Instrum.* 1970, 41, 909-&.